学　位　論　文

Observational study on the slip behavior of deep tremor in western Japan

（西日本における深部微動のすべり過程について）

平成 25 年 12 月　博士(理学)申請

東京大学大学院 理学系研究科

地球惑星科学専攻

太　田　和　晃

Abstract

We study the detailed spatio-temporal behavior of deep tremor in western Japan, by developing and applying a new slip inversion method. On the basis of resultant slip process, we discuss the relationship between slip evolution of tremor and the heterogeneities on the plate interface. We further make a comparison between tremor with very low frequency earthquakes (VLFs) and tremor with no visible VLFs to discuss the source area and occurrence conditions of VLFs.

Although many studies now recognize tremor as shear slips on the plate interface and swarm activities of low frequency earthquakes (LFEs), an ordinary slip inversion analysis is not available for tremor due to inadequate knowledge of source locations and Green's functions. Therefore, we construct a new method by combining precise locations of plate interface, synthetic template waveforms as substitutes of Green's functions and iterative deconvolution method.

We relocate a large number of LFEs beneath the Shikoku region by using the network cross-correlation (NCC) method. Relocated hypocenters are very concentrated in depth and show clear inclinations in every part of the region. The distributions of LFEs are well fitted by a single plane and we estimate the plate interface on the basis of the distribution.

Next we introduce the synthetic template waveforms as typical waveforms of tremor sources on the plate interface by stacking the seismograms of the LFEs at arranged points on the interface. We prepare the synthetic template waveforms in two regions in the western and central Shikoku. The usability of synthetic template waveforms is checked by moment tensor inversion and matched filter analysis. From moment tensor inversion, we obtain the focal mechanism of low-angle thrust faults and moment magnitude of 0.84, which are consistent with typical mechanisms of LFEs. We conduct a matched filter analysis using synthetic template waveforms to examine tremor activity in the western Shikoku. The synthetic template waveforms work well for detection and the detectability is over 100 times larger than that of the ordinary method adopted by Japan Meteorological Agency.

Using the synthetic template waveforms as substitutes of Green's functions,

we finally invert continuous tremor waveforms by iterative deconvolution method with a Bayesian constraint. The method is applied to a tremor burst episode for 12 days in the western Shikoku and for 1 day in the central Shikoku region which contains known VLF events. The resultant slip distribution shows a patchy structure and relatively rapid moment releases with durations less than 100 s occur on some patchy regions on the fault. These spatially and temporally heterogeneous slip patterns may be associated with the heterogeneities of material properties on the plate interface. The slip distribution of tremor and the centroid of coincidental VLFs are consistent with each other. This suggests tremor associated with VLF is triggered within the source area of VLF. The source size of VLFs in the central Shikoku approximated by slip distribution of tremor, ~5 km in radius, is much larger than the size of patchy slip region of tremor in the western Shikoku. Such difference in source size might possibly control the occurrence of VLFs.

Contents

Chapter 1　General Introduction

Deep nonvolcanic tremor is a newly discovered phenomenon in the 2000s which was first observed in the Nankai subduction zone of Japan by Obara [2002]. Tremor is observed as weak intermittent noise-like signals with long durations coherent among many stations. Individual train of tremor waves lasts typically tens of minutes and active periods of tremor with duration of days to weeks emerge repeatedly every several months [Obara, 2002]. Unlike volcanic tremor beneath active volcanos [Aki and Koyanagi, 1981], nonvolocanic tremor is located in a belt-like zone along the near 30 km depth contours of the subducting Philippine Sea plate which is a downdip extension of frictionally locked fault zone. Since the discovery of tremor, many studies have focused on the deep portion of subduction zone. This led to further discovery of related slow phenomena, such as low frequency earthquakes (LFE) [Katsumata and Kamaya, 2003], very low frequency earthquakes (VLF) [Ito et al., 2007], and slow slip events (SSE) [e.g., Obara et al., 2004; Hirose and Obara, 2005]. Outside Japan, similar phenomena are observed in many subduction zones worldwide, such as Cascadian subduction zone in the west coast of Canada and Washington state, USA [Rogers and Dragert, 2003], Cocos subduction zone in southern Mexico [Lowry et al., 2005], Hikurangi Trough off the east coast of the North Island of New Zealand [Douglas et al., 2005], Costa Rica subduction zone [Payero et al., 2004], and Alaska-Aleutian subduction zone [Ohta et al., 2006].

These phenomena are thought to be caused by “slow” physical process rather than ordinary earthquakes generated by instant fractures on a frictional fault, hence called as slow earthquakes. Slow earthquakes and megathrust earthquakes share the stress accumulation driven by tectonic loading and should be relevant to each other. The discovery of slow earthquakes requires us to reevaluate subduction zone and earthquake process.

Among the recently discovered slow earthquakes, deep tremor has been very much studied due to their frequent occurrences. Many studies now recognize tremor as shear slips on the plate interface and swarm activities of LFEs which are appearances in the smallest scale of slow earthquake family. Many

distinctive features of tremor including scale variant migration and t-linear scaling among slow earthquakes have been investigated. We can afford to say these features as macroscopic views because these analyses utilize only a part of tremor waveforms or see tremor waveforms as a whole entity.
We expect further progress by investigating the evolution of tremor slips, the relationship between tremor and other slow earthquakes, and heterogeneities on the plate boundary by analyzing the entire waveform of tremor in detail. This thesis is the first attempt to investigate a detailed spatio-temporal evolution of deep tremor by utilizing the slip inversion method. We will engage in a further discussion on the spatial relationship between tremor and VLFs.
In this chapter, we review the issues and previous studies about tremor location, relationship between tremor and slow earthquakes, and characteristic tremor behavior on heterogeneous plate interface.

1.1 Tremor location

Accurate locating of tremor has been an important issue because the knowledge of true source locations is essential to understand the generation mechanism of tremor. Since the initiation of tremor is very hard to constrain due to lack of distinct body wave arrival, it is difficult to determine their source locations. Many approaches have been tried to locate tremor sources and various, sometimes controversial, discussion have been made about the generation of tremor associated with source locations [Rubinstein et al., 2010].
The location methods are roughly classified into two groups, envelope-based method and phase-based method. One of the most famous location and detection method based on the envelope is the envelope correlation method [Obara, 2002]. The envelope correlation method uses cross-correlation of tremor waveforms between neighbor stations to estimate the differential arrival times across the network. Then these differential times are used to locate the tremor sources by assuming the propagating velocity as S-wave velocity. Another approach is a source scanning algorithm developed by Kao and Shan [2004]. A source scanning algorithm (SSA) uses the maximum amplitude of tremor waveforms across the network to determine the source

locations of tremor by back projection. These methods are very useful to get a whole picture of tremor activity and now employed for automated detection and location methods [Kao et al., 2007a; Wech and Creager, 2008; Suda et al., 2009]. Epicentral tremor locations computed using these methods show similar distributions along subducting plates in each subduction zone [Obara, 2002; Kao et al., 2005]. The distributions in depth tend to be estimated over a wide range. In Cascadia, tremor located by SSA show the wide depth distribution within a volume of more than 40 km [Kao et al., 2005]. However, the location uncertainty is fairly larger in depth than horizontal due to unavailability of P-waves. Thus, we should take caution in discussing whether apparent wide distribution is real.

On the other hand, the phase-based methods as typified by Shelly et al. [2006] utilize the cross correlation coefficients between events to improve the relative locations. Instead of tremor sources, Shelly et al. [2006] determines the locations of LFEs in the western Shikoku by double difference techniques [Zhang and Thurber, 2003] with differential arrival times corrected using cross-correlations for each station. The majorities of LFEs estimated by them are well confined to the anticipated plate interface. These precisely relocated LFEs are used as template in a running cross-correlation search of tremor sources from continuous seismograms in the western Shikoku [Shelly et al., 2007a]. They demonstrated that a large portion of tremor seismograms could be explained by a swarm of LFEs. Brown et al. [2008] developed the method to detect LFEs from tremor without known templates using an autocorrelation technique. The studies based on the autocorrelation method reveal the tremor along three subduction zones including southwest Japan, Cascadia, and Costa Rica localized to the plate interface [Brown et al., 2009]. Another type of phase based method is based on S-P time. La Rocca et al. [2009] deduced S-P times by computing the cross correlations between vertical and horizontal components of tremor seismograms. The authors show the tremor in Cascadia locates near plate interface. Due to the heavy computational costs, these phase based methods are not good at grasping a whole picture of tremor activity, but suitable for estimating the tremor locations within limited regions or periods at a high resolution.

In the previous study, as an extension of the phase-based methods, we

developed an accurate hypocenter determination method using the summation of cross-correlation coefficients for network stations, termed network correlation coefficients (NCC) [Gibbons and Ringdal, 2006] and demonstrated that LFEs in western Japan are concentrated in a very narrow zone around the anticipated plate interface [Ohta and Ide, 2008; Ohta and Ide, 2011]. This suggests that the hypocenters of LFEs can be in turn distinctive indicators of the locations of the plate interface. In this thesis, we estimate the location of the plate interface by relocating a large number of LFEs in the Shikoku region using the network correlation method.

1.2 Tremor and various slow earthquakes

One of the striking features of tremor is scale variant migration. Obara [2002] reported that tremor in south west Japan migrates over 100 km at speed of 10 to 13 km/day along strike of subduction zone. Such tremor migration along strike is usually coincident with migration of SSE [Obara, 2010]. Similar long-term migration along strike has been also reported in Cascadia [Dragert et al., 2004; Kao et al., 2007b]. Shelly et al., [2007ab] found much faster migration of tremor sources at speed of 25 to 150 km/h primarily in the subduction dip direction in western Shikoku. This rapid short-term migration has been examined by systematic cross correlation search with template LFEs as described above, termed matched filter analysis. In Cascadia, similar short-term migration along dip has been found as tremor streaks [Ghosh et al., 2010]. More recently, Houston et al. [2011] found an intermediate-scale tremor migration at speed of 100 km/day, termed rapid tremor reversals. Although the underlying mechanisms of these types of migration are still under issues, the scale variant migration indicates close association between tremor and larger scale slip such as SSEs.

Ide et al. [2007] found the scaling relationship shared among slow earthquakes. While ordinary earthquakes grow in seismic moment with cube of their duration, slow earthquakes grow in seismic moment linearly with their duration. As described before, tremor is a swarm of LFEs which are the smallest member of slow earthquakes. Hence, tremor and other slow earthquakes are thought to be shear slips obeying a common physical

mechanism. This idea is also supported by similar observations such as the linear relationship between the moment of SSEs and their duration [Schwartz and Rokosky, 2007], the linear relationship between the moment of SSEs and the total duration of tremor during SSEs [Aguiar et al., 2009], and the close correspondence between moment rate of longer (up to 200 s) VLFs and tremor energy [Ide et al., 2008]. However, these relationships are based on moment and the spatial relationships among tremor and slow earthquakes are rather obscure. Basically tremor is observed at locations similar to SSEs [Rogers and Dragert, 2003; Obara et al.,2004]. Bartlow et al. [2011] reported the spatial correspondence between tremor and slow slip in 2009 Cascadia ETS event. On the other hand, the inconsistency between the slip distribution of SSEs and tremor in Cascadia is also pointed out [McCaffrey, 2009; Wech et al., 2009; Gomberg et al., 2010]. They argue that the peak of ETS slip is shallower than tremor distribution. Similarly, tremor and VLFs are visible in one seismic record and expected to occur at the same location [Ito et al., 2007]. But their spatial correspondence is still unclear. Even for tremor and LFEs, it is yet unclear whether tremor occurs at exactly the same location as LFEs. Guilhem and Nadeau [2012] pointed out the presence of non-LFE tremor activity which is undetectable using known template LFEs. To address these issues, it is necessary to investigate the detailed locations of tremor with no spatial limitations of known template LFEs. In this thesis, we introduce the synthetic template waveforms as typical waveforms of tremor to relieve these spatial limitations.

1.3 Tremor and the heterogeneities on the plate interface

Tremor behavior on the plate interface are various and spatially characteristic [Ide, 2010; Obara, 2011]. Obara [2010] reported that tremor source regions in south west Japan are segmented along strike and tremor in each segment has specific recurrence intervals. Tremor activities are also depth dependent. Obara et al. [2010] found that each duration of tremor episodes changes inversely with depth. Ide [2010] also pointed out the depth dependency in the duration and the tidal sensitivity of tremor. These characteristics should reflect the heterogeneities of frictional properties on the plate interface. Ando et al. [2010] expressed the heterogeneous plate

interface as the mixtures of brittle patchy region and back ground ductile region. In this model, tremor and LFEs are triggered on the brittle patches by back ground slow slip. Nakata et al. [2011] examine the effects of patch density and viscosity on the slip evolution of tremor, such as shape of moment rate function and propagation velocity. If we can compare these simulation predictions with slip evolution of tremor in real, it would greatly help to evaluate the heterogeneities on the plate interface, which would in turn enable more realistic modeling of the generation of tremor and other slow earthquakes. However, our current image of tremor evolution is spatially and temporally limited. An ordinary slip inversion now commonly done for earthquakes [Hartzell and Heaton, 1983] is not applicable due to inadequate knowledge of Green's function of tremor. We approach the problem by developing and applying a new slip inversion method using the synthetic template waveforms described before as empirical Green's functions.

1.4 Construction of the slip inversion method for tremor

In this thesis, we construct a new slip inversion method to investigate the detailed slip evolution of tremor in western Japan. There are three keys necessary for slip inversion of tremor, which are the precise fault model, Green's functions, and the slip inversion method. In Chapter 2, we estimate accurate locations of the plate interface by relocating a large number of LFEs, which are in turn used as the fault model for tremor. In Chapter 3, we further introduce the synthetic template waveforms as substitutes of green's functions for tremor and check the usability of them by moment tensor inversion and matched filter analysis. In Chapter 4, we finally invert continuous tremor waveforms by iterative deconvolution method using synthetic template waveforms as empirical green's functions. Based on the results we discuss the relationship between slip evolution of tremor and the heterogeneities on the plate interface, and the relationship between tremor and VLFs.

Chapter 2 Estimation of the plate interface of the subducting Philippine Sea plate

2.1 Introduction

Recent progress in the analysis of seismic waves and hypocenter determination methods has revealed that most of tremors and LFEs along subduction zones worldwide occur on the plate interface of subducting oceanic slab [e.g., Rubinstein et al., 2010]. This fact also suggests that the accurate locations of the hypocenters of LFEs can be in turn used as an indicator of the location of the plate interface which is difficult to constrain by means other than seismic reflection surveys or receiver function analysis [Ammon et al, 1990].

We developed an accurate hypocenter determination method which can relocate a cluster of seismic events by utilizing the summed cross correlation coefficient across the network, which is referred to as a network correlation coefficient (NCC) and demonstrated that hypocenters of LFEs in Nankai subduction zone construct a thin planar structure which indicates the boundary between the subducting Philippine Sea plate and the overriding plate [Ohta and Ide, 2008, 2011].

In this chapter, we estimate the location of the plate interface by precise hypocenter distribution of LFEs which occurred from 2004 to 2011 in the Shikoku region. This is the preparation of the first key for slip inversion of tremor.

2.2 NCC Method

We briefly review the NCC method developed by Ohta and Ide [2008, 2011], which enables accurate hypocenter estimation for an event cluster. This method estimates the relative hypocenter location for each pair of events in the cluster by maximizing the summation of waveform cross-correlation for all available stations. Then, these relative locations are used to determine a set of hypocenter locations.

The relative hypocenter location $\Delta\mathbf{x}_{ij}$ and the origin time difference Δt_{ij} between a pair of earthquakes, a reference event i and a target event j, are determined by maximizing NCC,

$$\mathrm{NCC}(\Delta\mathbf{x}_{ij}, \Delta t_{ij}) = \sum_{ln} \frac{\sum_m u_m^{iln} u_m^{jln}}{\sqrt{\sum_m \left(u_m^{iln}\right)^2 \sum_m \left(u_m^{jln}\right)^2}}, \tag{2.1}$$

where u_m^{iln} is digitized ground velocity at m-th time step in l-th direction at n-th station for i-th event. The seismogram of the target event j is time shifted using $\Delta\mathbf{x}_{ij}$ and Δt_{ij} as

$$\hat{t}(\mathbf{x}_i^0 + \Delta\mathbf{x}_{ij}, \mathbf{x}_n) - \hat{t}(\mathbf{x}_i^0, \mathbf{x}_n) + \Delta t_{ij}, \tag{2.2}$$

where $\hat{t}(\mathbf{x}_1, \mathbf{x}_2)$ is the theoretical travel time between two points $\mathbf{x}_1$ and $\mathbf{x}_2$, and $\mathbf{x}_i^0$ is the hypothetical location for the reference event, which we assumed as the JMA catalog value. We find the global maximum of NCC using a grid search.

Applying this procedure to every pair of N events yields $N \times (N-1)$ relative locations, $\Delta\mathbf{x}_{12}^{NCC}, \ldots, \Delta\mathbf{x}_{ij}^{NCC}, \ldots, \Delta\mathbf{x}_{NN-1}^{NCC}$. Assuming that these values have Gaussian errors, we determine the hypocenter locations of N events $\mathbf{x}_m (m = 1, \ldots, N)$, minimizing,

$$E = \sum_{i,j,i\neq j} w_{ij} \left(\mathbf{x}_j - \mathbf{x}_i - \Delta\mathbf{x}_{ij}^{NCC}\right)^2 + \sum_i \alpha^2 (\mathbf{x}_i - \mathbf{x}_i^0)^2, \tag{2.3}$$

where w_{ij} is a weighting factor associated with the maximum NCC [Ohta and Ide, 2008], and α is a hyperparameter, controlling the weight of prior information of the initial absolute location $\mathbf{x}_i^0$ given by the JMA catalog. We select the optimum value of α by minimizing Akaike's Bayesian information criterion (ABIC) [Akaike, 1980; Yabuki and Matsu'ura, 1992].

The maximum of NCC calculated for real events are often small. Such insignificant maximum could lead to completely wrong estimation of $\Delta\mathbf{x}_{ij}^{NCC}$ and violate the assumption of Gaussian errors. In this study, we add two

outlier control criteria adopted in Ohta and Ide [2008]. Before the linear inversion using (2.3), we eliminate the data $\Delta\mathbf{x}_{ij}^{NCC}$, (C1) if the maximum NCC is smaller than 6 times of its standard deviation σ_{NCC}, or (C2) if the difference between two opposite relative locations, $\Delta\mathbf{x}_{ij}^{NCC}$ and $-\Delta\mathbf{x}_{ji}^{NCC}$, is larger than 1 km. As an exception for (C2), we keep $\Delta\mathbf{x}_{ij}^{NCC}$ if the maximum NCC is larger than $7\sigma_{NCC}$ and the maximum of the opposite is smaller than $5\sigma_{NCC}$.

2.3 Data and study area

In the western Shikoku region, Shelly et al. [2006] determined the hypocenters of LFEs using the double-difference tomography method. Tremor in this region is very active and often correlates with slow slip events. Most seismic stations have been installed in quiet areas and signal to noise ratio is high. More than 4,000 LFEs have been detected and located by JMA from 2004 to 2011.

The data are 3-component velocity seismograms observed at all available Hi-net stations maintained by the National Research Institute for Earth Science and Disaster Prevention (NIED) and seismic stations maintained by Earthquake Research Institute, University of Tokyo, JMA, and Kochi University. Each seismogram is band-pass filtered between 2-8 Hz. We calculate waveform cross correlation for every pair, using the vertical component of P-wave and two horizontal components of S-wave. The number of stations available for each pair varies but is about 10 on average. The time window used for calculating a cross-correlation is from 1.5 s before to 2.5 s after the theoretical P- or S-wave arrival times. Travel times are calculated based on the 1-D velocity structure model of JMA 2001 [Ueno et al., 2002].

2.4 Relocation of LFEs in Shikoku

We relocate all LFEs in the JMA catalog from April 2004 to March 2011 in the Shikoku region (Figure 2.1). We divide the whole area to 11 subareas (A-K) and apply the NCC method to events in each subarea. Because NCC between a pair of events decreases with distance even if the mechanisms are identical, it does not have much meaning to apply the method to events far from each other. Therefore, the relative location search between a pair of events using NCC is omitted if their epicentral distance in the catalog is larger than 20 km. Figure 2.2 shows all the relocated events (red dots). Not all events are relocated by the NCC method for the reason that some events have no significant correlation with any other events in the subarea. The numbers of events applied and relocated in each subarea are shown in Table 2.1. Total number of the relocated event is about 60 % of applied events, but the ratio between them is very different for each subarea.

Figure 2.3 shows the comparison between the hypocenter distributions of the LFEs in JMA catalog and that relocated by the NCC method in the cross sectional views along 11 profiles (A-K). The relocated hypocenters are more concentrated in the depth direction and inclined landward, which is consistent with the assumption that these events occurred on the plate interface.

We divide LFEs into groups for each subarea on the basis of relative location information constrained by the NCC method. LFEs in one group have at least one relative location information with a significant NCC to others in the same group. Figure 2.4 shows the epicenters of LFEs which are the same as red dots shown in Figure 2.2 but with colors coded according to the groups. Group ID is attached for each subarea in order of the number of events within the group. Figure 2.5 shows the cross-sectional views of Figure 2.4 along each profile. The numbers of events in each group are shown in Table 2.2. The numbers of groups in each subarea are different among subareas. In the western and central Shikoku (E-H), there are small numbers of groups and most events belong to one group. Especially for subarea F and H, all LFEs are in one group even though there are many events. On the other hand, LFEs in other subareas are into various groups.

2.5 Estimation of the plate interface

We next estimate the location of the plate interface. Assuming the LFEs relocated by the NCC method occur on the plate interface, we fit a plane to the 3D distribution of hypocenters for each subarea. We minimize the vertical distance between each hypocenter and the plane by least squares. Figure 2.6 shows the map view of the geometries of the estimated planes. Each plane is shown as a $10\,\mathrm{km} \times 10\,\mathrm{km}$ square with the center at the centroid of the distribution of LFEs for demonstration purpose. Figure 2.7 shows the cross sectional views of the relocated LFEs and the estimated plane along profiles perpendicular to the strike in each subarea. The information of each plane is summarized in Table 2.3 (A-K). In most subareas, the hypocenters of LFEs are well fitted, with the standard deviation less than 1.5 km. Estimated planes are located at around 30 km depth and dip to the northwest in all the subareas except G, I, and K. In the subareas G and I, planes dip seaward in contradiction to other subareas. In the subarea K, the plane dips to the northeast. Dip angles are steeper beneath the Bungo channel (A-B) and modest in the central Shikoku region (G-J).

2.6 Discussion

Ohta and Ide [2011] suggested that apparent wide depth distribution of LFEs along Nankai trough in JMA catalog is caused by estimation errors. Relocated LFEs are more concentrated in the depth and the distribution is consistent with the geometry of the oceanic Moho. Results in this study confirm this. While many events are relocated successfully, significant number of events cannot be relocated. The applicability of NCC method is very different among subareas as shown in Table 2.1. There are many reasons for the difference in the number of events relocated. One influential reason is the difference in the extent of temporal isolation of LFE events because the superposition of successive events tends to lower cross correlations, which may prevent relocation even though the NCC method is robust. In the western Shikoku (E,F) where the NCC method works pretty well, LFEs are more impulsive than those in other regions. This feature is

also shown in the difference in duration of tremor among the regions [Ide, 2010].

Since the cross correlation of a pair of events decays with the inter-event distance, the NCC method is applicable only for closely located events. Hence, sparse distribution of the events leads to isolated clusters and relative locations between the clusters cannot be constrained. In Chapter 2.4, these clusters are classified as groups in each subarea (Fig. 2.4, Fig. 2.5). Although the diversity of focal mechanisms is also a possible reason that separates clusters, the difference in the density of events is easy to explain the variation of groups among subareas.

The distributions of LFEs are well explained by a single plane. However, we should note that relative locations of the groups are not constrained at all in this study and the uncertainties in the original catalog remains. The apparent reverse dips in the subarea G and I might be produced by such uncertainties. The dip angles in those subareas are mainly controlled by relative locations between group 1 and group 2. For the same reason, the plane geometry estimated in the subarea K is not constrained in this study although it does not contradict to the geometry of the Philippine Sea plate.

We retry to estimate the fault plane by using only events within one group (Fig. 2.8, Fig. 2.9). In subarea G, we fit the plane to events within group 1. As shown in Table 2.3 (G-1), estimated strike and dip of the plane are more consistent with the subducting plate. In fact, most of events are in group 1, therefore it is reasonable to use only events within this group. By consrast, in subarea I, significant number of events belong to group 2 (Table 2.2) and the groups 1 and 2 are clearly apart from each other (Figure 2.5). We fit two planes based on the events in groups 1 and 2, respectively (Fig. 2.8, Fig. 2.9). Although the vertical locations are different, the strikes and dips are almost consistent with each other in Table 2.3 (I-1 and I-2). For discussing whether the difference in the depth is true or not, more improved techniques to constrain absolute locations are required.

2.7 Conclusion

In this chapter, we relocate a large number of LFEs beneath the Shikoku region by using the NCC method. Relocated hypocenters of LFEs are more concentrated in the depth than in the original catalog and show clear inclinations in every part of the region. We estimate the plate interface on the basis of the distribution of LFEs. The distributions of LFEs are well fitted by a plane in each subarea. The estimated locations of LFEs and the fault models can be used for further studies to catch up the detailed space time evolution of tremor sources in the following chapters.

Figures

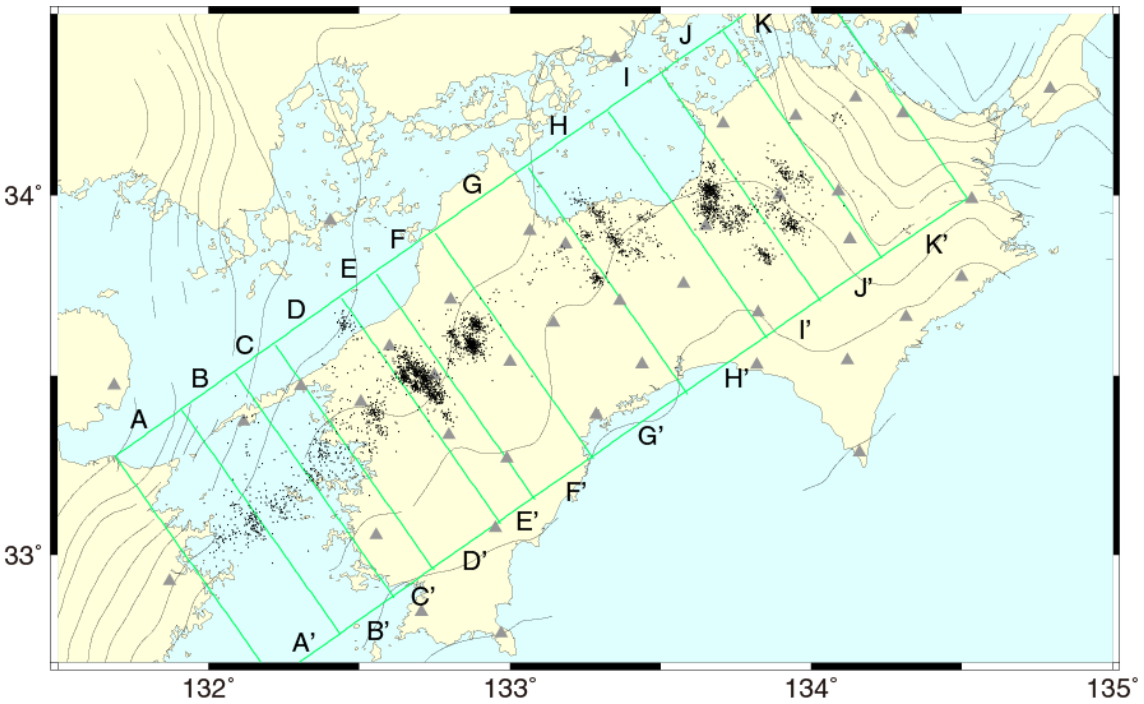

Figure 2.1: Map showing the epicenters of LFEs in JMA catalog from 2004 to 2011 (black dots). Green rectangles (A to K) indicate subareas analyzed in this study. The depth contour lines indicate the depth of the oceanic Moho estimated by receiver function analysis [Shiomi et al., 2008].

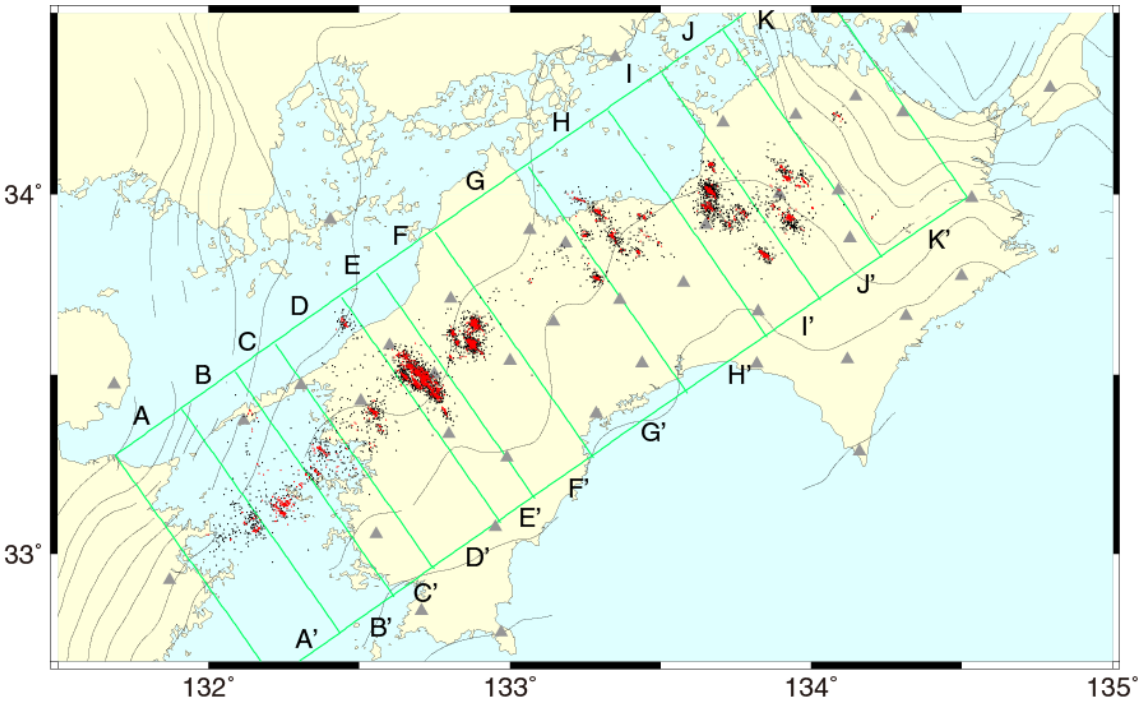

Figure 2.2: Map showing the epicenters of LFEs in JMA catalog (black dots) and relocated in this study (red dots). Others are the same as Figure 2.1.

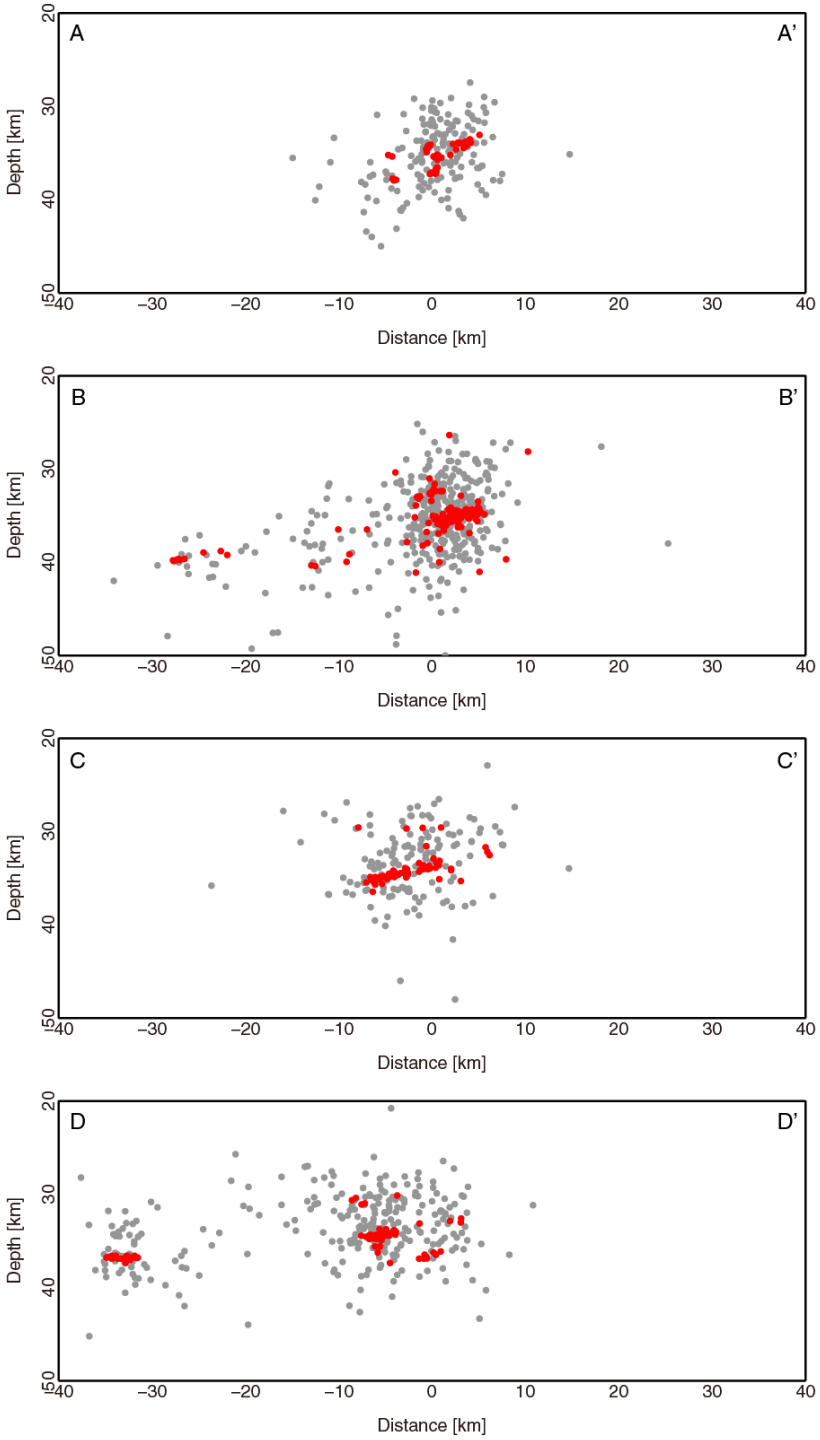

Figure 2.3: Cross-sectional views of the hypocenters of LFEs in JMA catalog (gray circles) and relocated by NCC method (red circles) along 11 profiles in each subarea (A-K) shown in Figure 2.2.

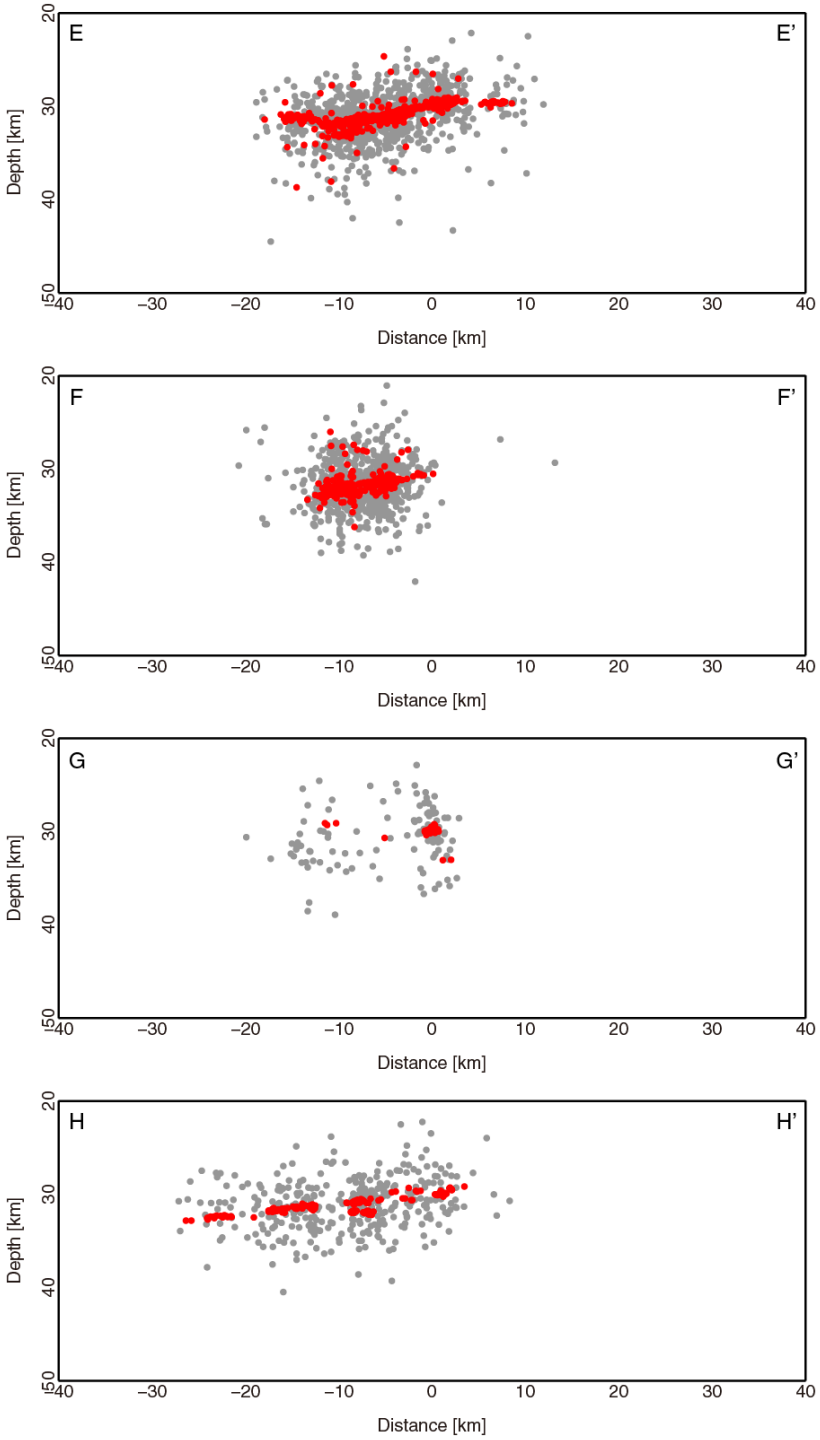

Figure 2.3: (Continue)

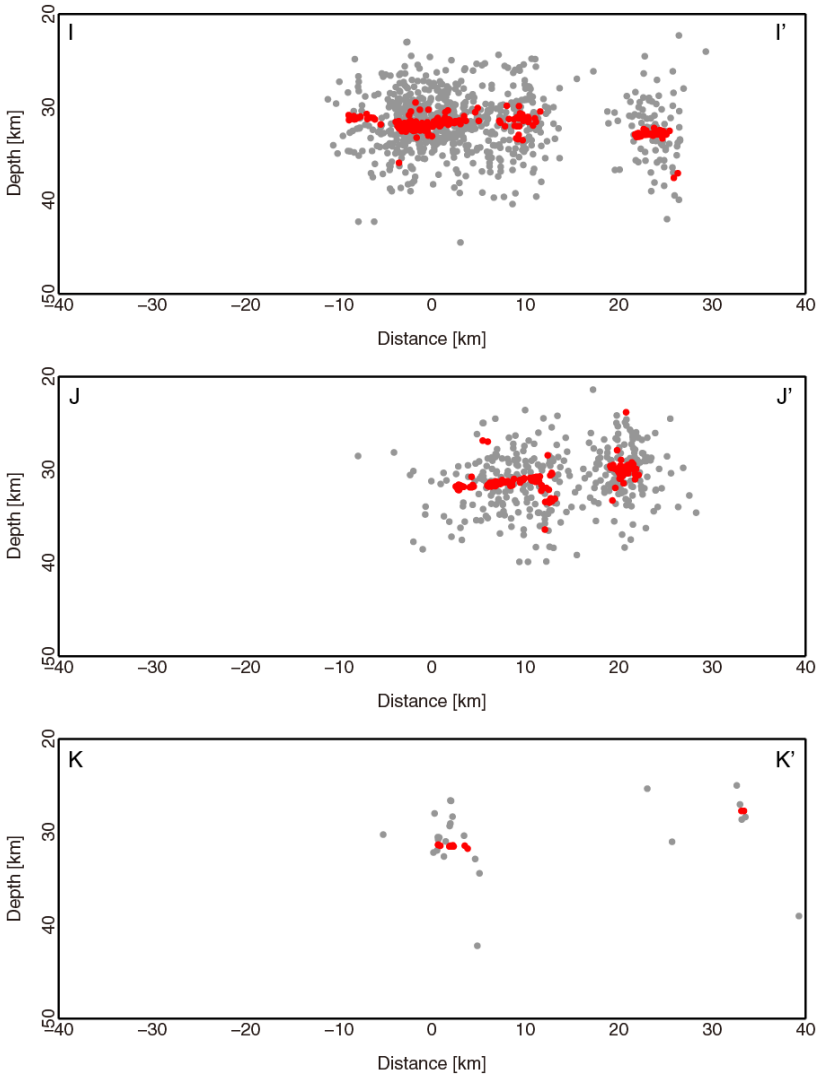

Figure 2.3: (Continue)

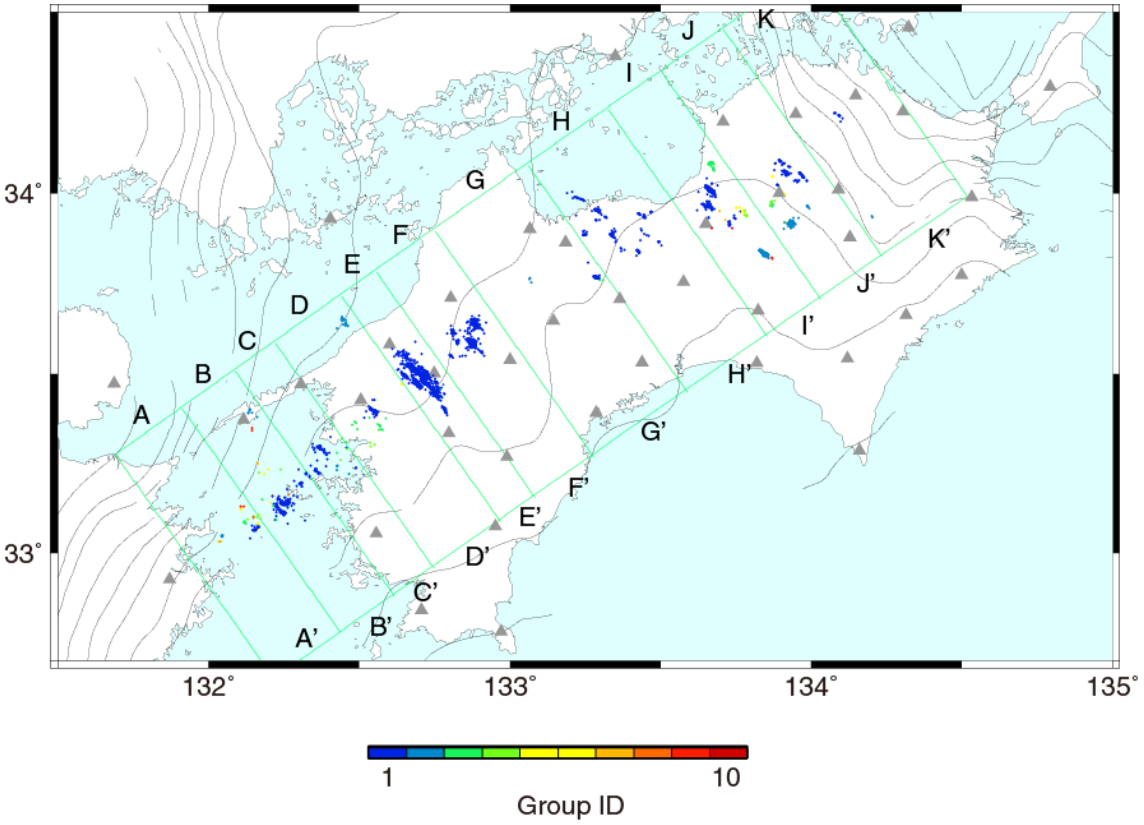

Figure 2.4: Epicenters relocated by NCC method colored based on the groups in which all LFEs are successfully connected by significant NCC. Group ID is attached for each subarea in order of the number of events included.

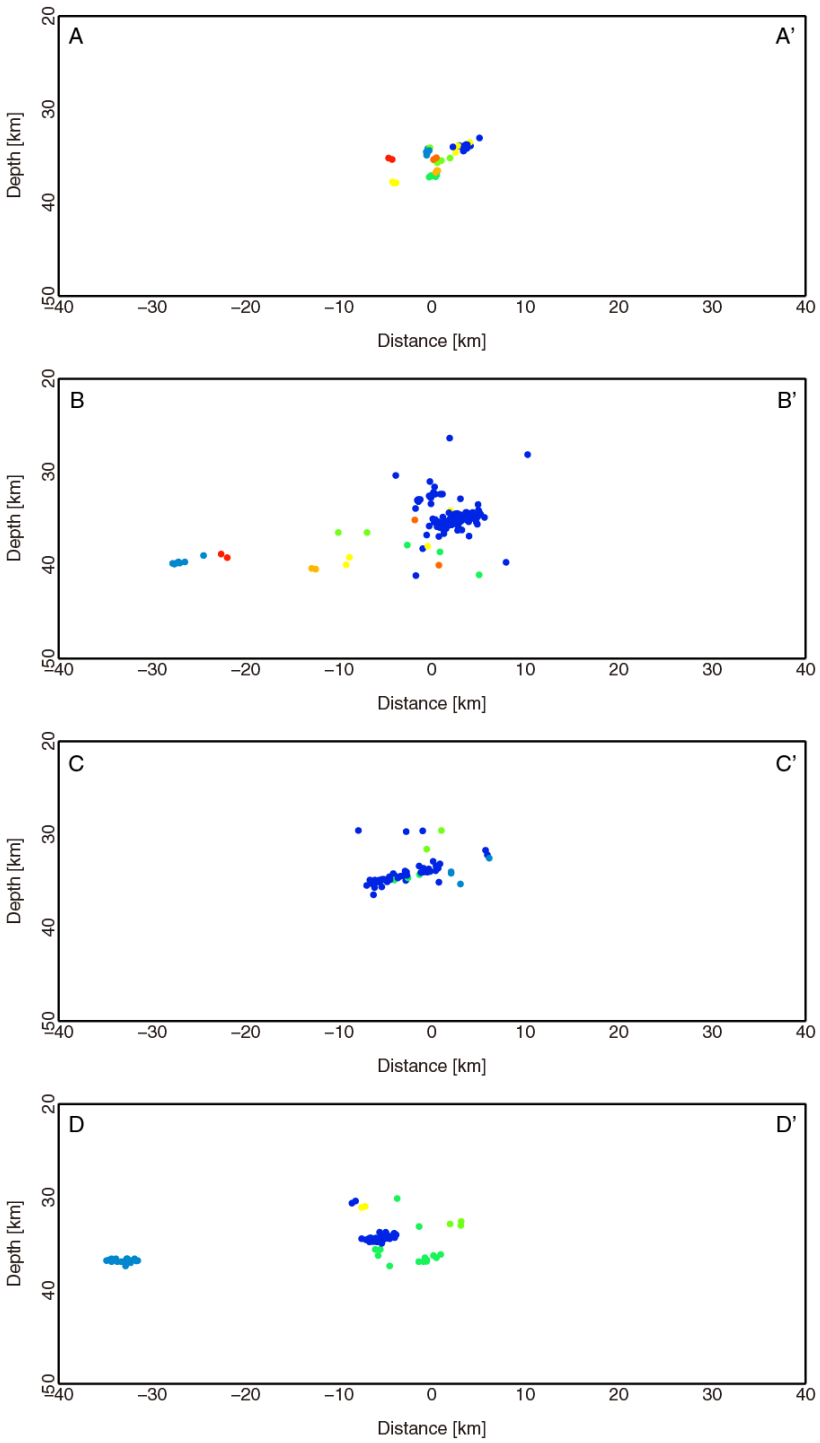

Figure 2.5: Cross-sectional views of the hypocenters of LFEs relocated by NCC method (color circles) along 11 profiles in each subarea (A-K). Color is coded with the same rule as Figure 2.4.

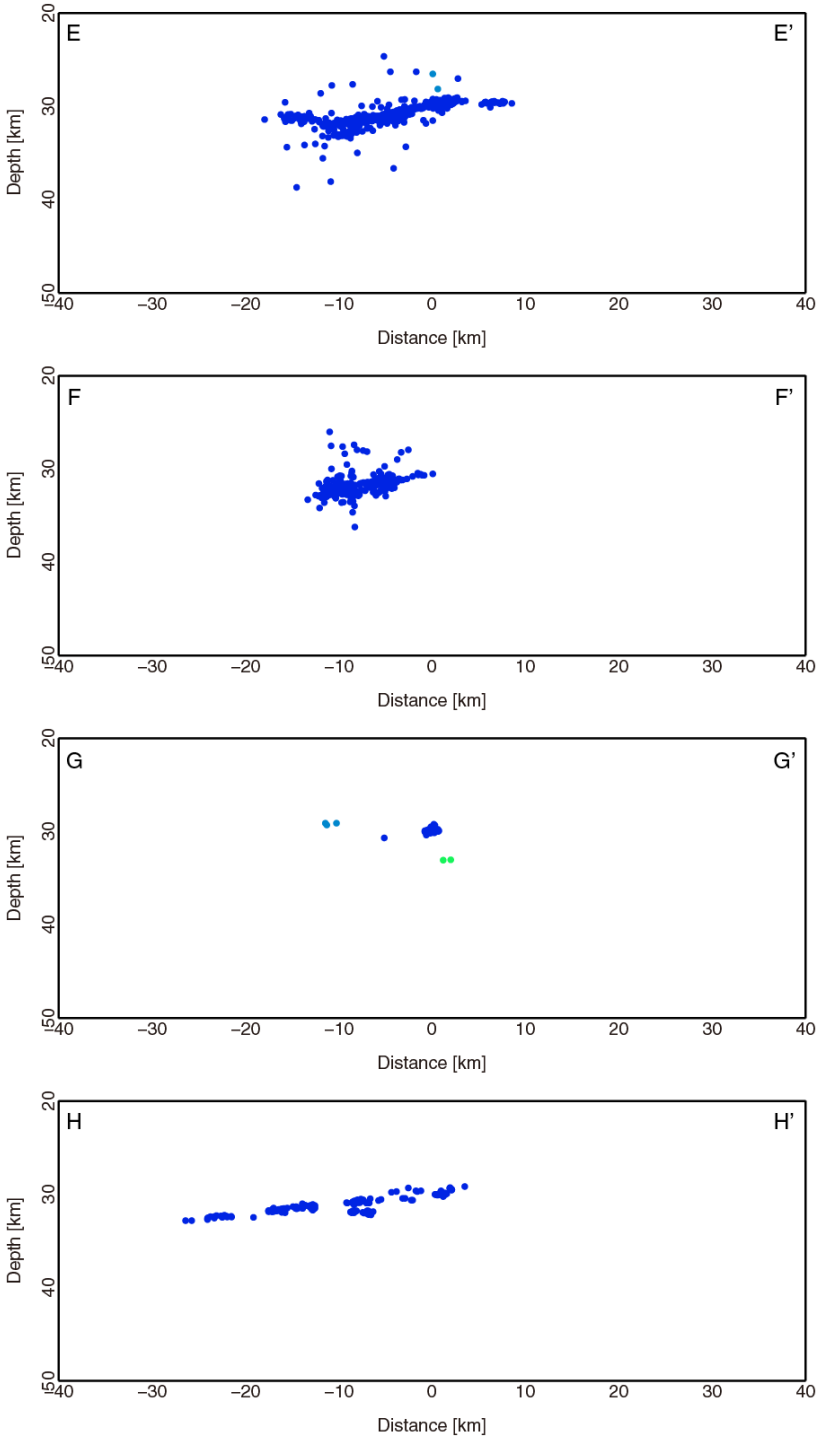

Figure 2.5: (Continue)

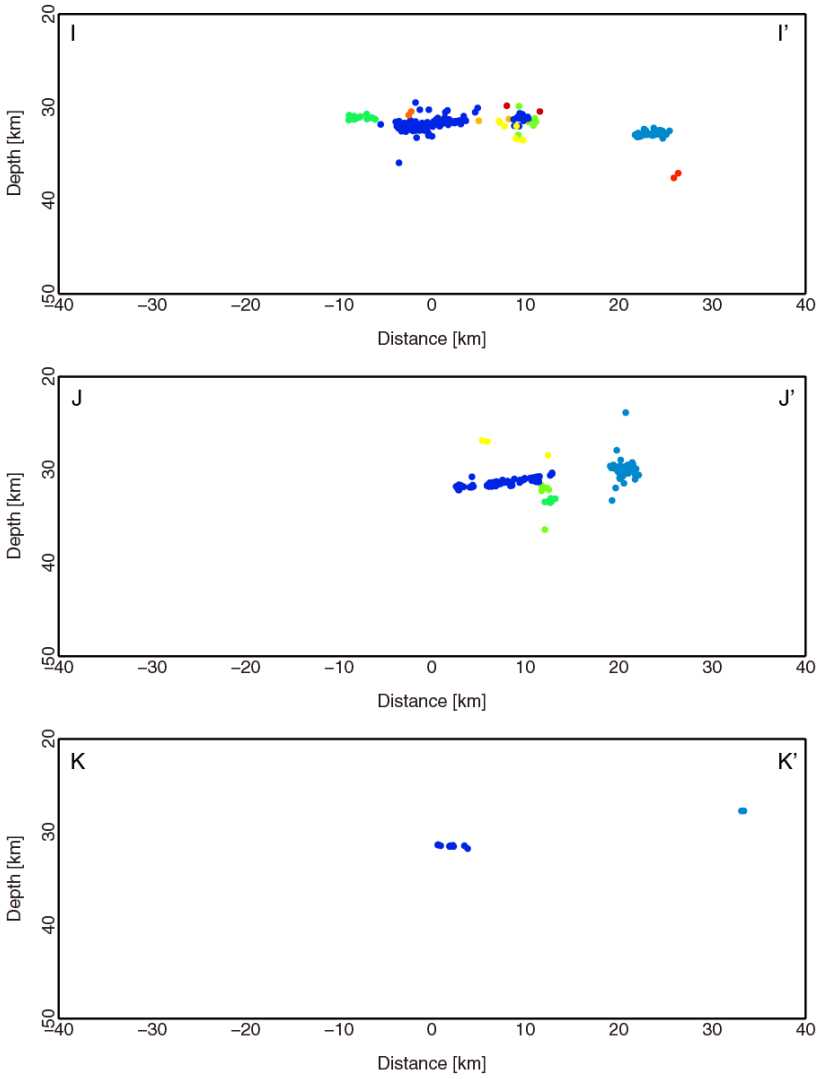

Figure 2.5: (Continue)

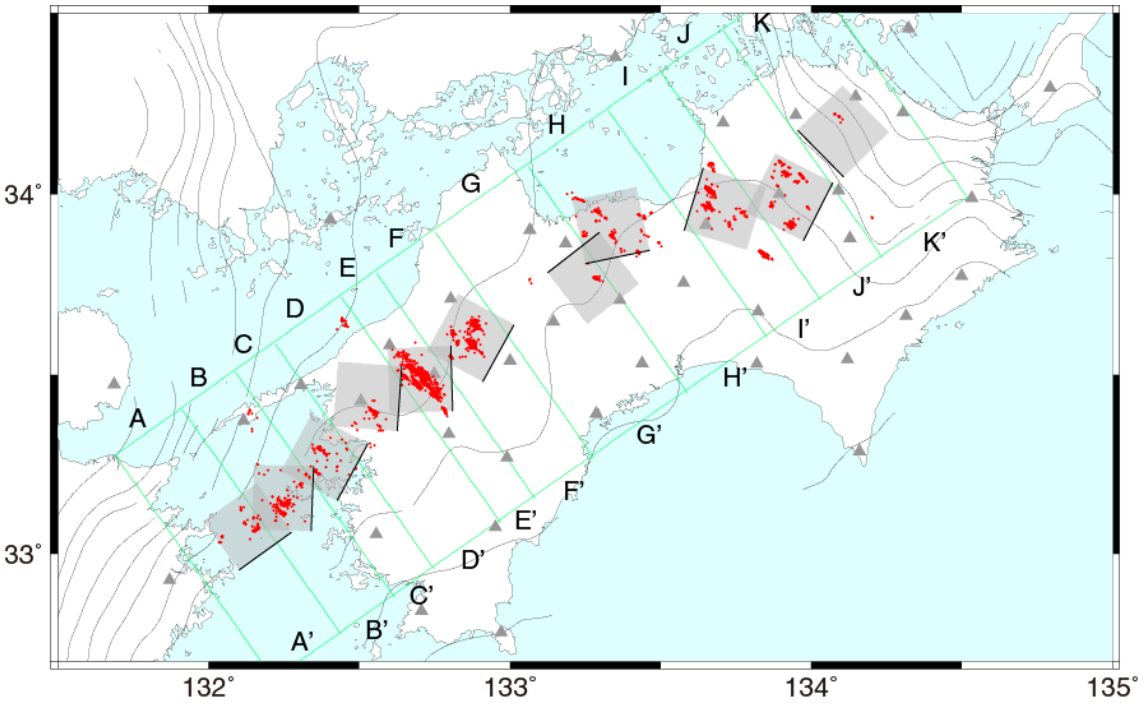

Figure 2.6: Map showing the geometries of estimated plate interface for each subarea (gray squares). The up-dip sides are indicated by solid black lines. Red dots show the relocated epicenters of LFEs. Others are the same as Figure 2.1.

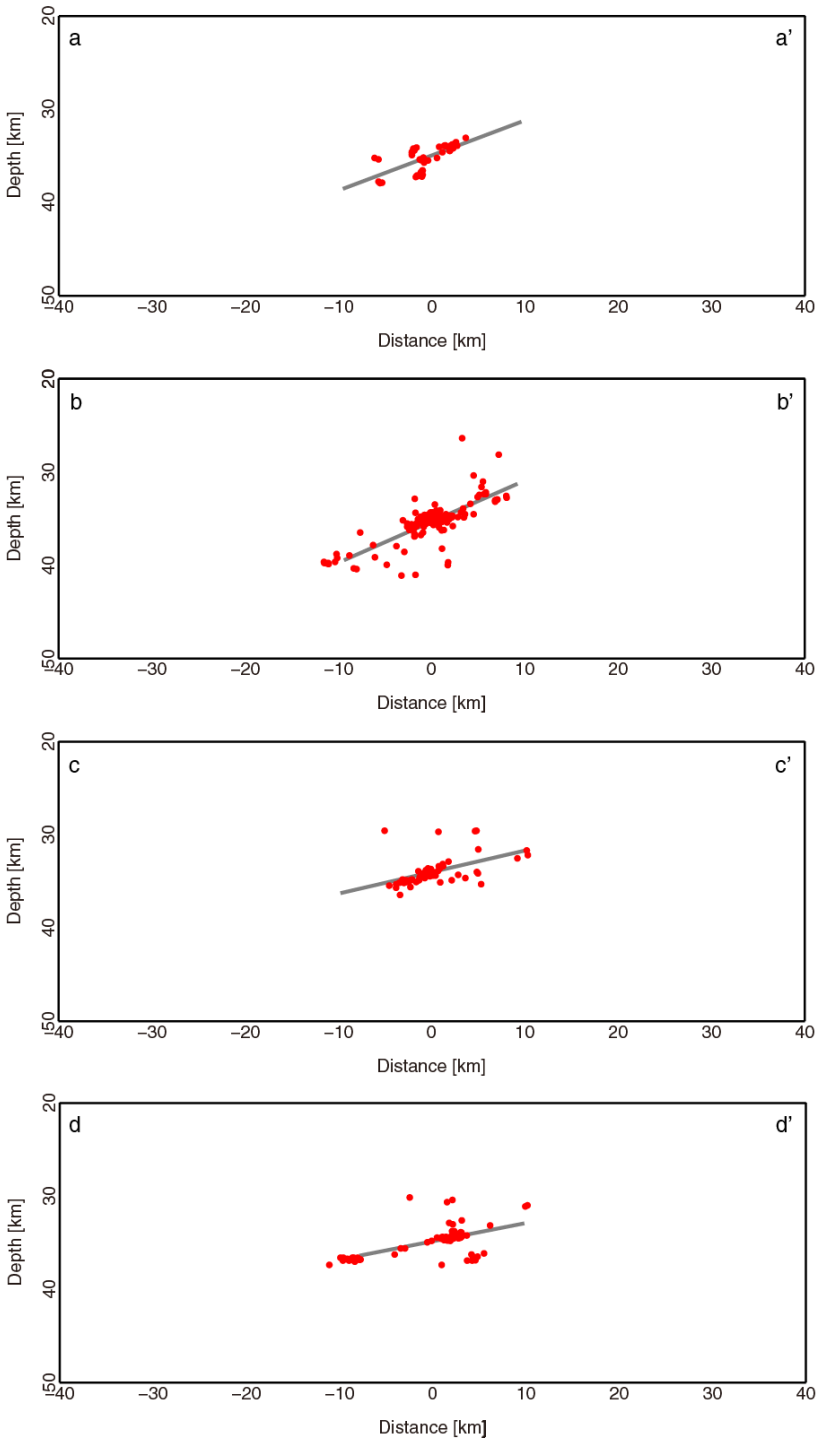

Figure 2.7: Cross-sectional views of the relocated LFEs (red circles) and estimated plate interface (gray lines) along profiles perpendicular to the strike in each subarea (A-K).

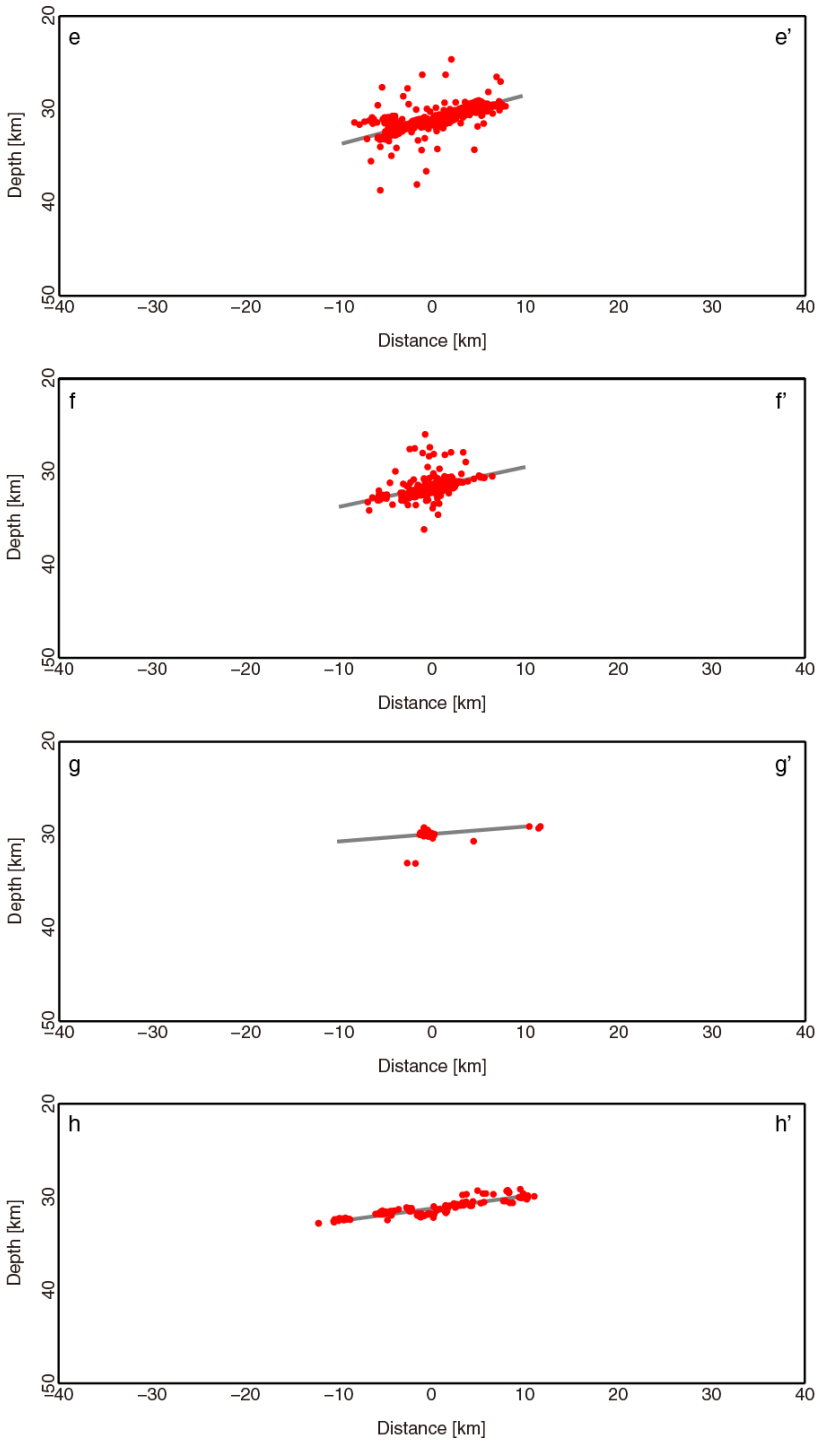

Figure 2.7: (Continue)

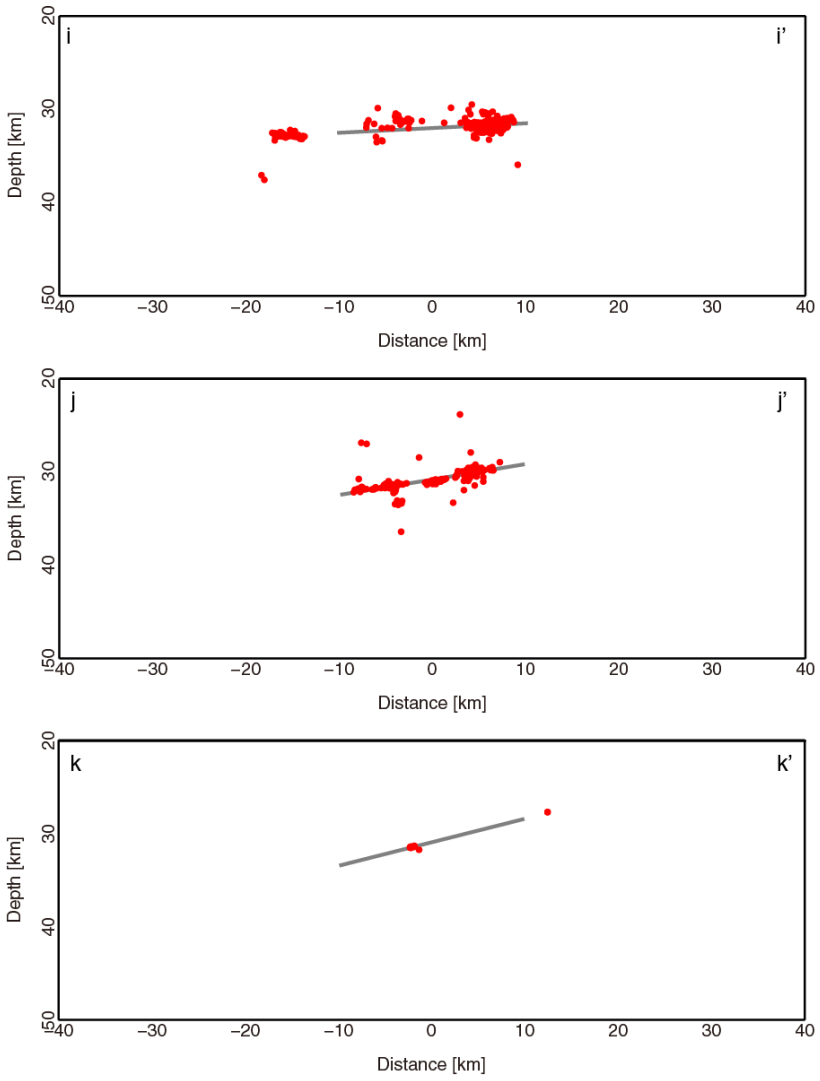

Figure 2.7: (Continue)

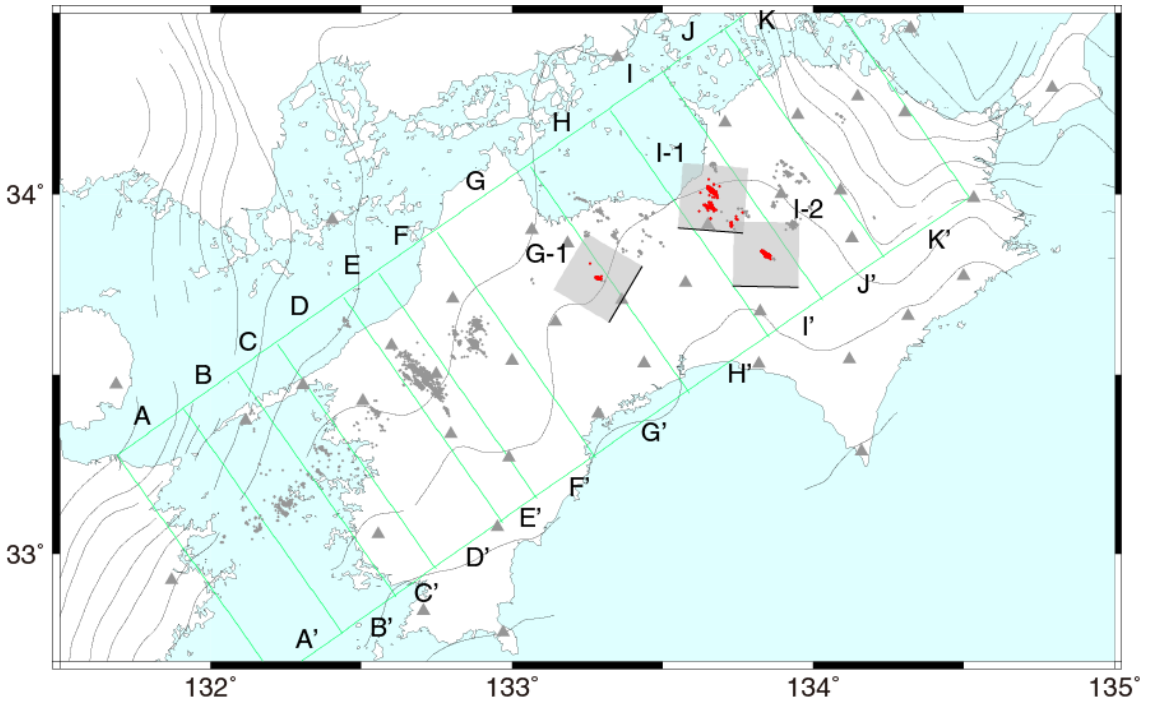

Figure 2.8: Map showing the geometries of re-estimated plate interface for subarea G and I (gray squares). The up-dip sides are indicated by solid black lines. Red dots show the relocated epicenters of LFEs used for estimation of each fault. Others are the same as Figure 2.1..

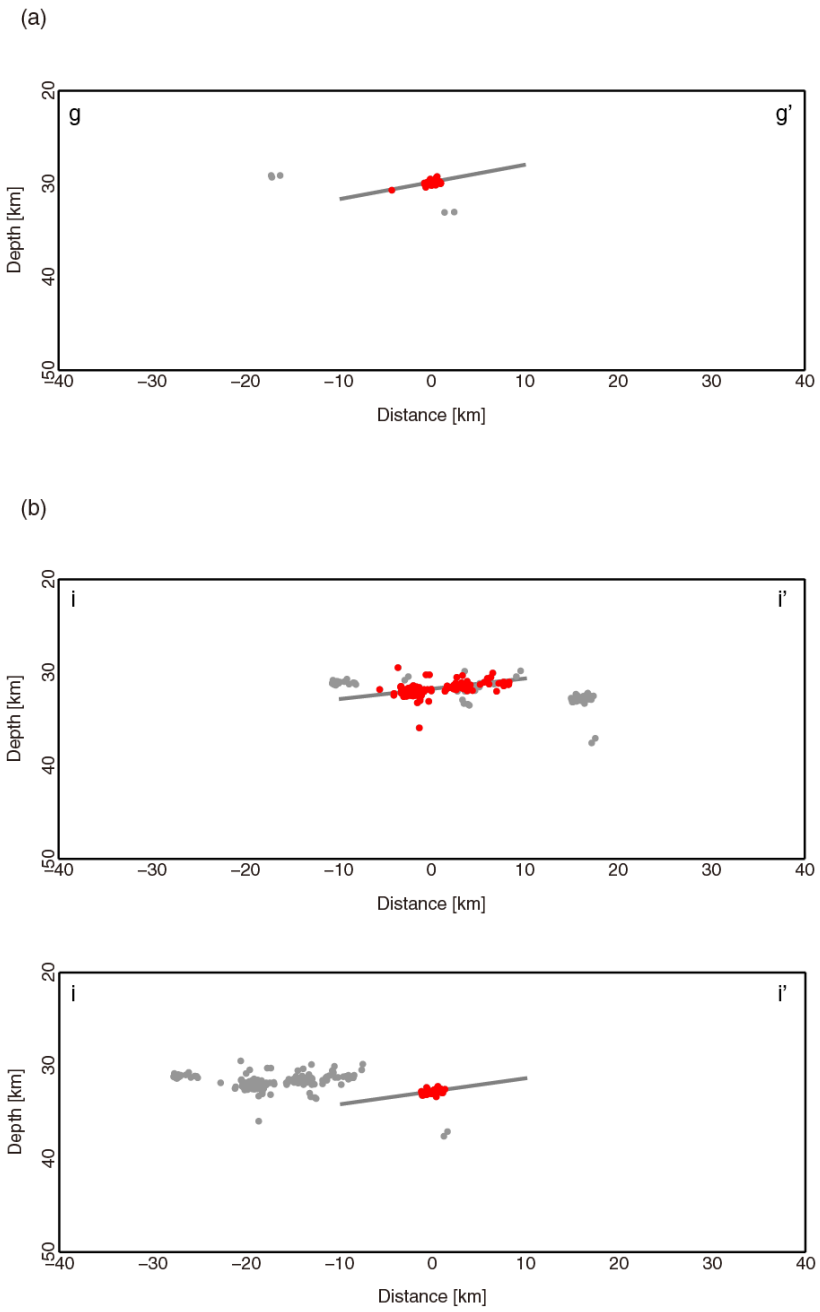

Figure 2.9: (a) Fault plane estimated by using only events within group 1 in subarea G. (b) Fault plane estimated by using only events within group 1 (upper) and group 2 (lower) in subarea I.

Table 2.1: The number of events applied and successfully relocated in each subarea.

Subarea	Events applied	Events relocated
A	166	52
B	376	164
C	141	61
D	281	87
E	876	752
F	696	607
G	115	65
H	348	160
I	744	293
J	333	238
K	29	14
Total	**4,105**	**2,493**

Table 2.2: The number of events within the groups for each subarea.

Subarea	Group ID	Events	Subarea	Group ID	Events
A	1	24	E	1	750
	2	5		2	2
	3	5	F	1	607
	4	5	G	1	60
	5	3		2	3
	6	3		3	2
	7	3	H	1	160
	8	2	I	1	179
	9	2		2	65
B	1	142		3	28
	2	7		4	6
	3	3		5	4
	4	2		6	3
	5	2		7	2
	6	2		8	2
	7	2		9	2
	8	2		10	2
	9	2	J	1	119
C	1	52		2	103
	2	4		3	7
	3	3		4	5
	4	2		5	2
D	1	50		6	2
	2	18	K	1	12
	3	14		2	2
	4	3			
	5	2			

Table 2.3: Estimated fault plane in each subarea. Standard deviations are measured vertically. G-1 and I-1(2) are estimated by using only events within group 1(2) as shown in Figure 2.7.

Subarea	Strike, Dip	Location	Standard deviation (km)
A	N234.65°E, 21.16°	33.076°N, 132.130°E, 34.93km	0.88
B	N181.98°E, 23.49°	33.157°N, 132.246°E, 35.28km	1.32
C	N207.86°E, 12.72°	33.270°N, 132.384°E, 34.04km	1.28
D	N184.21°E, 10.99°	33.440°N, 132.527°E, 34.88km	1.27
E	N178.06°E, 14.87°	33.486°N, 132.703°E, 31.12km	0.82
F	N208.69°E, 12.34°	33.602°N, 132.870°E, 31.67km	0.69
G	N53.43°E, 4.46°	33.768°N, 133.276°E, 29.95km	0.57
H	N258.34°E, 7.54°	33.914°N, 133.335°E, 31.26km	0.38
I	N16.84°E, 2.93°	33.960°N, 133.714°E, 32.01km	0.73
J	N206.80°E, 9.44°	33.992°N, 133.928°E, 30.76km	0.89
K	N316.60°E, 15.23°	34.174°N, 134.106°E, 30.95km	0.14
G-1	N209.55°E, 10.14°	33.769°N, 133.286°E, 29.88km	0.16
I-1	N274.58°E, 5.67°	33.990°N, 133.668°E, 31.83km	0.52
I-2	N273.26°E, 7.97°	33.833°N, 133.844°E, 32.82km	0.18

Chapter 3 Synthetic template waveforms

3.1 Introduction

Recent studies have shown that deep tectonic tremors in many subduction zones consist of numerous low-frequency earthquakes (LFEs) that occur as shear slips on the plate interface [e.g. Shelly et al., 2007; Ide et al., 2007]. The relative hypocenters of LFEs are determined accurately, and in western Japan, they are concentrated in a narrow zone around the anticipated plate interface [Ohta and Ide, 2011]. Therefore, the location of LFEs may constrain the instantaneous location of tremor sources and illustrate its migration behavior, as demonstrated by a matched filter analysis with template LFEs [Shelly et al., 2007].

Nevertheless, it is yet unclear whether tremor occurs at exactly the same location as LFEs. Since tremor behavior on the plate interface are various and spatially characteristic [e.g. Ide, 2010; Obara, 2011], there might be some tremor activity undetectable using template LFEs. To understand the underlying physics of tremor and other slow earthquakes, it is essential to highly resolve the spatial and temporal behavior of these events.

In this chapter, we introduce "synthetic template waveforms" to constrain the spatial and temporal evolution of tremor sources with no spatial limitations of previously observed template events. These synthetic template waveforms will be expected to work as the second key for slip inversion of tremor, that is, Green's function of tremor. For the validation of synthetic template waveforms, we perform moment tensor inversion of synthetic template waveforms and matched filter analysis using synthetic template waveforms to investigate tremor activities in the western Shikoku region.

3.2 Synthetic template waveforms

In many previous studies, the waveforms of known LFEs are used as template waveforms to catch the timing when the tremor waveforms have strong similarity with the waveforms of the templates [e.g., Shelly et al., 2007ab]. The similarity is measured by NCC across all available channels of data. However, the locations of tremor sources detected by such method are limited around known events in principle. Hence, we cannot investigate the behavior of tremor sources in the area where the catalog of previous events is insufficient. As indicated by Shelly et al. [2006], most LFEs within a certain region have similar waveforms. Their similarities were discussed in the previous chapter of the thesis. Therefore, if the typical waveform of LFE is available, we can use it as a substitute of a template waveform radiated from an imaginary source location and systematically search the locations of tremor sources from continuous seismograms. However, the moderate correlation between each pair of events measured at one station suggests that the waveform of individual event is not suitable for the representative of LFEs. Hence, we stack the waveforms of previously observed LFEs to obtain the typical waveform radiated from a point in the assumed source region. We call it as a "synthetic template waveform".

Assuming that all LFEs have the same mechanism, for a given source location we stack the waveforms of LFEs with theoretical travel time shift to obtain a synthetic template waveform. Then the l-th component of the synthetic template waveform at n-th station from a source located at $\mathbf{x}$ is expressed as follows,

$$g^{ln}(t,\mathbf{x}) = \frac{C^{ln}}{N_e}\sum_{i=1}^{N_e} W(\mathbf{x}) \cdot \frac{u^{ln}\left(t + t_0^i + T(\mathbf{x}_i,\mathbf{x}_n)\right)}{\sqrt{\int \left|u^{ln}\left(t + t_0^i + T(\mathbf{x}_i,\mathbf{x}_n)\right)\right|^2 dt}}, \qquad (3.1)$$

where $u^{ln}(t)$ is the velocity seismogram; N_e is the number of LFEs used; t_0^i is the origin time of i-th LFE; $T(\mathbf{x}_i,\mathbf{x}_n)$ is the travel time between the hypocenter of i-th LFE, $\mathbf{x}_i$ and the n-th station, $\mathbf{x}_n$. C^{ln} is the average norm given by

$$C^{ln} = \frac{1}{N_e}\sum_{i=1}^{N_e} \sqrt{\int \left|u^{ln}\left(t + t_0^i + T(\mathbf{x}_i,\mathbf{x}_n)\right)\right|^2 dt}\,. \qquad (3.2)$$

$W(\mathbf{x})$ is a weighting factor, given as follows,

$$W(\mathbf{x}) = \exp(-k|\mathbf{x}_i^0 - \mathbf{x}|). \quad (3.3)$$

As discussed in Chapter 2, even though the waveforms of neighbor events are similar, the correlations decay with inter-event distance. Therefore, the waveforms of events close to the assumed source location, **x**, should more contribute to the synthetic template waveforms rather than those of distant events. The weighting factor, $W(\mathbf{x})$, is calculated based on the distance between the source location and the hypocenter of each event. Figure 3.1 shows the logarithm of the number of strongly correlated event pairs ($\mathrm{NCC} > 6.0\,\sigma_{\mathrm{NCC}}$) against the distance between their hypocenters, which is obtained from the analysis in Chapter 2. The similarity of the waveforms of two events generally decreases with distance between the events. We fit an exponential curve to this plot and use its slope as an empirical weighting factor. The constant k in equation (3.3) is $k = 0.7\,[km^{-1}]$ in this case and we use this value through all analyses in the thesis.

3.3 Data and study area

We use 3 components of the velocity seismograms recorded by the densely high-sensitivity seismograph network (Hi-net) maintained by NIED. Each seismogram is band-pass filtered between 2-8 Hz, and resampled to 20 samples per second.

We focus the activities of the tremor in the western Shikoku region shown in Figure 3.2. This region contains the clusters of LFEs which are known for very high activity. Figure 3.2 shows the distribution of 607 LFEs relocated by NCC method in Chapter 2. We assume that tremors occur on a fault plane, which was a plane fitted to the LFE distribution in Chapter 2. The fault plane has a strike of $\mathrm{N}208.69°\mathrm{E}$ and $12.34°$ dip and the center is located at $33.602°\mathrm{N}, 132.870°\mathrm{E}$ and at the depth of 31.67 km which coincides with the centroid of LFEs. The length and width of the fault model are both 16km. We assign 4,425 nodes with interval of 250m on the plane for origins of the synthetic template waveforms. Using the waveforms of 607 LFEs, we calculate each component of the synthetic template waveforms at every station for every node. We refer to these imaginary sources as synthetic template events or just as template events here.

We use only S-wave of synthetic template waveforms to save the computational cost. Because the source depths are constrained to the fault plane in this study, differential arrivals of S-waves provide sufficient information to distinguish the source locations. The time window used for calculating synthetic template waveforms is from 1.5 s before to 2.5 s after the theoretical S-wave arrival times.

Figure 3.3 shows an example of the synthetic template waveforms. The EW component of the synthetic template at the station, OOZH, is demonstrated here. The source location is assumed to $\mathbf{x}_c = (33.602°\mathrm{N}, 132.870°\mathrm{E}, 31.67\mathrm{km})$, which corresponds to the center of the fault. Note that stacking the seismograms cleans up the noises clearly enough to see the signal of LFEs.

3.4 Numerical test

Before the analysis using the synthetic template waveforms synthesized from real data, we carried out a numerical test to check the usability of synthetic template waveforms, using theoretically calculated waveforms from a set of double-couple point sources. We place 607 sources at the same locations with the hypocenters of LFEs in the western Shikoku. We theoretically calculate three components of velocity waveforms for all source locations, $u_{clc}(t, \mathbf{x}_i^{LFEs})$ $(i = 1, \ldots, 607)$, at actual 9 Hi-net stations in the western Shikoku with a common low-angle thrust mechanism of (strike, dip, rake) = (208°, 12°, 100°). The time function of each source is 0.3 s in duration with a simple triangular shape. We use a discrete wave number method incorporating attenuation for a layered structure [Takeo, 1987] to calculate Green's functions. The synthetic template waveforms for each node on the model fault, $g_{clc}(t, \mathbf{x}_j^{fault})$, are obtained by stacking these theoretically calculated waveforms, $u_{clc}(t, \mathbf{x}_i^{LFEs})$, following equation (3.1). We also calculate theoretical waveforms for each node on the fault, $u_{clc}(t, \mathbf{x}_j^{fault})$. Then the discrepancy between $g_{clc}(t, \mathbf{x}_j^{fault})$ and $u_{clc}(t, \mathbf{x}_j^{fault})$ is evaluated.

Figure 3.4a shows the distribution of variance reduction (VR) for every 4 nodes (1 km interval) on the fault which is defined by

$$VR(\mathbf{x}_j) = 1 - \frac{\sum_{l,n,k}\left|u_{clc}^{ln}(t_k,\mathbf{x}_j) - g_{clc}^{ln}(t_k,\mathbf{x}_j)\right|^2}{\sum_{l,n,k}\left|u_{clc}^{ln}(t_k,\mathbf{x}_j)\right|^2}, \tag{3.4}$$

where $u_{clc}^{ln}(t_k,\mathbf{x}_j)$ and $g_{clc}^{ln}(t_k,\mathbf{x}_j)$ are l-th component of theoretical and synthetic template waveforms at n-th station from a source located at $\mathbf{x}_j$, respectively. The synthetic template waveforms at the portions close to the clusters of LFEs explain the theoretical ones well, whereas they are less matched at several portions apart from the clusters. This is because the synthetic template waveforms at such portions cannot explain amplitude patterns among stations of theoretical ones well. Figure 3.4b shows the distribution of cross-correlation coefficients (CC) between the synthetic template waveforms and the theoretical ones averaged among components given by

$$CC(\mathbf{x}_j) = \frac{1}{3N_s}\sum_{ln}\frac{\sum_k u_{clc}^{ln}(t_k,\mathbf{x}_j)g_{clc}^{ln}(t_k,\mathbf{x}_j)}{\sqrt{\sum_k\left|u_{clc}^{ln}(t_k,\mathbf{x}_j)\right|^2\sum_k\left|g_{clc}^{ln}(t_k,\mathbf{x}_j)\right|^2}}, \tag{3.5}$$

where N_s is the number of stations. Each CC value is larger than 0.7 which is enough for event detection in cross correlation study such as matched filter analysis. Figure 3.4c shows the distribution of the ratio (R) of L2-norms between the synthetic template waveforms and the theoretical ones given by

$$R(\mathbf{x}_j) = \frac{\sum_{l,n,k}\left|g_{clc}^{ln}(t_k,\mathbf{x}_j)\right|^2}{\sum_{l,n,k}\left|u_{clc}^{ln}(t_k,\mathbf{x}_j)\right|^2}. \tag{3.6}$$

L2-norms of the synthetic template waveforms are larger than that of the theoretical ones at the west side on the fault and smaller at the east side on the fault. This suggests that the slip amounts on the fault estimated using the synthetic template waveforms tend to be smaller than true values at the west side and larger at the east side.

3.5 Moment tensor inversion

When we calculate the synthetic template waveforms for an assumed source location using the actually observed waveforms of LFEs, that synthetic template event should have typical focal mechanism and source time function of LFEs. For the evaluation of the mechanism and source time

function of synthetic template events, we conduct a moment tensor inversion. The observation equation is written as,

$$\boldsymbol{g}(t_k, \mathbf{x}) = \sum_l f(t_k - t_l) \sum_{j=1,5} m_j \boldsymbol{g}_j^0(t_l) + \boldsymbol{e}(t_k), \quad (3.7)$$

where $\boldsymbol{g}(t_k, \mathbf{x})$ is the synthetic template waveform from a source location, $\mathbf{x}$, calculated by using the waveforms of previously observed LFEs following equation (3.1). We assume a source time function of the synthetic template event, $f(t_k)$, to be a single node linear spline function. m_j are five unknown parameters and $\boldsymbol{g}_j^0(t_k)$ are Green's functions which correspond to a set of basis moment tensors, respectively. $\boldsymbol{e}(t_k)$ is an error vector. We calculate Green's functions theoretically using an algorithm to calculate Green's functions for a layered structure [Takeo, 1987]. We estimate both source duration and five model parameters in equation (3.7). For an assumed duration, the maximum likelihood solution is obtained from the linear least squares method [e.g., Menke, 1989]. Then the variance reduction (VR) is defined as,

$$VR = 1 - \frac{\sum_i \|\boldsymbol{e}(t_i)\|^2}{\sum_i \|\boldsymbol{g}(t_i, \mathbf{x})\|^2}. \quad (3.8)$$

The optimum source duration is determined by maximizing VR and examined between 0.05 and 0.6 s in 0.05 s steps by a grid search method.

We apply the above inversion procedure to the synthetic template event located at $\mathbf{x}_c$, where $\mathbf{x}_c$ is the center of the fault as described before. Figure 3.5 shows the focal mechanism of the synthetic template event and comparison between data and calculated waveforms. The beach ball indicates low-angle thrust fault dipping to north-west, which is consistent to the focal mechanism of LFEs in the western Shikoku region estimated by Ide et al. [2007]. The seismic moment is measured to be 2.7×10^{10} Nm (M_w 0.84). The source duration is estimated to be 0.3 s (Fig. 3.6). The final VR of 27.7% seems far from perfect. In fact, the theoretically calculated waveforms are not suitable for explaining the observed ones with frequency higher than ~1 Hz [e.g., Ide et al., 2005] due to uncertainty of velocity structure. Hence, these estimates of seismic moment and source duration should be considered as one of possible solutions that do not contradict observation.

Figure 3.7 shows the focal mechanisms of synthetic template events on the fault. Those mechanisms are obtained for every 4 nodes (1 km interval) by solving equation (3.7), but the source time duration is fixed to 0.3 s here. The

seismic moments and VR range from 2.1 to $3.2 \times 10^{10}\ Nm$ and from 21.5% to 31.8%, respectively. Each mechanism is slightly different but nearly identical.

3.6 Matched Filter Analysis

We next perform the matched filter analysis using the synthetic template waveforms to confirm the detectability of tremor sources. The running cross-correlation between the synthetic template waveforms and continuous seismograms is used to evaluate the similarities. NCC across many stations stands at a significantly high value when the synthetic template waveforms from the assumed source location and continuous seismograms are highly correlated, then we obtain the time and the location of a tremor source.
For the template event located at $\mathbf{x}$, NCC at the time t is given by

$$\mathrm{NCC}(\mathbf{x}, t) = \sum_{ln} \frac{\sum_m u_m^{ln}(t + \tau(\mathbf{x}, \mathbf{x}_n)) g_m^{ln}(\mathbf{x})}{\sqrt{\sum_m \left(u_m^{ln}(t + \tau(\mathbf{x}, \mathbf{x}_n))\right)^2 \sum_m \left(g_m^{ln}(\mathbf{x})\right)^2}}, \qquad (3.9)$$

where $u_m^{ln}(t)$ is the ground velocity seismogram of m-th time step around reference time t in l-th direction at n-th station, $g_m^{ln}(\mathbf{x})$ is the synthetic template waveforms derived for $\mathbf{x}$, and $\tau(\mathbf{x}, \mathbf{x}_n)$ denotes the theoretical travel time from $\mathbf{x}$ to the station $\mathbf{x}_n$.
The detection threshold is set at 7 times standard deviation (SD) of NCC and SD is calculated independently for each synthetic template and each day of continuous data. At this value, the expected number of false detection for each template is 1.6×10^{-3} for the application to 4 years record with time lag of 0.1 s. To eliminate duplicate detection we count only one event which has the highest NCC within each 4 second window.
We analyze the continuous seismograms recorded at 9 Hi-net stations which surround and enclose the source area (Figure 3.2) for 4 years from January 2005 to December 2008.

An example of detection is shown in Figure 3.8. Each cross-correlation coefficient is not always high and the average is about 0.63. However, NCC is about 9*SD which is statistically high value (probability of exceedance of $\sim 1.13 \times 10^{-19}$ for a Gaussian distribution) enough to distinguish signals of

LFEs from noises.

Figure 3.9a shows the histogram of the number of detected events. We detect 38,715 events for 4 years in total whereas the number of LFEs in JMA catalog within the same period is 282. The large tremor burst episode occurs repeatedly at intervals of about 180 days, which is consistent to the recurrence interval of tremor in this region reported in Obara et al. [2010]. We further focus on the activity of one burst episode on March, 2008. Figure 3.9b shows the histograms of detected events on this month. The episode continues for 12 days from 16 to 27 March and the number of detected events is 2,205 in total. The activity is the highest in the first day and decay rapidly. Figure 3.10 and 3.11 demonstrates an example of migration of detected events. Figure 3.10 shows the continuous seismograms for 1 hour from 23:00:00 on 16 March, 2008 which contains migrating tremor sources. 31 events are detected within the latter 30 minutes. Each waveform is colored at the timing of detection and color is coded by time. Figure 3.11 shows locations of detected sources within the same time window. The sources are located in the southern part of the fault in the beginning and gradually shift toward the north. The migrating velocity along the north south direction is roughly measured by first and last detected source locations in this sequence and estimated to be about 20km/h, which is comparable to typical short-term migration velocity of tremor sources in the dip direction [e.g., Shelly et al., 2007b; Ghosh et al., 2010].

3.7 Discussion and Conclusion

We introduce the synthetic template waveforms as the representatives of typical constituents of tremor sources in a certain source area. The stacking procedure of known LFEs with appropriate time shifts renders the signal of tremor source prominent. By assigning theoretical differential times among the stations, we can use the synthetic template waveforms as the waveforms derived for the imaginary sources.

The focal mechanism estimated by moment tensor inversion shows low angle thrust faults, which supports the idea that LFEs are shear slips on the plate interface. Although the analysis is not very reliable due to insufficient knowledge of Green's functions, it is notable that all estimated parameters including focal mechanisms, seismic moment, and source duration are likely values.

We conduct a matched filter analysis using synthetic template waveforms to investigate tremor activities in the western Shikoku region. The synthetic template waveforms introduced here work well for detection and the detectability is over 100 times larger than that of the ordinary method adopted by JMA. The recurrence interval of tremor burst episode is consistent to that is reported in Obara et al. [2010]. The daily frequency of tremor within one burst episode shows very high activity in the beginning (Figure 3.9b). The number of detected events in the first three days is 1,500, which is about 70% of total number in this episode. This might be related to the back ground SSE event, and the detailed investigation will be done in the next Chapter. The striking feature of tremor, migrating behavior is also clearly shown here (Figure 3.11). The tremor sources seem to propagate radially from the initiation, it is difficult to determine its migration velocity. The average migrating velocity of ~20km/h is the same order as the migrating velocity of LFEs along dip direction reported in Shelly et al. [2007]. Although the image of tremor source migration obtained here is still temporally discrete, the analysis shows the potential of the synthetic template waveforms to investigate the detailed slip evolution of tremor.

In the next chapter, we try to deduce more temporally detailed image of tremor evolution. We will develop the slip inversion method using synthetic template waveforms introduced here as empirical Green's function. The slip

history of tremor will be quantitatively evaluated, and the comparison between the tremor and VLF will be shown and discussed further.

Figures

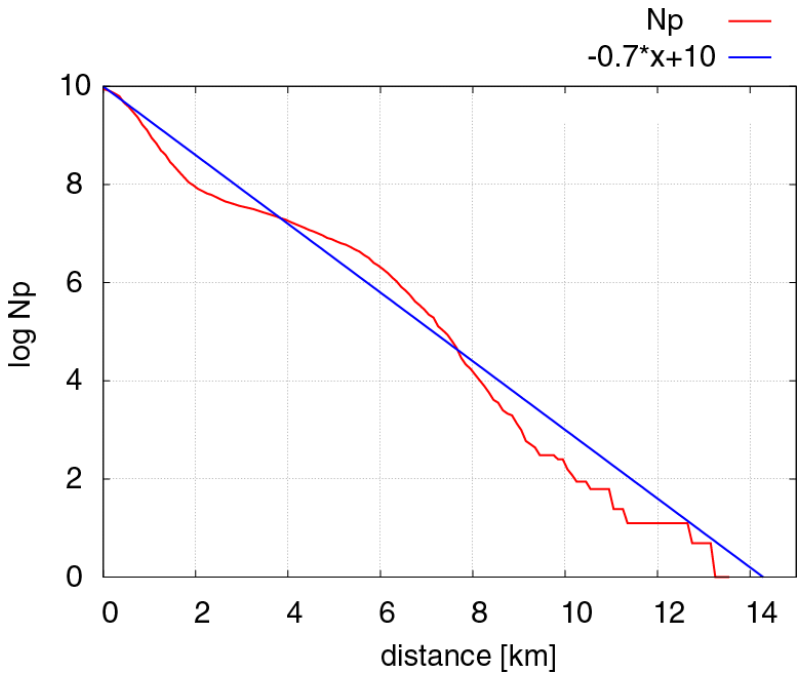

Figure 3.1: Relationship between waveform similarity and inter-event distance of LFEs in the study area. Red curve shows logarithm of cumulative number of event pairs which have NCC over 6.0*SD. Blue line shows an exponential curve, $\log N_p = \exp(-0.7x + 10)$.

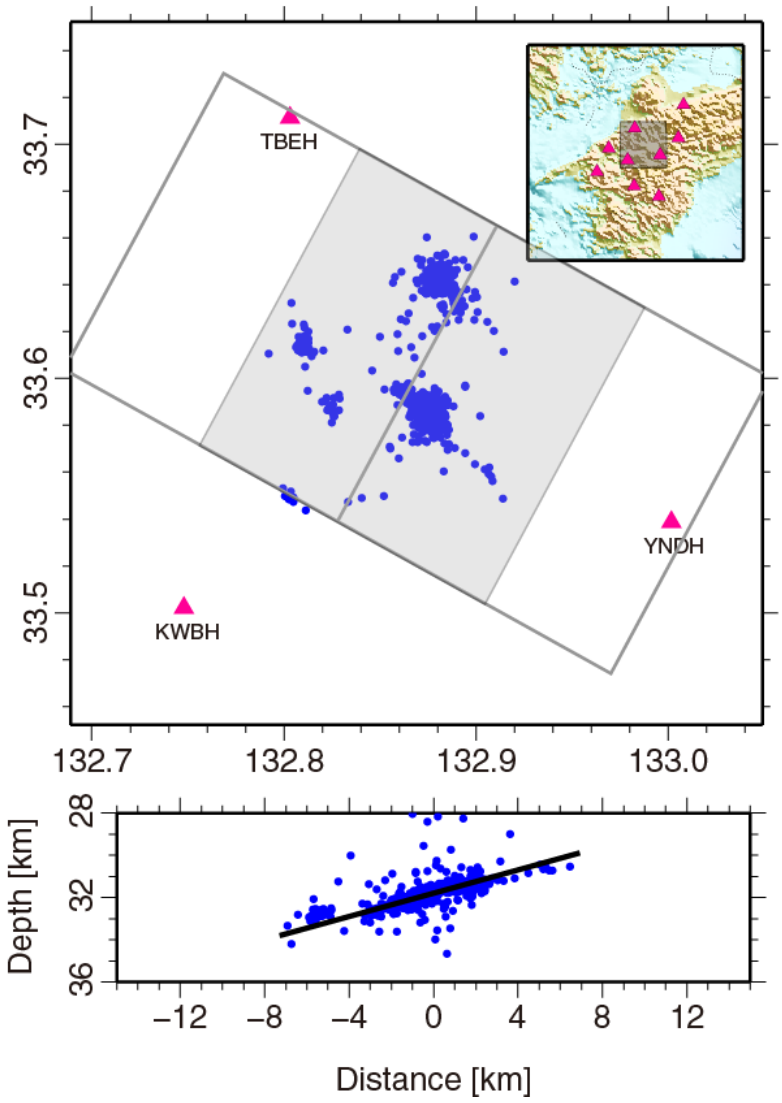

Figure 3.2: The assumed fault plane in the western Shikoku region is shown by a gray shadow rectangle (upper panel) and black line (lower panel). Blue circles show the hypocenter locations of LFEs which are relocated by NCC method in Chapter 2.

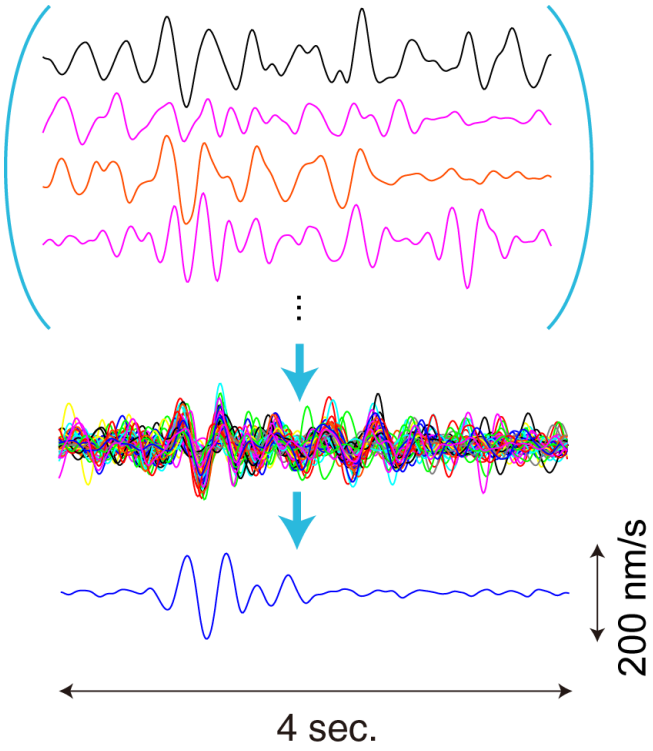

Figure 3.3: Example of a synthetic template waveform. Color lines show EW components of velocity seismograms of 607 LFEs recorded at OOZH station. Blue line shows a resultant synthetic template waveform.

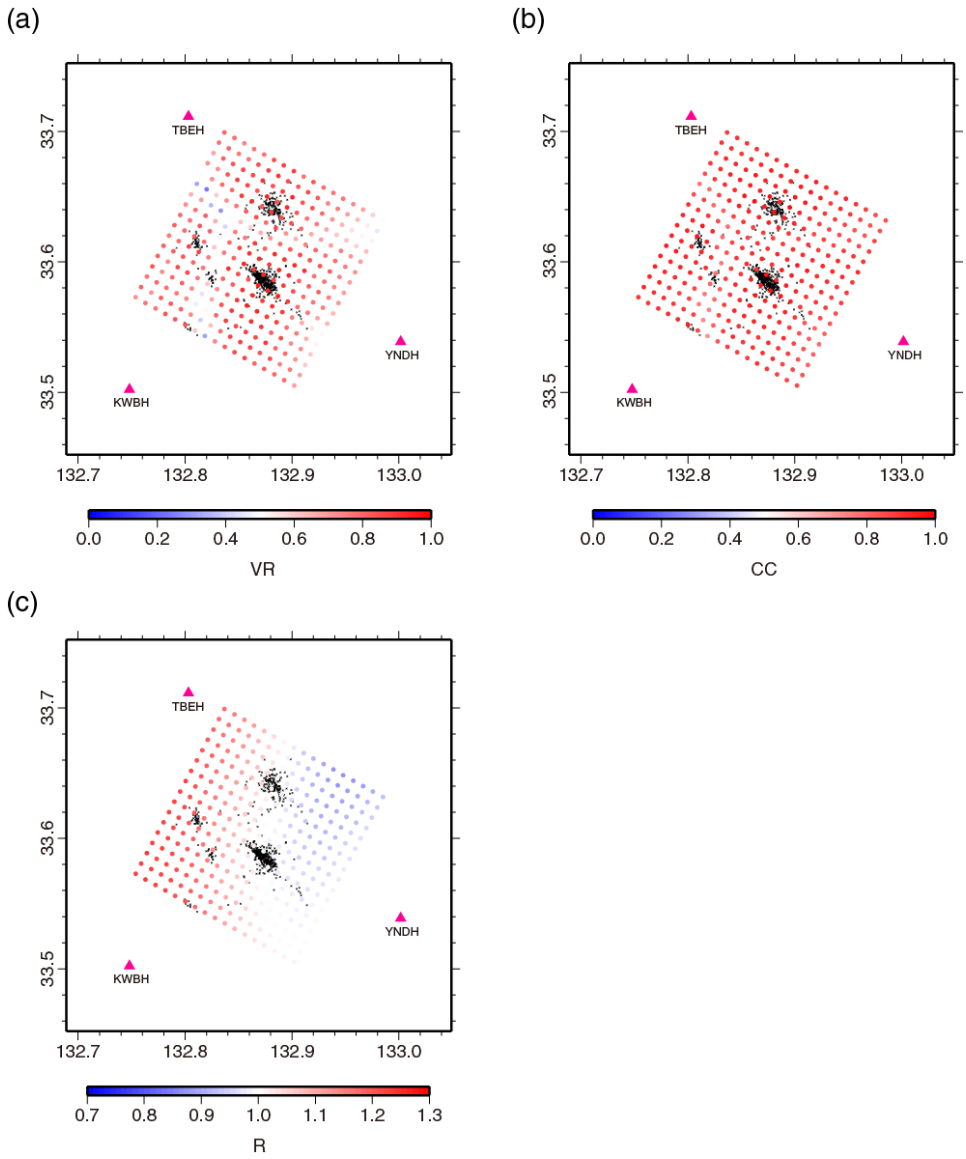

Figure 3.4: Result of numerical test. Black dots show the locations of sources for calculation of the synthetic template waveforms, placed at the same locations of LFEs in the western Shikoku region. Color circles denote the distribution of variance reductions (a), averaged cross-correlation coefficients (b), and L2-norm ratios (c) between the synthetic template waveforms and theoretical waveforms at each node on the assumed fault. Red triangles show Hi-net stations.

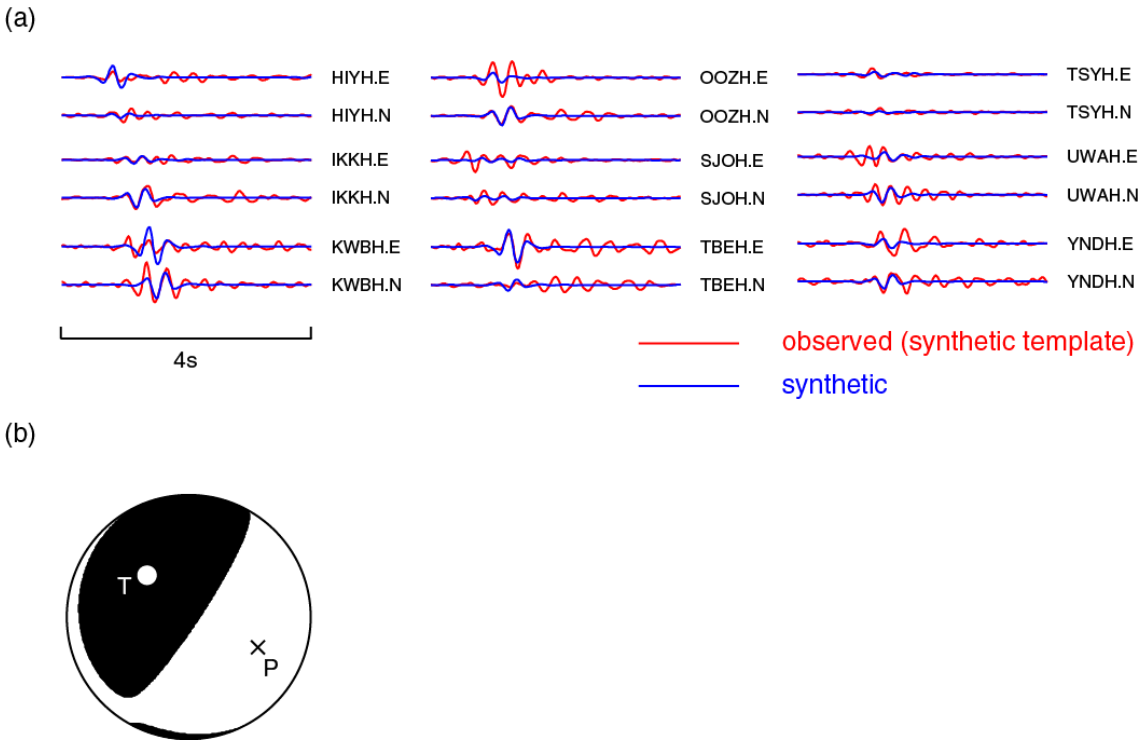

Figure 3.5: Estimated moment tensor solution. (a) The comparison of observed (red lines) and synthetic (blue lines) seismograms. (b) The obtained focal mechanism.

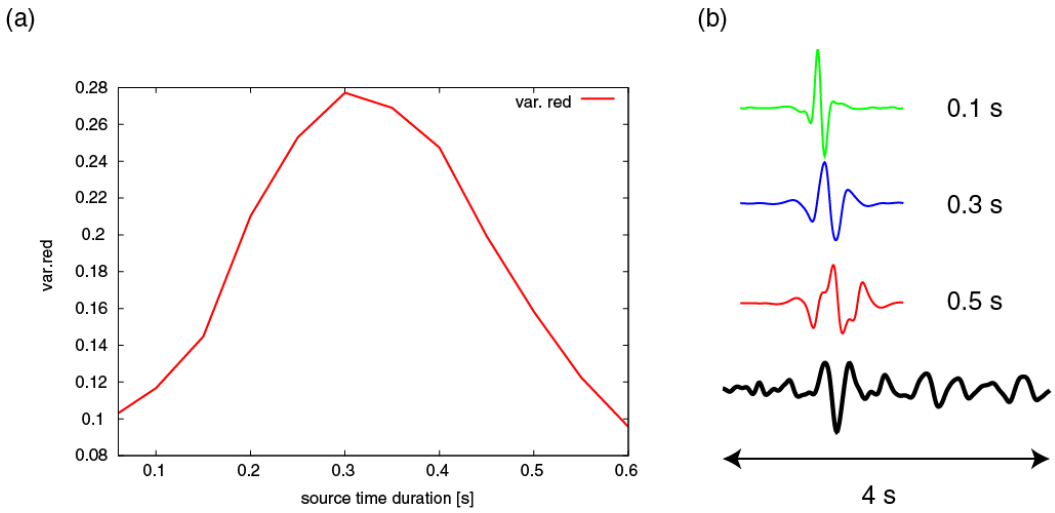

Figure 3.6: (a) Variation of VR with source duration. (b) Examples of the variation of synthetic seismograms with source duration. Green, blue, and red lines represent EW component of the theoretically calculated seismograms for 0.1, 0.3 (best fit), and 0.5 s of source duration at the TBEH station. Black line shows EW component of the synthetic template waveform at the TBEH station.

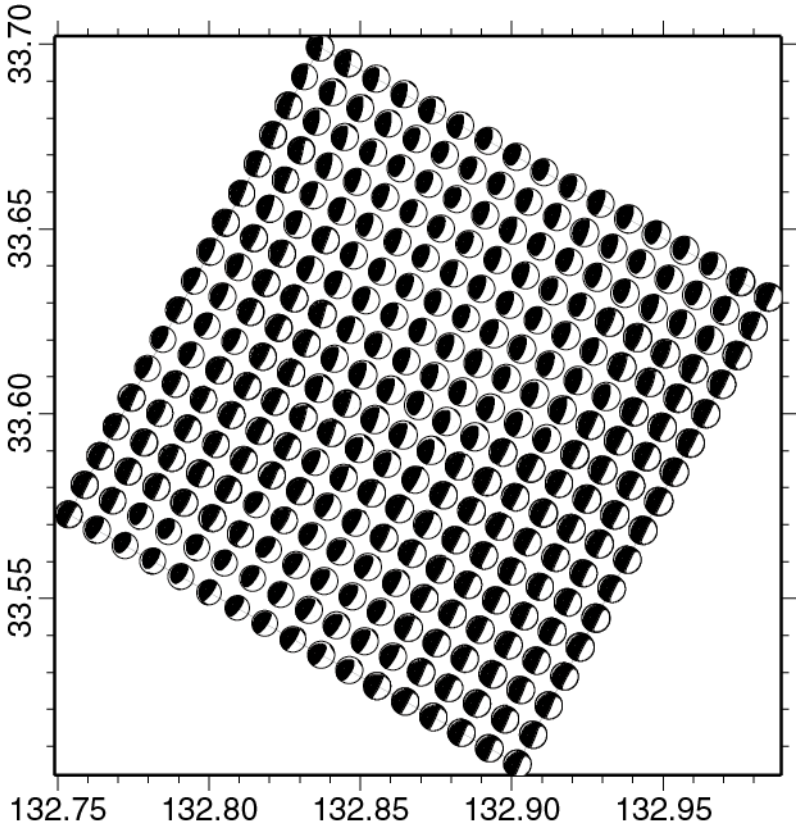

Figure 3.7: The distribution of estimated focal mechanisms of synthetic template events located at 289 nodes with interval of 1km on the assumed fault.

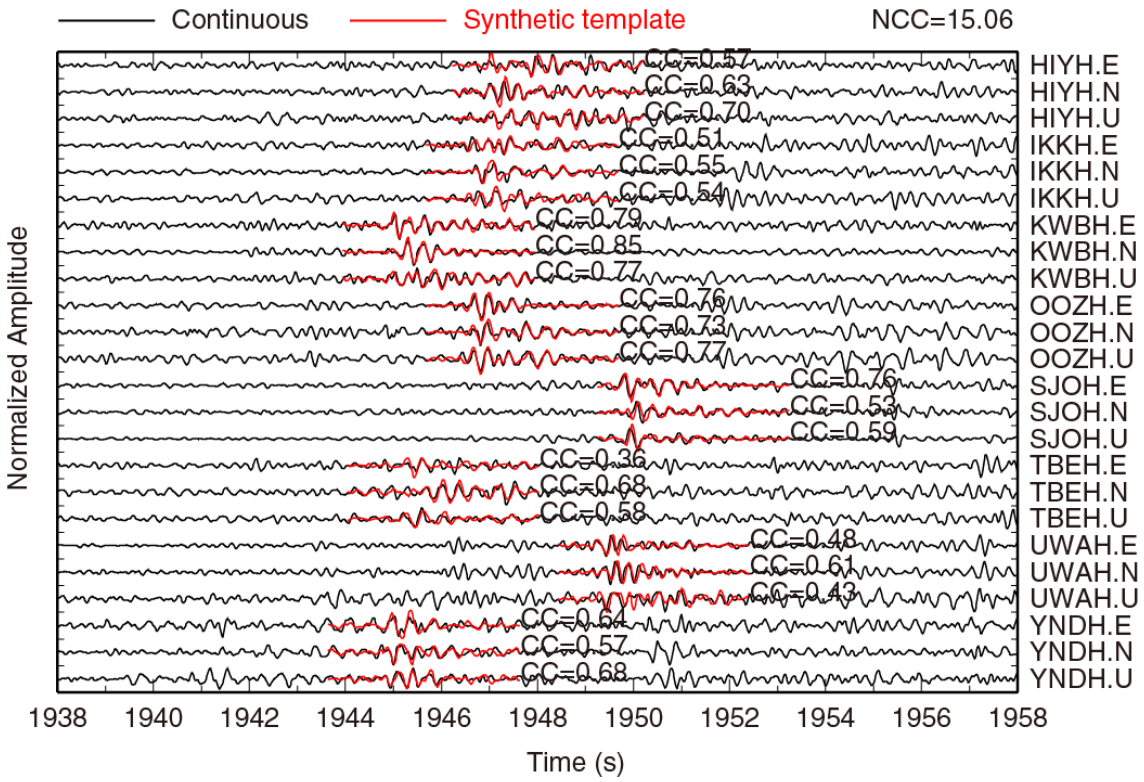

Figure 3.8: An example of detection. Continuous tremor waveforms are shown in black and synthetic template waveforms in red for each component. Cross-correlation coefficient for each trace is shown next to the synthetic template waveforms.

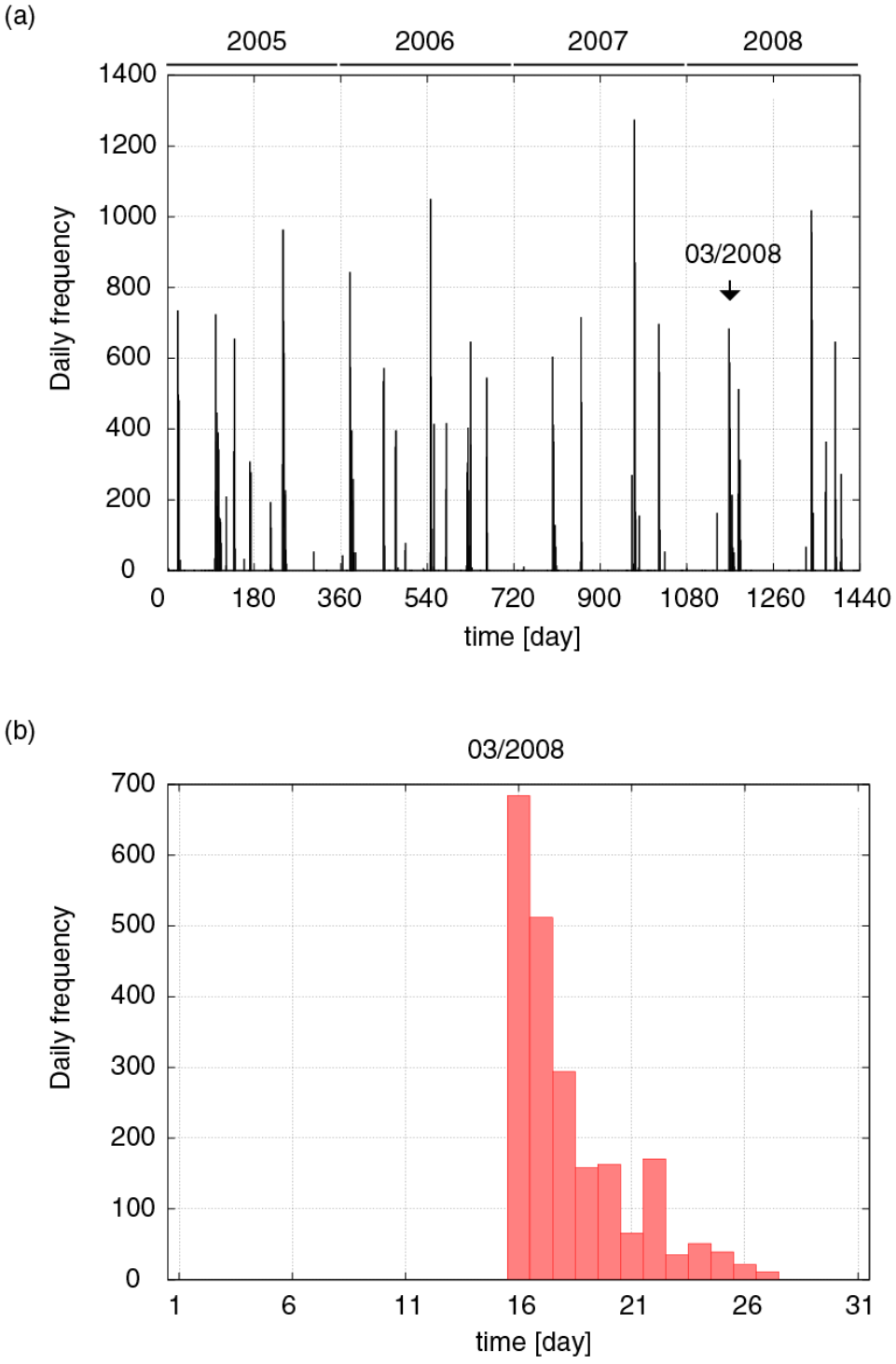

Figure 3.9: Histogram of detected events. (a) The number of detected events for each day is plotted during 4 years from 2005 to 2008. (b) Close-up of the histogram during March, 2008 which includes a tremor burst episode indicated by the arrow in (a).

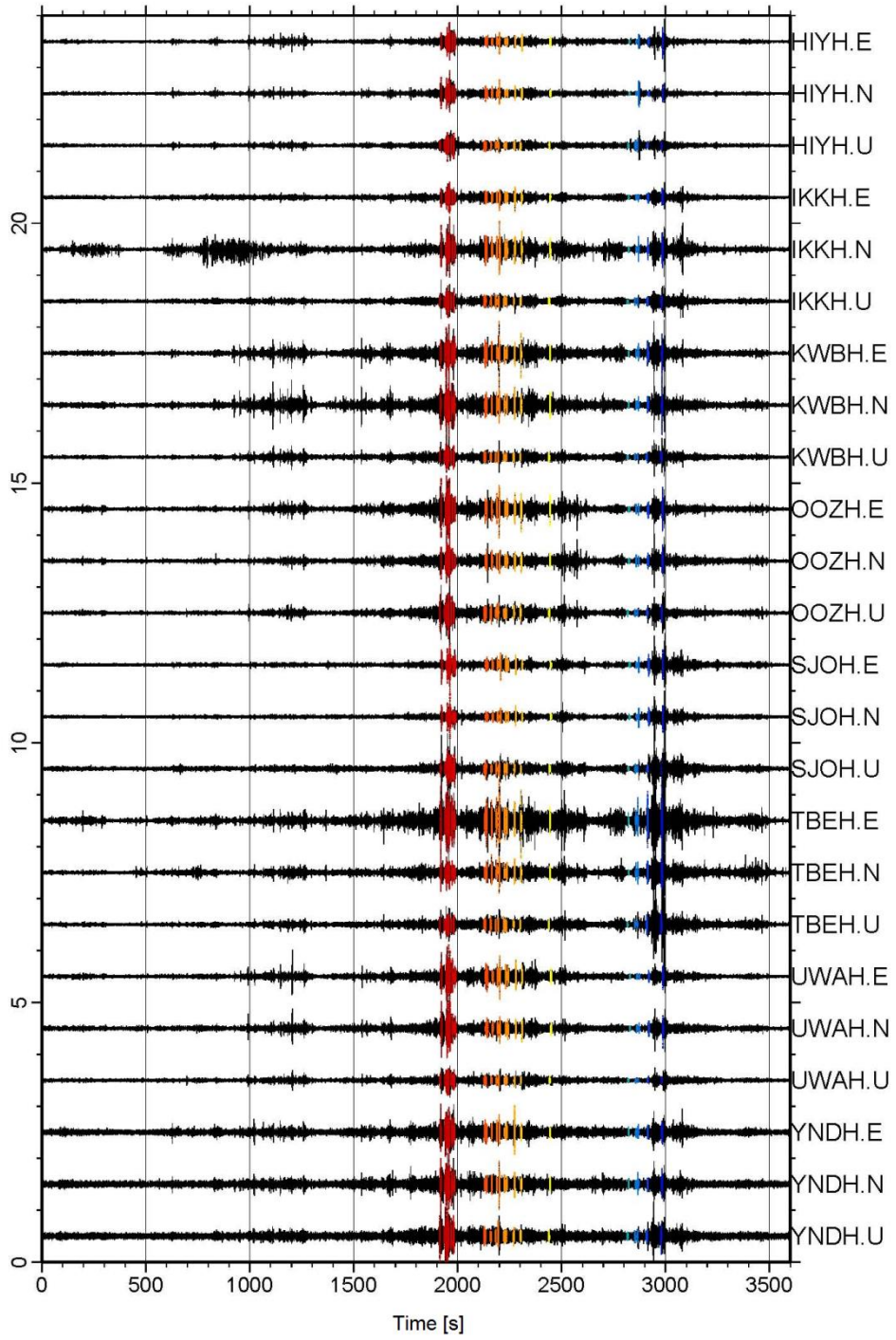

Figure 3.10: Continuous tremor waveforms for each component at 23:00:00 on 16 March, 2008 are shown. Colored portions of waveforms indicate times of detections. Color is coded with time.

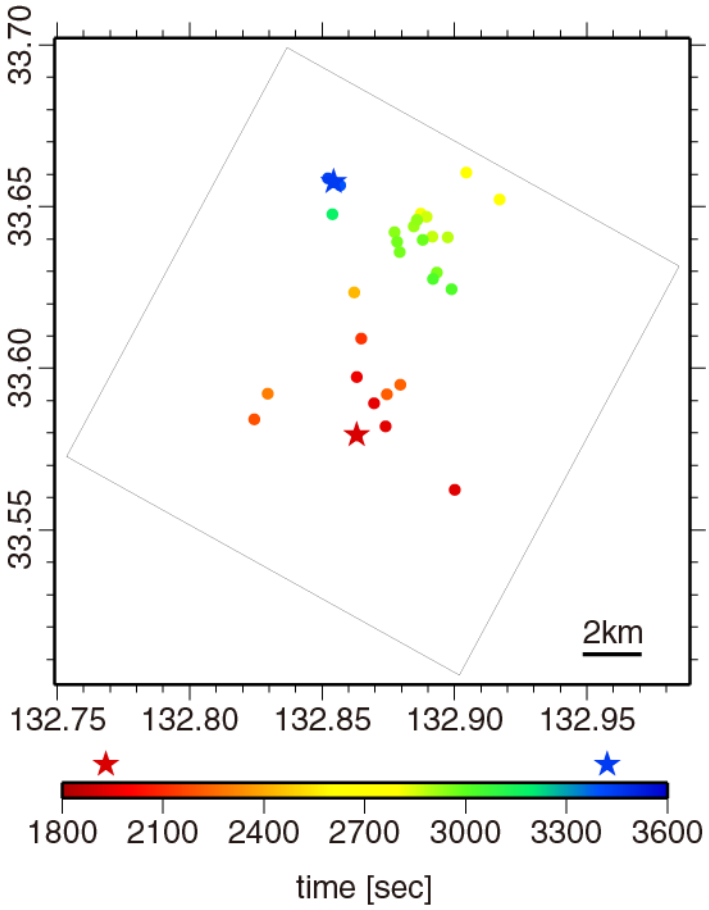

Figure 3.11: Space-time distribution of detected tremor sources within 1 hour time window from 23:00:00 on 16 March, 2008. Color circles indicate locations of detected events on the fault with the same color scale as Figure 3.10. Gray rectangular indicates the assumed fault plane. Red and blue stars indicate first and last detected sources of this migration episode, respectively.

Chapter 4 Slip inversion of continuous tremor

4.1 Introduction

Recent studies suggested heterogeneities on the plate boundary affect the occurrences of tremors and slow earthquakes. Obara [2010] and Obara et al. [2010] discovered the difference in recurrence interval of tremor activity among segmented regions located in parallel to the trench, together with some depth dependent variation of temporal tremor activity. Ide et al. [2010] also suggested the spatially characteristic behavior of tremor including tidal response and duration of tremor. Similar characteristics are also reported in tremors associated with ETS in Cascadia subduction zone [e.g. Wech et al., 2009; Wech and Creager, 2011]. These observations imply that the heterogeneities on the plate boundary, such as frictional property, play important roles about the generation of tremors and slow slips.

Ando et al. [2010] explained the tremor generation by a numerical model including many small brittle patches surrounded by ductile slow slip region. This model predicts that the patch density and viscosity are important factors controlling the slip behavior of tremor [Nakata et al., 2011].

Although the macroscopic characteristics of tremor have been examined by many recent studies, the spatially and temporally detailed slip behavior is not investigated well. Quantitative evaluation of the slip evolution of tremor might enable more realistic modeling of tremor generation.

In the preceding chapters, we obtained the accurate fault locations and synthetic template waveforms as typical waveforms of tremor/LFEs. We also demonstrated the validity of synthetic template waveforms for tracking the tremor sources in an episode. We finally proceed to develop a non-linear slip inversion method of continuous tremor waveforms using synthetic templates and investigate the detailed slip evolution of tremor in the Shikoku region.

From the result of slip inversion, detailed discussion associated with the slip behavior of tremor will be explicated.

4.2 Theoretical background of slip inversion method for tremor

Observation equation

We model a rupture process of tremor as a sequence of point sources which have the same focal mechanism as that of LFEs. Then the l-th component of observed ground velocity at n-th station, $u^{ln}(t)$, is expressed as follows

$$u^{ln}(t) = \sum_i a_i s\big(t - t_i + T(\mathbf{x}_i, \mathbf{x}_n)\big) * G^{ln}(t, \mathbf{x}_i) + e^{ln}(t), \qquad (4.1)$$

where $G^{ln}(t, \mathbf{x}_i)$ is theoretical velocity function from shear slip located at $\mathbf{x}_i$ with a unit step time function and unit source area. The direction of the shear slip is the same as that of LFEs. $s(t)$ is a temporal basis function for each source, which is assumed as a linear spline function with a constant duration. $T(\mathbf{x}_i, \mathbf{x}_n)$ is a theoretical travel time between $\mathbf{x}_n$ and $\mathbf{x}_i$. a_i is an expansion coefficient, and $e^{ln}(t)$ is an error vector. The time function $s(t)$ is normalized as $\int s(t)dt = 1$, so that the slip amount of i-th source is a_i.

In Chapter 3, assuming all LFEs have the same mechanism, we introduce the synthetic template waveforms as typical waveforms of LFEs on the fault. We use the synthetic template waveform as substitutes of the theoretical velocity function in equation (4.1). Note that the source of this synthetic template waveform has a finite area, a finite duration, and the seismic moment of LFEs. Therefore, we rewrite equation (4.1) as follows

$$u^{ln}(t) * f(t) = \sum_i a'_i s\big(t - t_i + T(\mathbf{x}_i, \mathbf{x}_n)\big) * g^{ln}(t, \mathbf{x}_i) + e^{ln}(t), \qquad (4.2)$$

where

$$g^{ln}(t, \mathbf{x}_i) \sim (M_0^{st}/\mu) G^{ln}(t, \mathbf{x}_i) * f(t)$$
$$\int f(t)dt = 1 \qquad (4.3)$$
$$a'_i = a_i/(M_0^{st}/\mu).$$

$f(t)$ is the source time function of the synthetic template waveform which is assumed to be a linear spline function with the duration constrained by moment tensor inversion in Chapter 3.5. $g^{ln}(t, \mathbf{x}_i)$ is the synthetic template waveform derived for $\mathbf{x}_i$. M_0^{st} is seismic moment of synthetic template events which is also estimated by moment tensor inversion in Chapter 3.5. In the analysis, all synthetic template events on the fault are assumed to have the same value of seismic moment, M_0^{st}. μ is the rigidity and M_0^{st}/μ is the normalization constant.

Equation (4.2) is simplified as follows

$$v^{ln}(t) = \sum_i a'_i h^{ln}(t - t_i, \mathbf{x}_i) + e^{ln}(t), \tag{4.4}$$

where

$$v^{ln}(t) = u^{ln}(t) * f(t), \tag{4.5}$$

$$h^{ln}(t - t_i, \mathbf{x}_i) = s(t - t_i + T(\mathbf{x}_i, \mathbf{x}_n)) * g^{ln}(t, \mathbf{x}_i). \tag{4.6}$$

Then the best fit solution is obtained by minimizing the approximation error given by

$$\Delta = \sum_{l,n} \int \left[v^{ln}(t) - \sum\nolimits_i a'_i h^{ln}(t - t_i, \mathbf{x}_i) \right]^2 dt. \tag{4.7}$$

Iterative deconvolution

Due to the limitation of computational resources, we search the solution of equation (4.4) iteratively following the method introduced by Kikuchi and Kanamori [1982; 1986; 1991]. The schematic of the iteration procedure is shown in Figure 4.1. First we take a single wavelet to determine a set of parameters a'_1, t_1, and $\mathbf{x}_1$ by minimizing the error defined by

$$\Delta_1 = \sum_{l,n} \int [v^{ln}(t) - a'_1 h^{ln}(t - t_1, \mathbf{x}_1)]^2 \, dt. \tag{4.8}$$

For the sake of simplicity, we rewrite equation (4.8) in terms of correlation function as follows

$$\Delta_1 = r_{vv}(0) - 2a'_1 r_{vh}(t_1, \mathbf{x}_1) + a'^2_1 r_{hh}(0, \mathbf{x}_1), \tag{4.9}$$

where

$$r_{vv}(t) = \sum_{l,n} \int v^{ln}(\tau) v^{ln}(t + \tau) \, d\tau, \tag{4.10}$$

$$r_{vh}(t, \mathbf{x}) = \sum_{l,n} \int v^{ln}(t + \tau) h^{ln}(\tau, \mathbf{x}) \, d\tau, \tag{4.11}$$

$$r_{hh}(t, \mathbf{x}) = \sum_{l,n} \int h^{ln}(\tau, \mathbf{x}) h^{ln}(t + \tau, \mathbf{x}) \, d\tau. \tag{4.12}$$

For fixed t_1 and $\mathbf{x}_1$,

$$\frac{\partial \Delta_1}{\partial a'_1} = 2[-r_{vh}(t_1, \mathbf{x}_1) + a'_1 r_{hh}(0, \mathbf{x}_1)]. \tag{4.13}$$

Hence, the error Δ_1 is minimized if

$$\frac{\partial \Delta_1}{\partial a'_1} = 0 \quad or \quad a'_1 = \frac{r_{vh}(t_1, \mathbf{x}_1)}{r_{hh}(0, \mathbf{x}_1)}. \tag{4.14}$$

For this value of a'_1,

$$\Delta_1 = r_{vv}(0) - \frac{[r_{vh}(t_1, \mathbf{x}_1)]^2}{r_{hh}(0, \mathbf{x}_1)}, \tag{4.15}$$

which takes the minimum value when

$$[r_{vh}(t_1, \mathbf{x}_1)]^2 = maximum. \tag{4.16}$$

In this study, we assume a'_i is always positive. Therefore, we seek t_1 and $\mathbf{x}_1$ which satisfy

$$r_{vh}(t_1, \mathbf{x}_1) = maximum. \tag{4.17}$$

The next source is derived from the residual waveform,

$$v^{ln\,\prime}(t) = v^{ln}(t) - a'_1 h^{ln}(t - t_1, \mathbf{x}_1). \tag{4.18}$$

We apply the above procedure to the residual waveform to determine the optimum values of a'_2, t_2, and $\mathbf{x}_2$, then whole procedure is iterated until the residual sufficiently decrease. After N_{itr} iteration steps, the resultant synthetic waveform and the final approximation error are obtained by

$$y^{ln}(t) = \sum_{i=1}^{N_{itr}} a'_i h^{ln}(t - t_i, \mathbf{x}_i), \tag{4.19}$$

$$\Delta_{N_{itr}} = r_{vv}(0) - \sum_{i=1}^{N_{itr}} [a'^2_i r_{hh}(0, \mathbf{x}_i)]. \tag{4.20}$$

The variance reduction (VR) is given by

$$VR = 1 - \Delta_{N_{itr}}/r_{vv}(0). \tag{4.21}$$

We determine the optimum iteration number based on Akaike's information criterion (AIC) [Akaike, 1973]. The AIC at N_{itr} step is given by

$$\begin{aligned} \mathrm{AIC}_{N_{itr}} &= -2 \ln L_{N_{itr}} + 2k \\ &\cong \Delta_{N_{itr}}/\sigma_d^2 + 2k, \end{aligned} \tag{4.22}$$

where $L_{N_{itr}}$ is the maximum likelihood, σ_d^2 is the data variance and k is the number of free parameters. σ_d^2 is based on the back ground noise level of the seismograms at each station. From equation (4.14), the expansion coefficient a'_i is uniquely determined if t_i and $\mathbf{x}_i$ are fixed, therefore the number of free parameters for one iteration is 3 (origin time and two-dimensional source locations on the fault). Hence, $k = 3 \times N_{itr}$. The optimum N_{itr} is determined by minimizing this $\mathrm{AIC}_{N_{itr}}$.

Constraint based on Bayesian statistics

In general, the reliability of the solution for each step decreases with iteration number. The sources derived at later iterations are less reliable and likely to be affected by back ground distribution (which will be discussed in Chapter 4.4). To reduce such location failures, we introduce the constraint based on Bayesian statistics. In the above procedure, the likelihood function at i-th step is given by

$$P_d(\mathbf{x}_i, t_i) = \frac{1}{\left(\sqrt{2\pi}\sigma_d\right)^{N_d}} e^{-\frac{\Delta_i}{2\sigma_d^2}} \tag{4.23}$$

where N_d is a number of data. Minimizing Δ_i is equivalent to maximize $P_d(\mathbf{x}_i, t_i)$ in equation (4.23). If the space-time distribution of tremor sources is known a priori, the prior distribution is given by

$$P_p(\mathbf{x}_i, t_i) \propto \sum_{j=1}^{n_p} e^{-\left(\frac{\left|\mathbf{x}_i - \mathbf{x}_j^p\right|^2}{2\sigma_x^2} + \frac{\left|t_i - t_j^p\right|^2}{2\sigma_t^2}\right)}, \tag{4.24}$$

where $\mathbf{x}_j^p$, t_j^p are the location and origin time of j-th a priori source; n_p is a number of sources; σ_x and σ_t are hyperparameters which constrain the spatial and temporal expansions from the source, respectively. Then $\sigma_x/\sigma_t(= v_r)$ is interpreted as a rupture velocity.

The posterior probability function is given by the product of P_d and P_p,

$$L_i = P_d(\mathbf{x}_i, t_i) \cdot P_p(\mathbf{x}_i, t_i). \tag{4.25}$$

The maximum-a-posteriori estimate of t_i, and $\mathbf{x}_i$ are obtained as optimum values by maximizing L_i. After N_{itr} iteration, the AIC is given by replacing $L_{N_{itr}}$ in equation (4.22) to $L_{N_{itr}}$ as follows

$$L_{N_{itr}} = P_d\left(\mathbf{x}_{N_{itr}}, t_{N_{itr}}\right) \cdot P_p\left(\mathbf{x}_{N_{itr}}, t_{N_{itr}}\right). \tag{4.26}$$

4.3 Slip behavior of the tremor in western Japan

4.3.1 Study area and waveform data

We use two horizontal components of velocity seismograms recorded by Hi-net stations maintained by NIED. Each seismogram is band-pass filtered between 2-8 Hz, and resampled to 20 samples per second.
We focus two regions in the Shikoku (Fig. 4.2). One is the western Shikoku region which is the same as examined in Chapter 3. 38,715 events are detected during 4 years from 2005 to 2008 by matched filter analysis using the synthetic template waveforms. 9 stations (blue and red) are used, which are the same as ones in Chapter 3. Because the slip inversion requires heavy computational costs, we analyze just one tremor burst episode on March 2008 (Fig. 3.9b). Hence, our analysis covers the time period between 16 and 27 March 2008. This tremor burst episode in the target region was a part of sequential tremor migration from Bungo Channel to the eastern Shikoku in March and April 2008 (Fig. 4.3). The entire tremor episode started on 8 March at deep portion beneath Bungo Channel. The tremors migrated up-dip at first and secondly migrated along the strike of the subducting plate towards eastern. The associated slow slip event has been observed between 14 and 18 March 2008 [Sekine et al., 2010].
The other region is the central Shikoku region. The activity of the tremor in this region is not as high as that in the western Shikoku, but sometimes tremors are coincident with VLFs [Ito et al., 2007; Ito et al., 2009]. 6 stations (red and green) are used for the analysis (Fig. 4.2). We examine one-day records on 23 October, 2009 when a specific VLF (named VLF0 in this thesis) was previously detected [Ito et al., 2009].

4.3.2 Western Shikoku

Fault model and Parameter settings for inversion

The fault model in the western Shikoku is the same as that used in Chapter 3 (Fig. 3.2). We assign 4,425 nodes with interval of 250m on the fault and calculate each horizontal component of the synthetic template waveforms at every station for every node. Because the amplitudes of P-waves of the LFEs in the region are negligible compared with those of S-waves at almost all

stations, we use only S-waves of the synthetic templates for the analysis. The time window used for each template waveform is 4.0 s starting from 1.5 s before the theoretical arrival times of S-waves. The source duration for the synthetic template, the duration of $f(t)$ in equation (4.2), is assumed to be 0.3 s which is derived for moment tensor inversion in Chapter 3.5. The temporal basis time function, $s(t)$, is also assumed to be a linear spline function whose duration is 0.3 s.

We use the distribution of tremor sources detected by matched filter analysis using synthetic template waveforms as a prior distribution for iterative searching process. The number of detected events in the burst episode is 2,205 (Fig 3.9b). The hyperparameters, σ_x, σ_t, in equation (4.24) are set at 1 km and 100 s, respectively. At these values the rupture velocity, σ_x/σ_t, is equal to 36 km/h which is comparable to the short-term migration velocity of LFEs in the region. All parameters for the slip inversion are summarized in Table 4.1.

To reduce the computational cost, we apply the slip inversion method to every 30 minutes time window of the continuous seismograms for 12 days from 16 to 27 on March, 2008. Thus 576 time windows are examined in total.

Variance and Comparison of data to synthetic

Figure 4.4 shows an example of the variance and AIC as function of N_{itr}. The time window is 23:30-24:00 on 16 March, 2008. $\Delta\mathrm{AIC}$ $(= \mathrm{AIC}_{N_{itr}} - \mathrm{AIC}_{N_1})$ is shown by a red curve instead of AIC in equation (4.22). The variance decreases rapidly in the beginning and gradually in the latter. While the variance monotonically decreases to the end of iteration steps, $\Delta\mathrm{AIC}$ has the minimum value at N_{itr} = 33,049. VR at this step is 79.8%.

Figure 4.5 shows an example of the comparison between observed and synthetic seismograms within the same time window. 100 s waveforms including the tremor within the same time window described above are shown here. The observed waveforms are well explained by the synthetic waveform.

From the result of the analysis for all 576 windows, the average optimum N_{itr} and VR are about 30,000 and 80% respectively.

Resultant slip evolution from inversion (entire image: 12 days)

We first show the entire image of the slip evolution of tremor for the whole

episode of 12 days. The daily snap-shots of the slip distribution for the episode are shown in Figure 4.6. Each panel shows the total slip distribution derived from the tremor waveforms for each day. Notice that color scales are different for each panel because of the significant difference in the daily slip amount. The slips seem to occur repeatedly on several patchy regions, northern two patches, a patch just south of center and a south eastern patch on the up-dip side. The slip amount is the highest in the first day and decreases to the end of the episode. The total slip amount per unit area on the fault for the entire period is 748.33 μm. While the slips occur on both deeper and shallower part of the fault in the beginning of the episode, the slips occur on only shallow part in the latter of the episode.

Figure 4.7 shows the moment rate function of tremor in the episode. The difference in moment release for each day is very clear. The total moment release is 5.7×10^{15} Nm, and ~70 % of the moment release is accounted by the tremor in the first three days. In addition, we can see two lineations of active periods in moment release plots, being shifted at a rate of of about 1 hour/day (blue lines), which implies that these active periods are controlled by the M2 tide.

Resultant slip evolution from inversion (detailed image: 30 minutes)

We next focus on the short episode at 23:30-24:00 on 16 March, 2008 which is the last 30 minutes of the first day. This period was investigated in Chapter 3.6 to demonstrate the migration of detected tremor sources.

The final slip distribution and snapshots of slip rate during the episode are shown in Figure 4.8. From the final slip distribution we can see three small regions with large moment releases (strong slip patches) in the central, west, and north of the fault. These patches correspond to the active clusters of LFEs. The slip evolves initially from the patch just south of the center (0-200 s), migrates to the west and north (200-1000 s), and finally strongly ruptures in the north patch (1000-1800 s). This evolution is also captured in the moment growth curve and the moment rate function (Figure 4.9). The moment growth is roughly divided into three stages. Rapid increase of moment for about 80 s occurred around 200 s from the beginning, followed by a gradual moment growth for several hundred seconds and the final rapid moment increase for about 60 s. The total cumulative moment is 1.7×10^{13} Nm.

4.3.3 Central Shikoku

Very low frequency earthquakes in the central Shikoku

We next focus on the tremor in the central Shikoku region (Figure 4.2). This region was selected for the comparison between tremor and coincidental VLFs. In this region several VLFs have been detected and analyzed by grid centroid moment tensor inversion [Ito et al., 2007; Ito et al., 2009]. We focus one tremor episode which contains VLF0 occurred at 00:34:12 on 23 October, 2006. Figure 4.10 shows the broadband seismograms at two F-net stations (OKW and UMJ) for 1 hour from 0:00 on 23 October, 2006. The signals of tremor (2-8Hz) and VLF (0.02-0.05Hz) are clearly visible at about 2000 s.

Fault model and Parameter settings for inversion

The fault model is provided by the precise distribution of previously observed LFEs as shown in Figure 4.11. 160 LFEs are accurately relocated by the NCC method in this area (Table 2.1). The fault plane is obtained by fitting a plane to the hypocenters using least squares where the errors are measured vertically. The obtained fault plane has a strike of N258.34°E and 7.54° dip and the center is located at 33.914°N, 133.335°E and at the depth of 31.26 km which coincides with the centroid of the 160 LFEs. The length and width of the fault model are both 20 km. We assign 6,561 nodes with interval of 250m on the fault as the origins of the synthetic template waveforms. Other parameters for slip inversion are the same as those used for the analysis of the tremor in the western Shikoku (Table 4.1).

Detection of VLFs similar to VLF0 using running autocorrelation

For the comparison between tremor and VLF, we search VLF events additionally which are similar to VLF0 using the running cross correlation. The data are vertical components of velocity seismograms recorded at three F-net stations (OKW, UMJ, and TGW) (Fig. 4.2). Each seismogram is band-pass filtered between 0.02-0.05 Hz, and resampled to 20 samples per second. We use the 100 s time windows which contain the S-wave of VLF0 as templates. We calculate the running cross correlation coefficients between the templates and the continuous seismograms for each station at every lag by 1 s. The average correlation coefficient across all channels is used for detection. The threshold is set at 0.7. We search 1 day seismograms on 23

October, 2006. Another four events (VLF1-4) are newly detected (Figure 4.12). We apply the slip inversion method to these 4 periods.

Resultant slip distribution from inversion

Figure 4.13 shows the slip distributions of the tremor coincident with VLF0 and newly detected four VLFs (VLF1-4). The moments of the tremor coincident with those VLFs are 3.80×10^{12} Nm, 3.17×10^{12} Nm, 3.20×10^{12} Nm, 2.81×10^{12} Nm, and 3.55×10^{12} Nm, respectively. The green star denote the centroid of VLF0 estimated by Ito et al. [2009] and the blue circles denote the centroids of the tremor estimated by the slip inversion in each period. Taking into account that the estimation error of the centroid of VLF is several km [Ito et al., 2009], the centroids of both tremor and VLF are almost identical as discussed in the previous studies [e.g., Maeda and Obara, 2009; Takeo et al., 2010].

While the seismograms of VLF are very similar, the slip distributions of tremors are not necessarily similar to each other. The tremors coincident with VLF0 are distributed in both the west and east of the centroid. On the other hands the newly detected tremors seems to be distributed in the southeast of the centroid.

4.4 Discussion

Background noises

Before detailed discussion, we comment on the effect of background noises. Because it is difficult to define the initiation and termination of tremor from the continuous seismogram, we analyze all waveforms which contain both the signals of tremor and background noises. Compared to the ordinary earthquakes, the signal-to-noise ratio of tremor is relatively low even in the dominant frequency range of tremor. Therefore, the contribution of noises to the inversion results might not be negligible in some cases. To evaluate the effect of back ground noises, we applied the method to the seismograms which contain no tremor signals and no obvious other earthquakes.

Red curves in Figure 4.9 show the seismic moment from back ground noises. The time window one week before the tremor burst episode in the western Shikoku region is selected as back ground. The cumulative moment growth from noises is proportional to t, along $\mathrm{M}_0(t) = 0.7 \times 10^{10} t$. Hence, we should take notice that the estimated seismic moment of tremor is overestimated at this rate due to background noises.

Figure 4.14 shows the slip distribution derived from these back ground noises. The slips on the west side of the fault are slightly large. This might be partly because the synthetic template waveforms at these portions are rather monotonic, hence easier to correlate with back ground noises (Fig. 4.15). We should keep in mind that the resultant slip distribution is affected by this pattern of spatial distribution.

Overestimation of iteration steps

Next we consider the effect of iteration procedure. As described in Chapter 4.2, the optimum iteration number is determined on the basis of AIC in equation (4.22). However, this AIC is not the true AIC because the order of iteration affects solutions. In other words, the iterative deconvolution method cannot provide the globally optimized solution. However, due to a large number of model parameters, it is unrealistic to adopt linear inversion methods or nonlinear inversion methods like monte-carlo methods because they require huge memories or enormous computational time. Therefore, the optimum solution obtained in this study is not the best solution but a compromised solution in capacity of current computational resources. As a

consequence of this issue, AIC defined in equation (4.22) should be larger than the true AIC, which leads to overestimation of the iteration number.

Effect of Bayesian constraint

We also discuss the effect of the prior information applied in our Bayesian modeling. The resultant slip distribution is constrained around the distribution shown in equation (4.24). This constraint could fairly control the resultant distribution.

We compare the slip distributions for three different levels of constraints by changing hyperparameters, σ_x and σ_t, in equation (4.24) (Fig. 4.16). The sets of hyperparameters, (σ_x, σ_t), in the cases of the weak constraint (adopted in this study) and the strong constraint are $(1\,km,\ 100\,s)$ and $(100\,m,\ 10\,s)$, respectively. In both cases, the rupture velocity, σ_x/σ_t, is retained to the same value. In the case of no constraint, the distribution seems to be rather sparse and slips on the west side of the fault are prominent. However, this might be caused by the back ground effects described above (Fig. 4.14). On the other hands, in the case of strong constraint the distribution is thoroughly bound to the prior distribution.

It is difficult to determine the optimum values of hyperparameters for the reason that the criterions such as ABIC are not applicable with realistic computational costs. In this study, the hyperparameters are set as the dominant slip areas are comparable to the clusters of tremor sources detected by the matched filter analysis. Since our method is the straight extension of the matched filter techniques, this assumption is not the optimum but reasonable.

Slip evolution of tremor during the burst episode in the western Shikoku

We now discuss the entire picture of the slip evolution during the burst episode in the western Shikoku region (Fig. 4.6, Fig. 4.7). The temporal and spatial changes of tremor slips should be highly relevant with the slow slip in the same region. The tremor slips are dominant in the early stage of the episode and the seismic moments of tremor released especially in the first three days account for most of total seismic moments of tremor in the episode (Fig. 4.7). This might be closely related to the SSE coincident with the tremors.

As shown in Figure 4.3, the migrating tremor sequence started from Bungo Channel before the burst episode analyzed in this study. Such tremor migration has been interpreted to represent the propagation of rupture front of slow slip [Obara, 2010]. The active period of the associated slip has been constrained by Sekine et al. [2010] using tilt meter data. The estimated SSE on March, 2008 started from 2008/03/14 and ended on 2008/03/18. The estimated fault geometry of the SSE is also shown in Figure 4.3. In the entire episode, the early stage of focused burst episode can be interpreted as the timing when the rupture front of this SSE passed though the target region.

Figure 4.6 shows that the slips derived from tremor tend to occur at both shallower and deeper part of the fault in the early stage, whereas the slips occur at only shallower part in the latter. The region of slow earthquakes may consist of a mixture of brittle and ductile regions and the ratio of brittle to ductile areas should be inversely proportional to the depth. Therefore, the SSE should be easy to grow at the deeper ductile part of the fault and trigger the tremors on brittle patches at the deeper part. Then the arising question is, what drives the tremors at the shallower part of the fault in the latter half of the episode? As shown in Figure 4.7, the tremor activity seems to correlate with the tidal stress perturbation as reported by many studies [e.g. Nakata et al., 2008; Rubinstein et al., 2008]. That correlation is rather clear in the latter half of the episode. This indicates that the tidal controls are dominant on triggering of tremor at the shallow part in the latter half of the episode. One possible explanation is that SSEs trigger deeper tremors relatively easily and release most of the strain at the portion, whereas the tremors at the shallower strong portion are less triggered by SSEs and the strain remains around tremor sources after the major slip of SSEs. In that case, the shallower tremor might occur with help of tidal stress and release the rest of

strain.

Slip behavior of tremor and heterogeneities on the fault

We next focus on the detailed picture of the slip evolution during 30 minutes sequence in the western Shikoku region (Fig. 4.8, Fig. 4.9). Resultant spatial and temporal slip behavior is quite heterogeneous. As demonstrated by Nakata et al. [2011], the variation of the shape of moment rate functions shown in Figure 4.9 could be explained by differences in brittle patch density and/or viscosities. In general, high density of brittle patch and low viscosity on both patch and back ground region produce a large pulse-like moment rate function while low density and high viscosity produce moderate long-lasting moment rate function. Then two prominent slip patches shown in Figure 4.8 could be characterized by dense brittle patches and/or locally low viscosity areas. The changes in the slope of cumulative moment curve shown in Figure 4.9 may indicate the gradual change of these properties between these two patches, though slip distribution in such area is not well constrained. There is a possibility that larger scale slow earthquakes with durations of over several hundred seconds are excited in such area. However, we cannot confirm the existence of such events due to the observational limits of seismology [Ide et al., 2008].

We now return to two rapid slips on the south and north of the fault. The duration of those slips are about 60-80 s. From the scaling relation of slow earthquakes [Ide et al., 2007], the moment release with such duration suggests the existence of VLF events. However, no VLFs corresponding to this time period have been reported. We checked the broadband seismograms at three F-net stations (OKW, TGW, and TSA) around the fault (Fig. 4.17). While tremor signals are very clear in the frequency band of 2-8 Hz, we cannot see the obvious signals of VLFs in the very low frequency band of 0.02-0.05 Hz. In fact, no VLFs have been observed in the western Shikoku area, whereas many VLFs have been detected beneath Bungo Channel, central and eastern Shikoku region [Ito et al., 2009]. Two possibilities can be considered. The one is that VLFs always accompany tremor but VLF signals are apparently obscured due to noises in the very lower frequency band. The other is that no VLF events are excited in this region. To make sure which idea is reasonable, further studies are necessary.

Tremor associated with VLF in the central Shikoku

We further discuss the tremor and VLF in the central Shikoku region. The seismic moments estimated from the tremor associated VLFs (VLF0-4) are $2.8 - 3.8 \times 10^{12}\ Nm$, which are fairly smaller than that of VLF0 derived from broadband data, $1.2 \times 10^{14}\ Nm$ [Ito et al., 2009]. This is because our analysis only uses seismograms within narrow frequency band higher than the characteristic frequency of VLF. Since we can see only microscopic source process of slow earthquakes in this frequency band, the evaluation of total moment releases in the transition zone accounted for by slow earthquakes is out of focus at this stage. Hence we now focus on the spatial distribution of slips derived from tremor. Figure 4.18 shows the centroids of 25 tremor sequences with durations over 100 s which occurred in the same day as the occurrence of VLF0. Among 25 sequences, only 5 sequences (VLF0-4) have VLF signals as stated in Chapter 4.3 and the centroids derived from those 5 sequences are presented by blue circles. The centroids of tremor slips associated with VLFs tend to be located south of fault area. This suggests that the source area of VLF exists at southern portion of the fault.

Figure 4.19 shows the total slip distribution derived for those 5 tremor sequences. The distribution illuminates the source area of VLF. The dense slip patches exist across the sparse area. Low frequency radiation of VLF could be excited by the cascades of slips on the patches. The apparent source size of VLF is approximately estimated to be ~ 5 km in radius. Assuming a circular crack model with a constant stress drop, $M_0 \sim \Delta\sigma L^3$, where $\Delta\sigma$ and L are stress drop and source radius, respectively. Substituting $M_0 = 1.2 \times 10^{14}\ Nm$ and $L \sim 5\ km$, then a stress drop $\Delta\sigma$ for VLF is estimated to be ~1.0 kPa, which is comparable to the stress perturbation of tide [Rubinstein et al., 2008; Nakata et al., 2008] or passing surface waves [e.g. Miyazawa and Mori, 2006; Rubinstein et al., 2007; Peng and Chao, 2008]. Although the assumption of constant stress drop might be unsuitable, it is useful to constrain the source area directly from the observation.

Comparison of tremor between the western and central Shikoku

We finally compare tremor activities between the western and central Shikoku regions. The obvious difference between two regions is shown in synchronicity of tremor and VLF. As stated before, VLFs and coincidental

tremor are sometimes observed in the central Shikoku region, though no such VLFs have been observed in the western Shikoku region. Then, outstanding question is why there are no VLFs in the western Shikoku? Let us consider the cause of the difference from slip inversion result of tremor in both regions.

Figure 4.20 shows the comparison of moment growth and slip distribution of tremor between the western and central Shikoku. Two rapid tremor slips in the western Shikoku as stated before and tremor slips associated with VLF0-4 in the central Shikoku are compared. From Figure 4.20a, we cannot see significant differences in moment growth. All cumulative moment growth curves are approximately along $\mathrm{M}_0(t) = 2.8 - 3.8 \times 10^{10}\, t$. The shapes of moment rate functions are also comparable (Fig 4.20b).

From Figure 4.20c, we can see the difference in dominant slip areas of these slips. The source sizes of tremor in the western Shikoku seem to be much smaller than that in the central Shikoku. This could be the reason for the absence of VLFs in the western Shikoku. The small size source areas in the western Shikoku might prevent the excitation of low frequency seismic wave radiation comparable to VLFs in the central Shikoku. The difference in physical properties could be possibly explained in the heterogeneous model [Ando et al., 2010; Nakata et al., 2011]. In the model, the dense brittle patches and high viscous back ground (western Shikoku?) produce similar moment rate function to that in the case of the sparse brittle patches and low viscous back ground (central Shikoku?). Although this interpretation is too simple because we do not consider other frictional properties, the varieties in occurrences of VLFs might be characterized by such differences as one possibility.

Figures

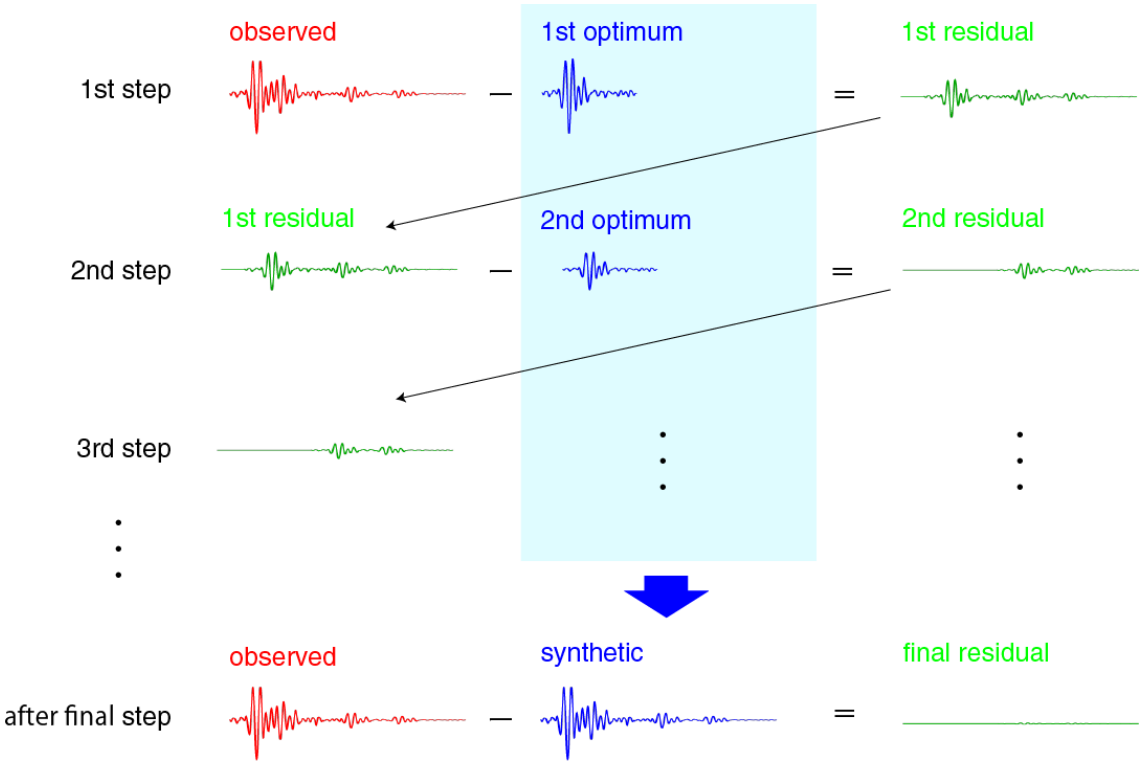

Figure 4.1: A schematic diagram to illustrate the procedure of iterative deconvolution. At each step, a residual waveform is calculated by subtracting the waveform of an optimum event from the residual waveform at the previous step.

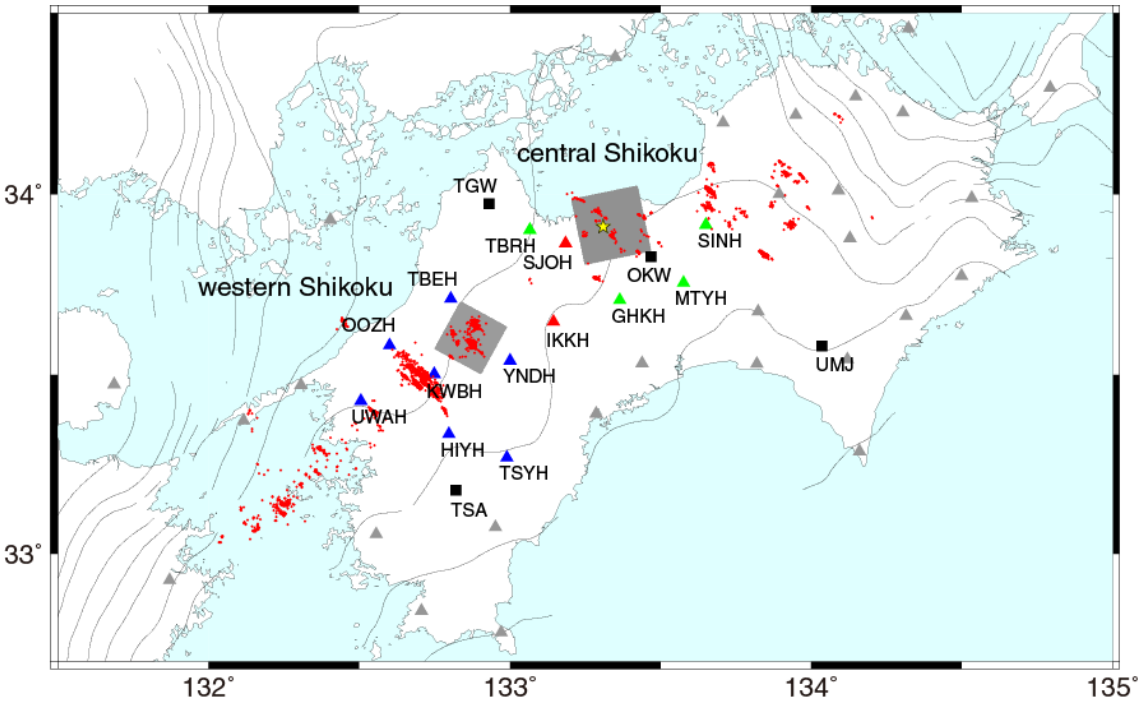

Figure 4.2: Map of the study area. Red dots are the epicenters of LFEs determined by NCC method in Chapter 2. Yellow star shows the centroid of VLF which occur on 23 October, 2006 estimated by Ito et al. [2009]. Two gray squares in the western and central Shikoku show the assumed fault geometries. Triangles are the location of Hi-net stations. The blue and red are used for the analysis in the western Shikoku, and the red and green are for the central Shikoku. Black squares show F-net stations. Gray contour lines indicate the depth of the oceanic Moho estimated by the receiver function analysis [Shiomi et al., 2008].

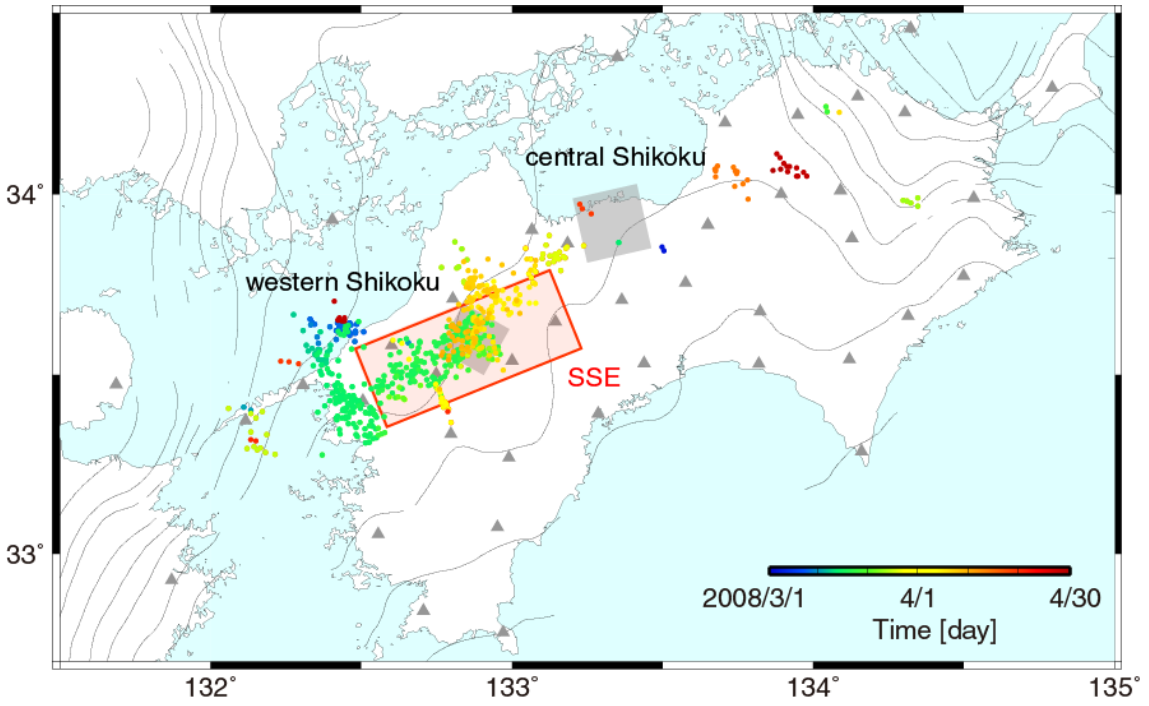

Figure 4.3: Migration of the tremors in March and April, 2008 in Shikoku. The epicentral locations of the tremors are shown in different colors (catalog from Idehara et al. [2014, submitted]). The color scale indicates time. Red rectangle presents the fault geometry of the short-term SSE during 14-18 on March, 2008 estimated by Sekine et al. [2010]. Two gray squares in the western and central Shikoku show the fault geometries used in this study. Triangles are the location of Hi-net stations. Gray contour lines indicate the depth of the oceanic Moho estimated by the receiver function analysis [Shiomi *et al.*, 2008].

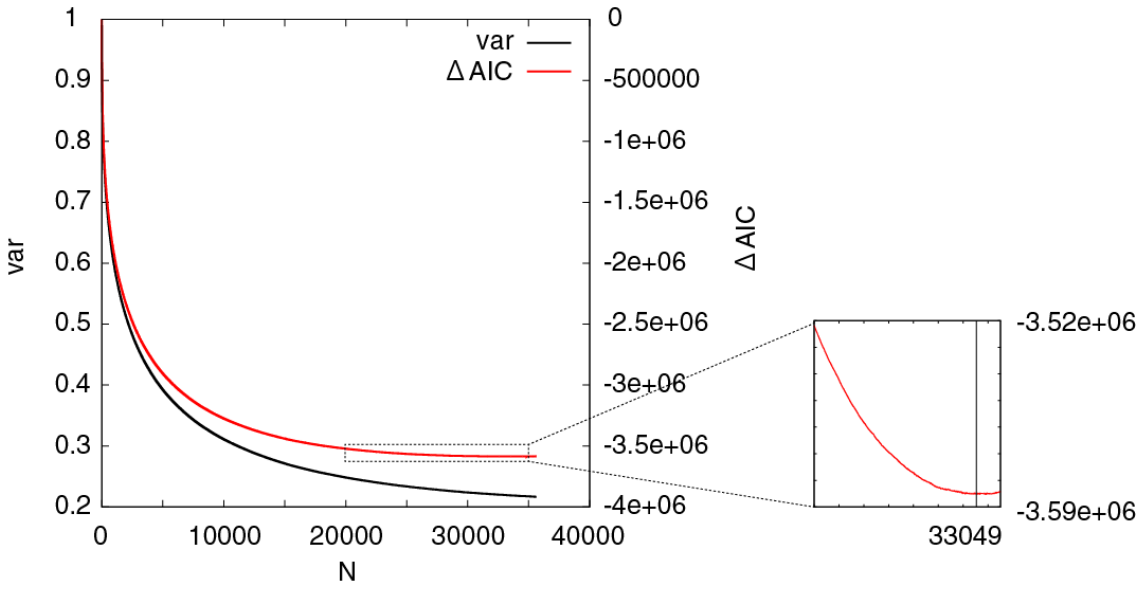

Figure 4.4: The inversion result for the tremor during 23:00-24:00 on 16 March, 2008 (JST). Red curve shows variance and black curve shows ΔAIC ($= AIC_0 - AIC_N$). Right panel is a close-up around the minimum value of ΔAIC.

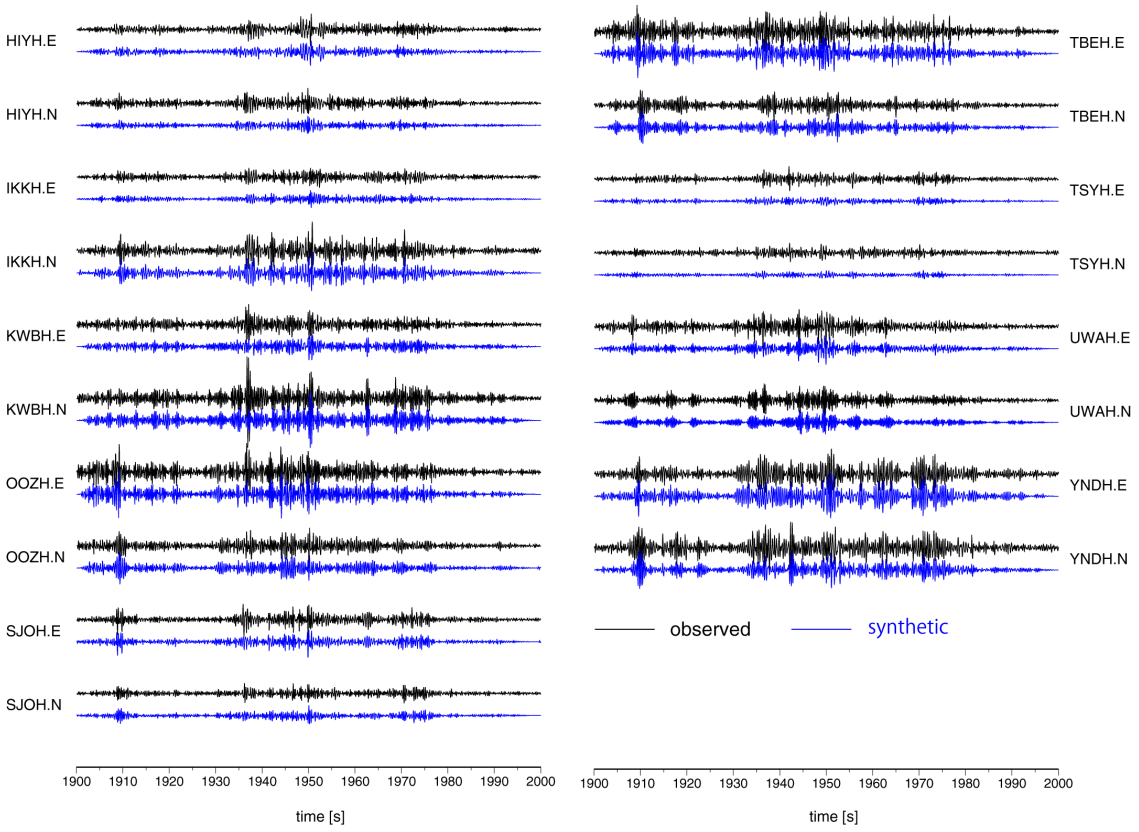

Figure 4.5: Comparison between observed (black lines) and synthetic (blue lines). Example for 100 s windows from 23:30:10 on 16 March, 2008 (JST) is shown.

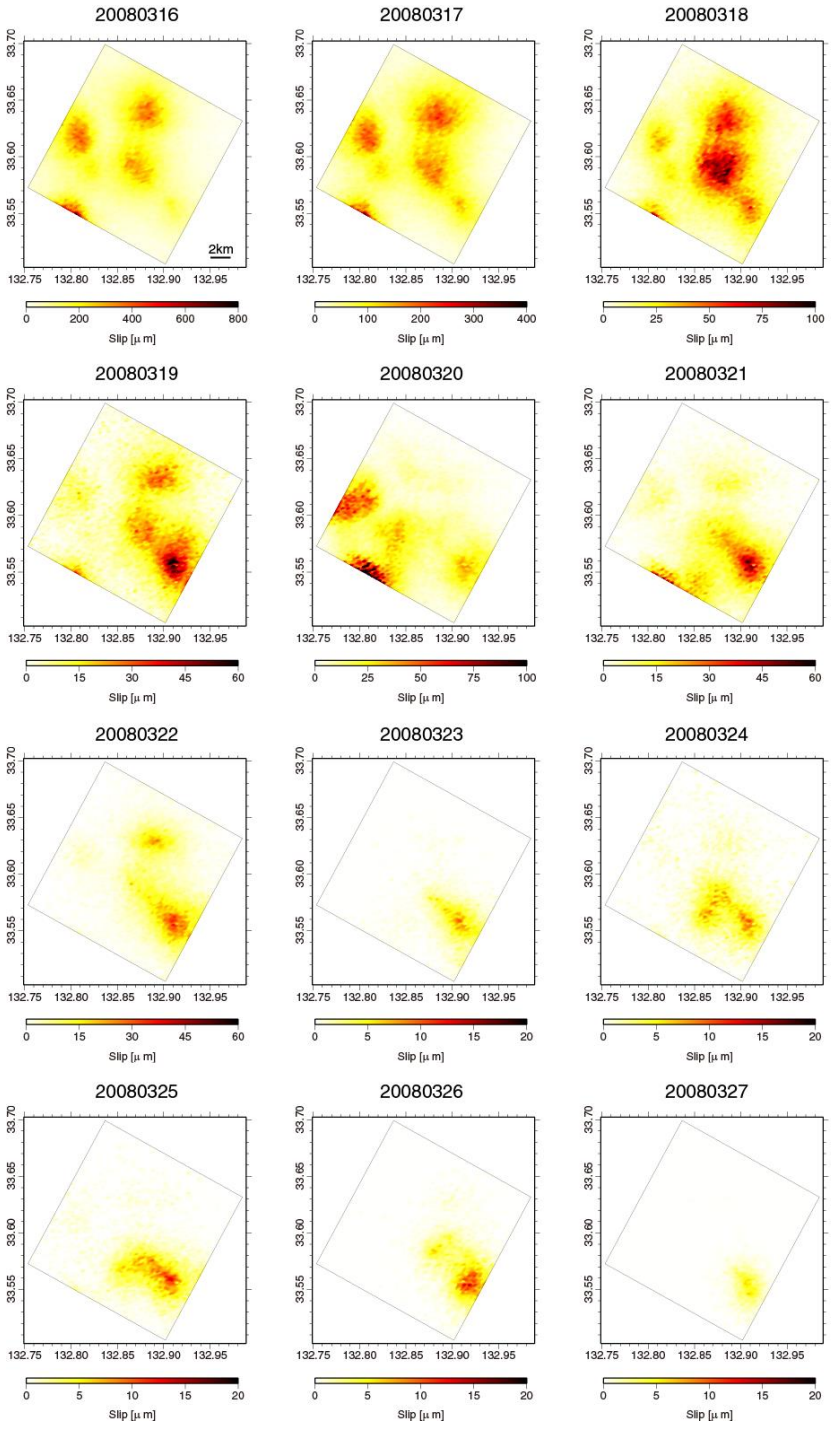

Figure 4.6: Slip distributions of tremor in the western Shikoku for each day of the focused episode obtained by slip inversion. Gray rectangles show the assumed fault plane.

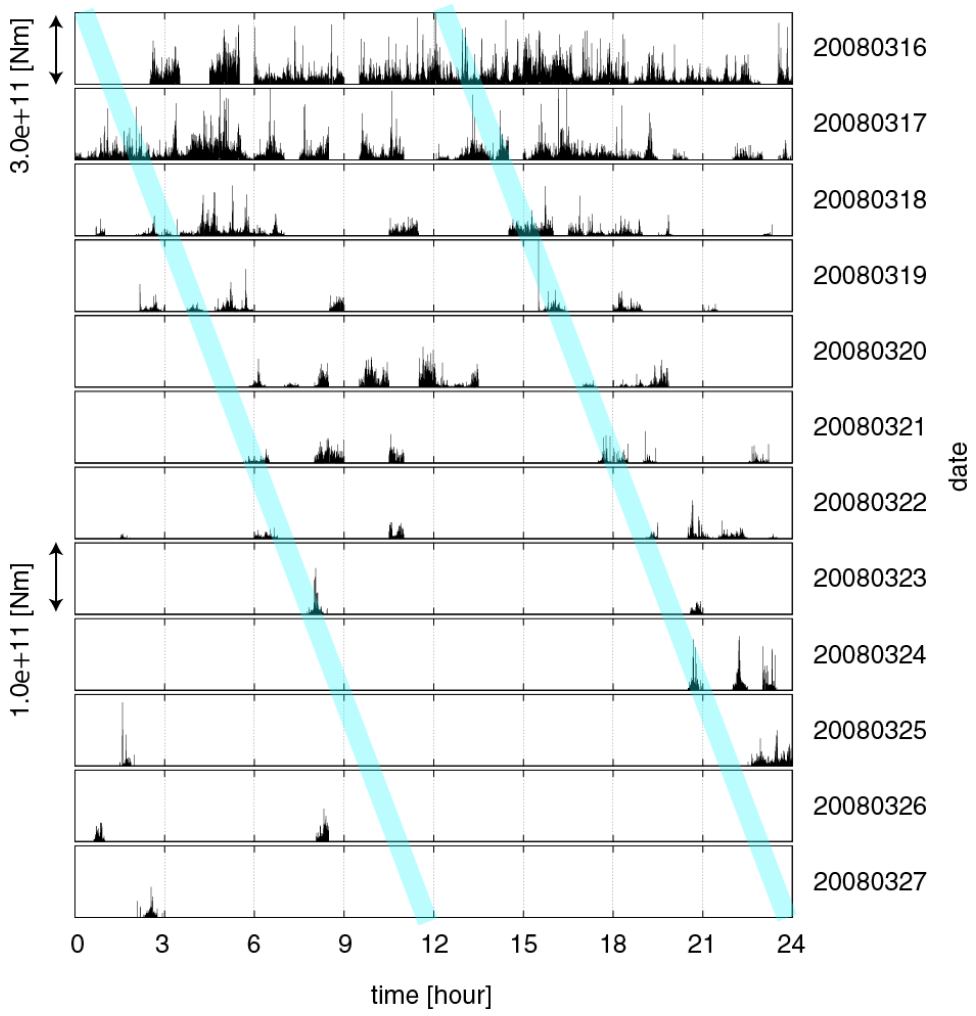

Figure 4.7: Estimated moment rate functions. Note the scale of moment rate is different between the former 7 days and latter 5 days. Two thin blue lines indicate M2 tidal constituents.

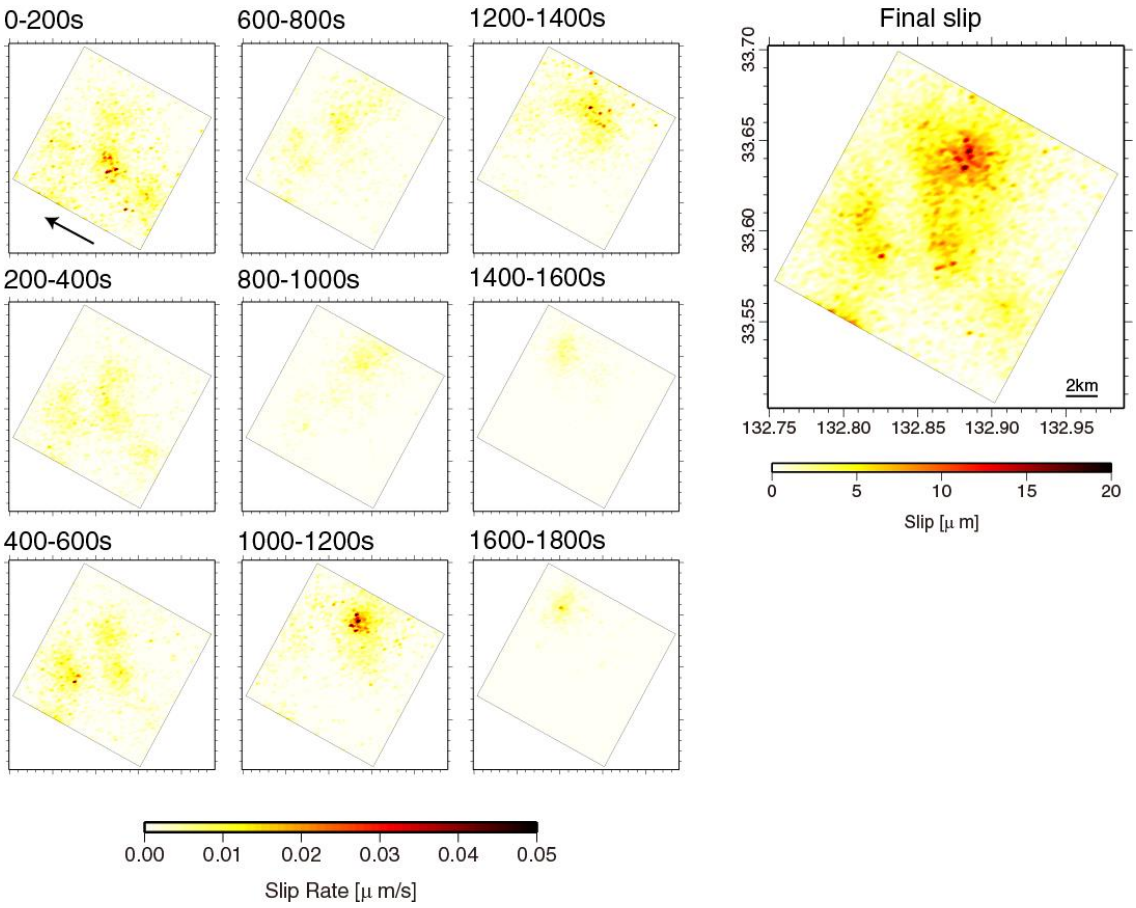

Figure 4.8: Slip rate history and final slip for tremor in the western Shikoku within 30 min from 23:30:00 on 16 March, 2008 (JST).

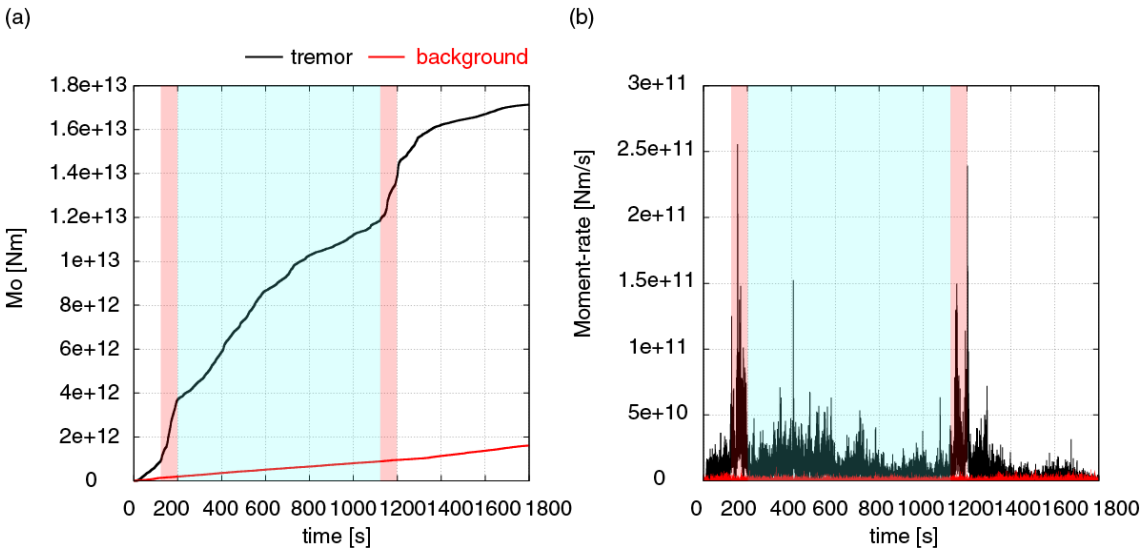

Figure 4.9: Cumulative moment functions (a) and moment rate functions (b) for tremor in the western Shikoku within 30 min from 23:30:00 on 16 March, 2008 (JST). Black lines show moment (moment-rate) estimated from tremor and red lines show moment (moment-rate) estimated from back ground noises.

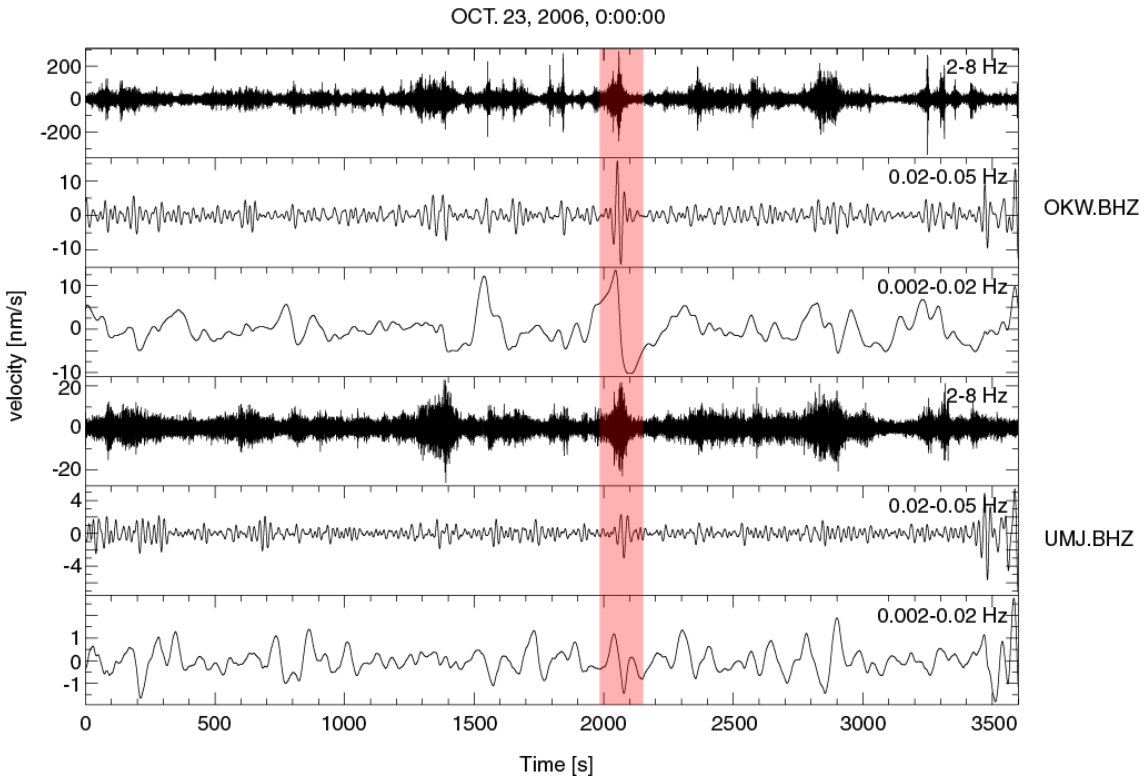

Figure 4.10: The broadband velocity seismograms at station OKW and BHZ. Time windows for 1 hour from 00:00:00 on 23 October, 2006 (JST) are shown here. Waveforms are shown in three different frequency ranges. They are band-pass filtered between 2-8, 0.02-0.05, and 0.002-0.02 Hz, respectively.

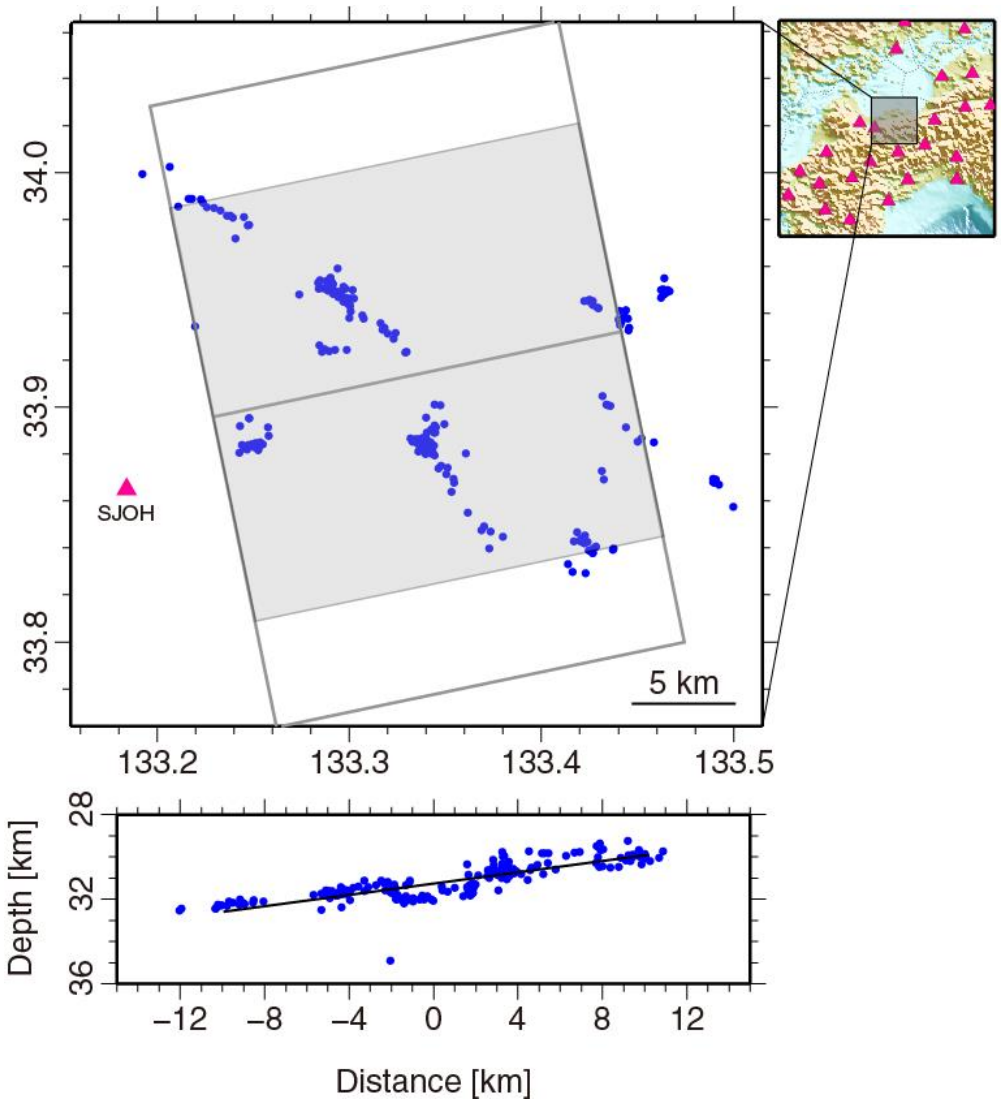

Figure 4.11: The assumed fault plane in the central Shikoku region is shown by a grey shadow rectangle (upper panel) and gray line (lower panel). Blue circles show the hypocenter locations of LFEs which are relocated by NCC method in Chapter 2.

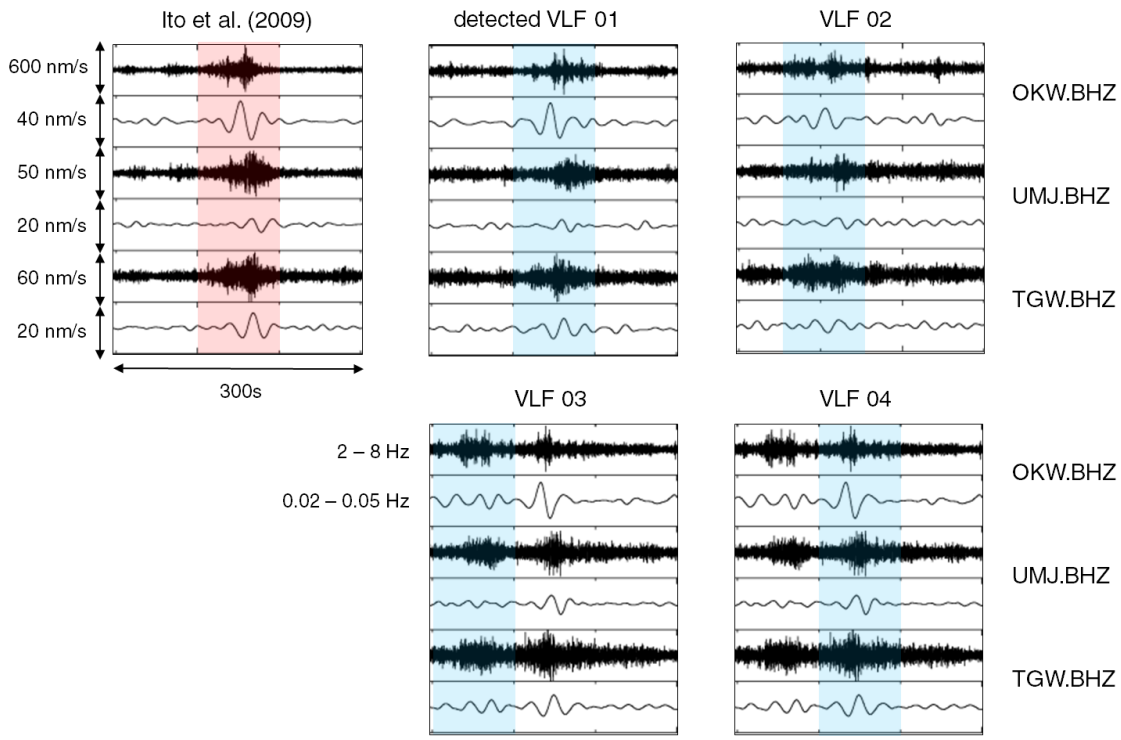

Figure 4.12: The waveforms of VLF0 and four detected VLFs (VLF1-4).

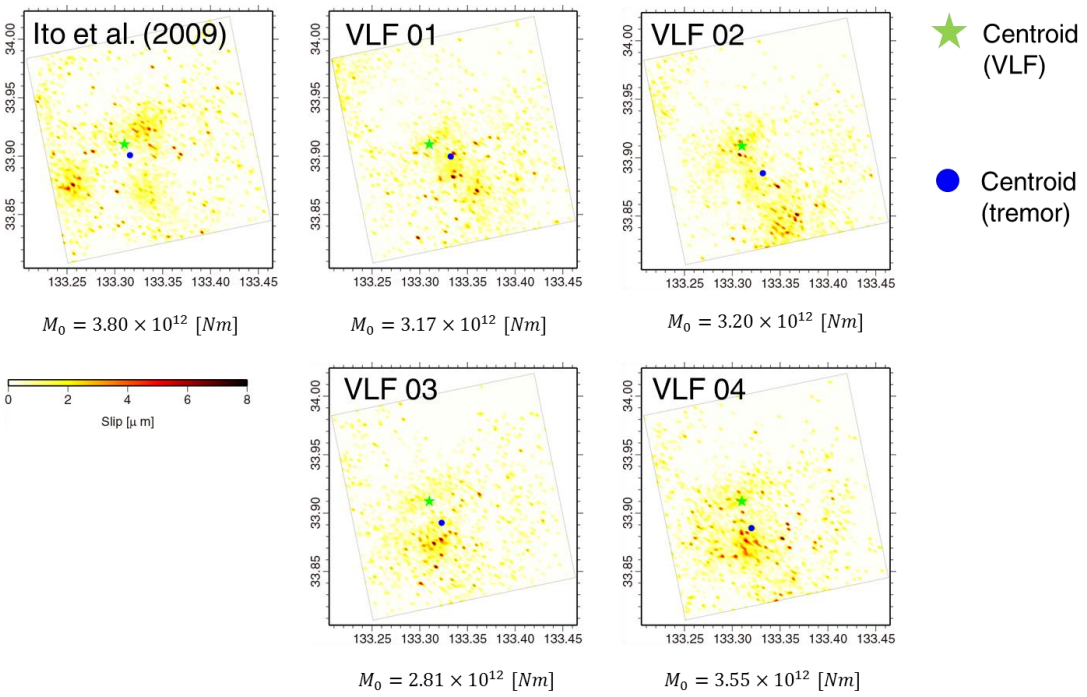

Figure 4.13: Slip distributions of tremor coincident with VLFs. Green stars denote the centroid of VLF0 estimated by Ito et al. [2009]. Blue stars denote the centroids of the slip distribution of each tremor.

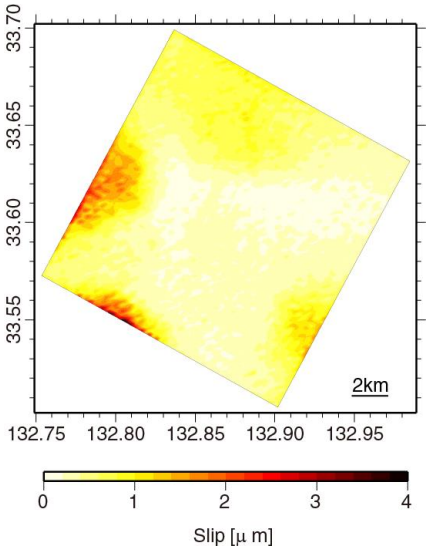

Figure 4.14: Slip distribution derived from back ground noises. Time period analyzed is 30 minutes from 23:30:00 on 09 March, 2008 (JST), which is just 1 week before the time period shown in Figure 4.8.

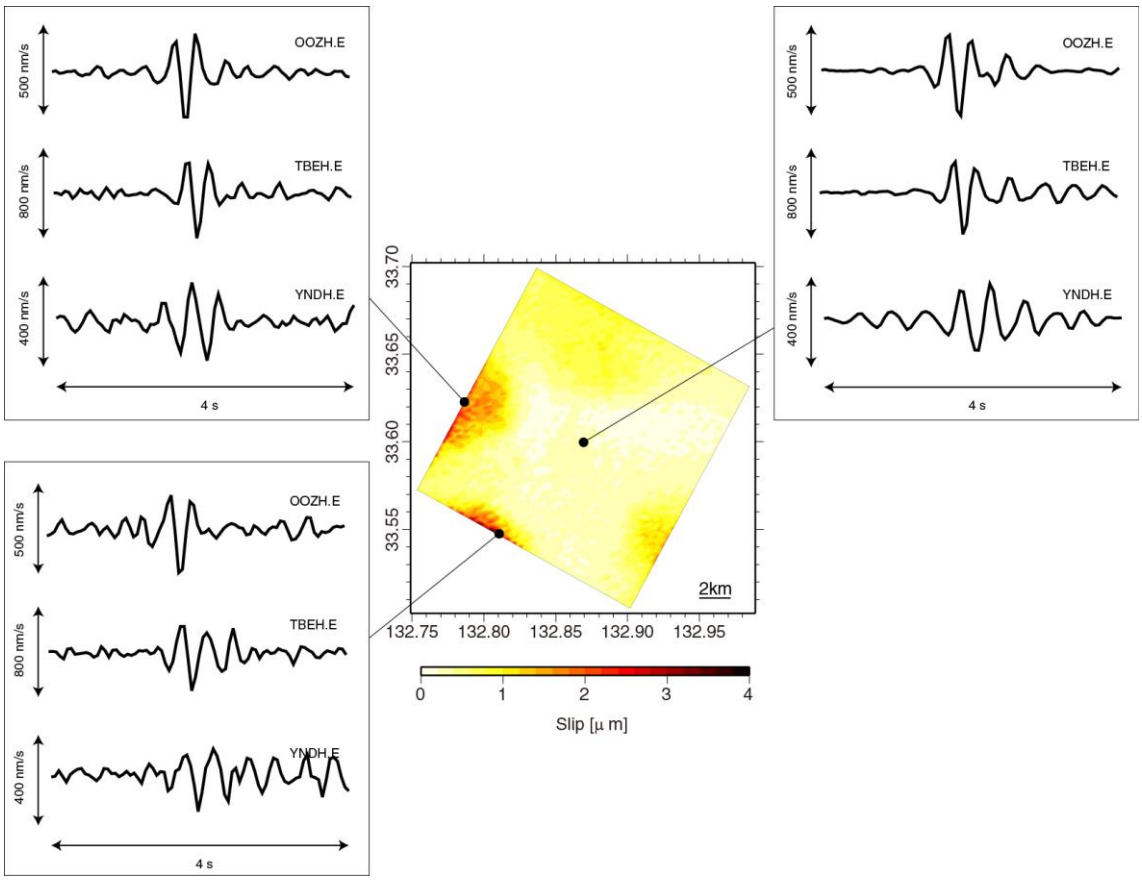

Figure 4.15: Examples of the synthetic template waveforms from different portions on the fault in the western Shikoku. EW components of the synthetic template waveforms at three Hi-net stations (OOZH, TBEH and YNDH) are shown. The slip distribution is the same as Figure 4.14.

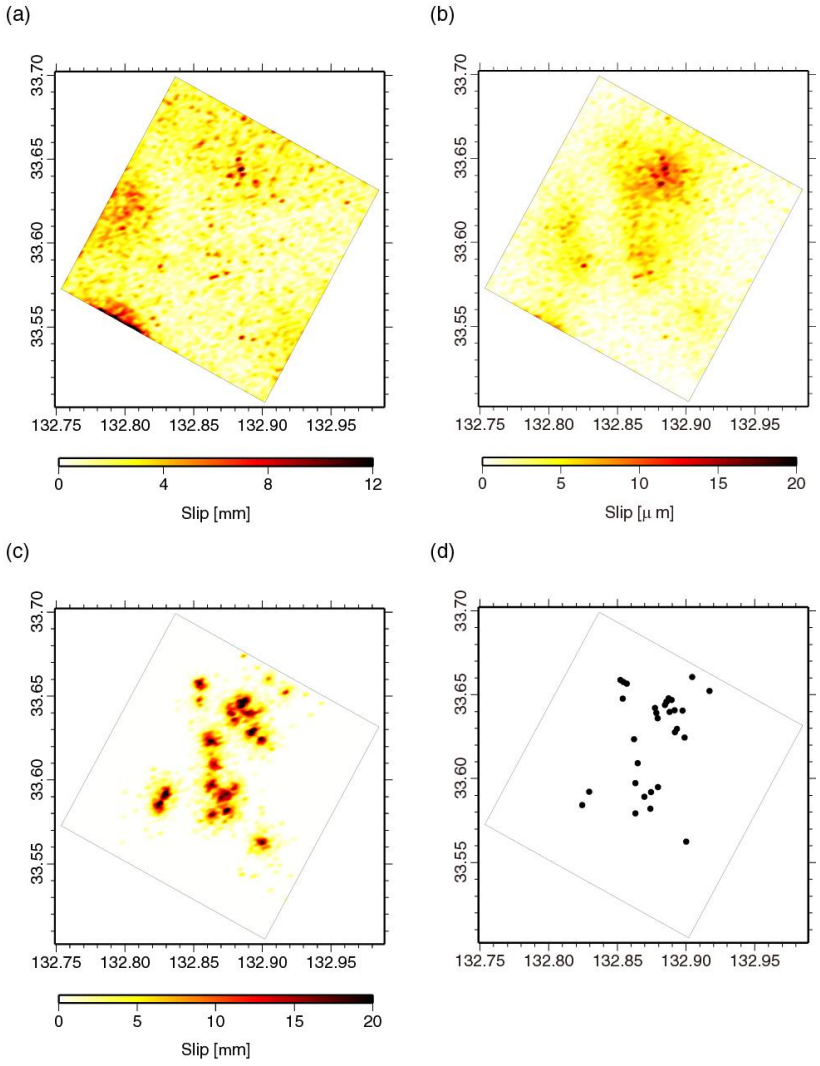

Figure 4.16: Comparison between the slip distributions for different levels of constraints. (a) no constraint. (b) weak constraint which is adopted in the study. (c) strong constraint. (d) prior distribution of tremor sources.

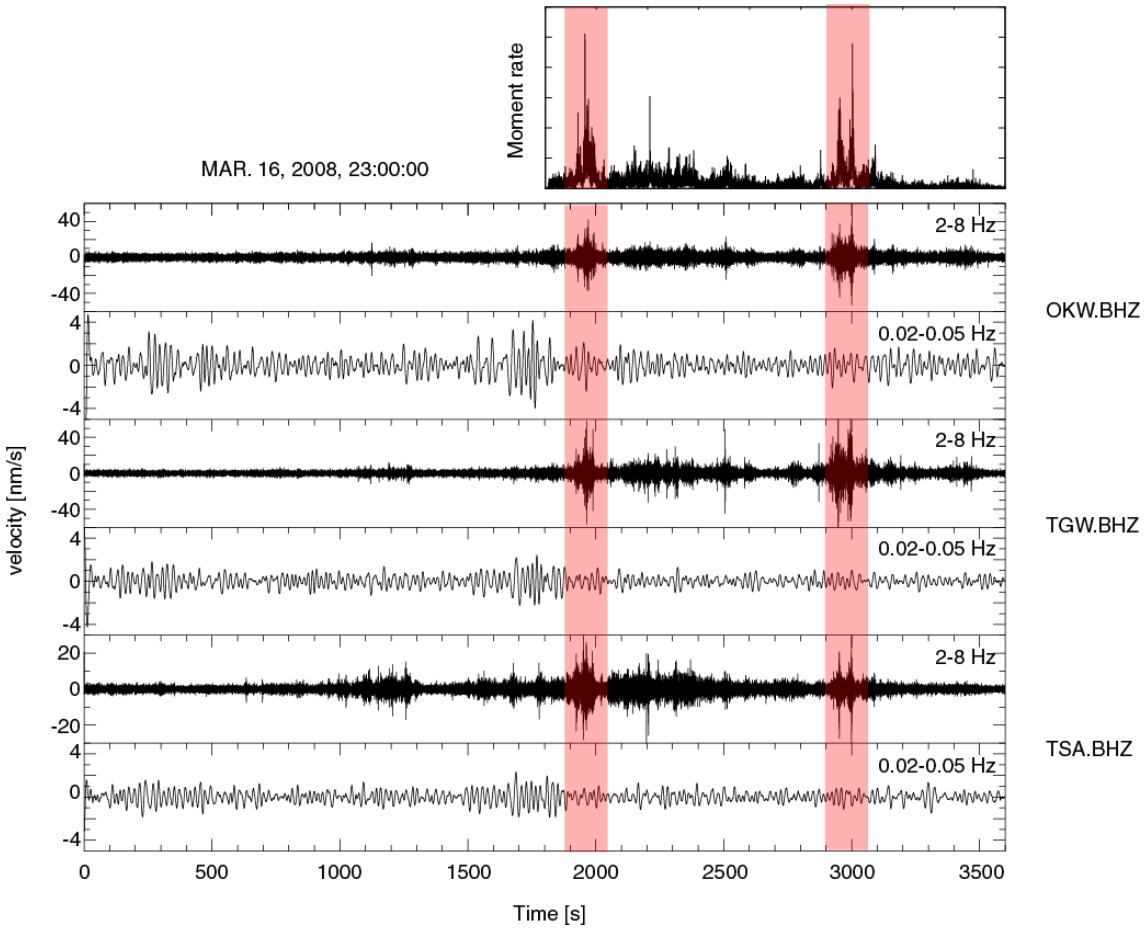

Figure 4.17: Broadband seismograms observed at three F-net stations. Time windows for 1 hour from 23:00:00 on 16 March, 2008 (JST) are shown here. Estimated moment rate function of tremor for the corresponding time window is shown in upper. Red shadows indicate the time period of rapid moment increases of tremor.

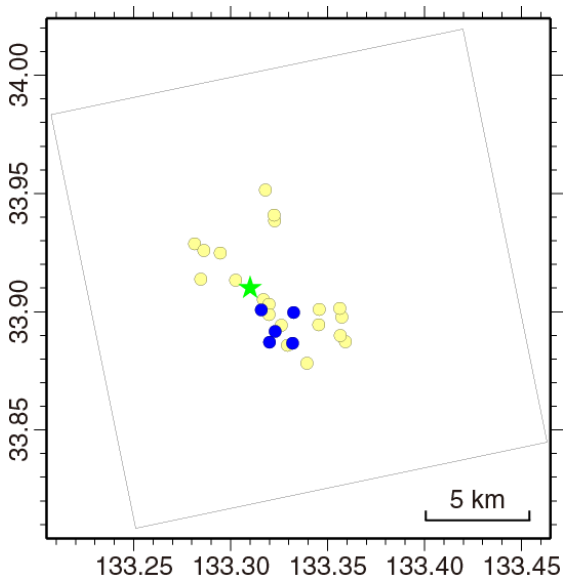

Figure 4.18: The centroids of 25 tremor episodes with durations over 100 seconds which occurred on 23 October, 2006 in the central Shikoku region. Blue circles show the centroids of tremor coincident with VLFs. Yellow circles show the centroids of tremor with no obvious VLFs. Green star denotes the centroid of VLF0.

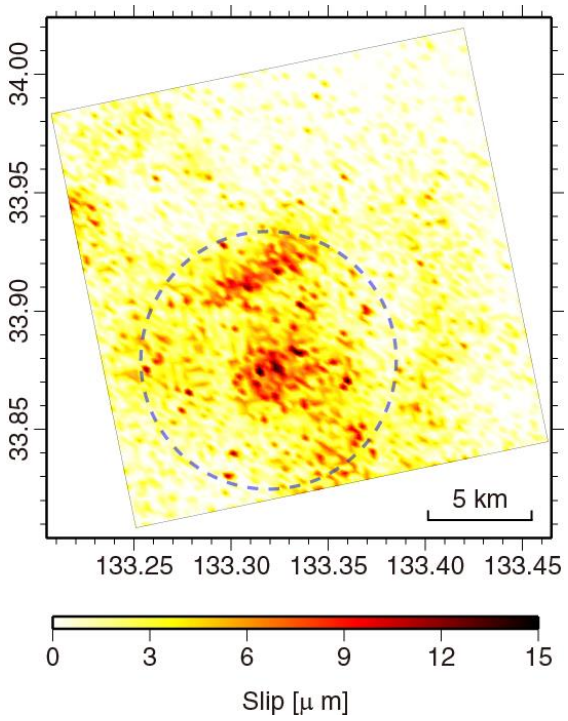

Figure 4.19: Total slip distribution of tremor coincident with all VLFs (VLF0-4) which is the summation of each distribution shown in Figure 4.13. Blue dotted circle denotes apparent source area of VLF.

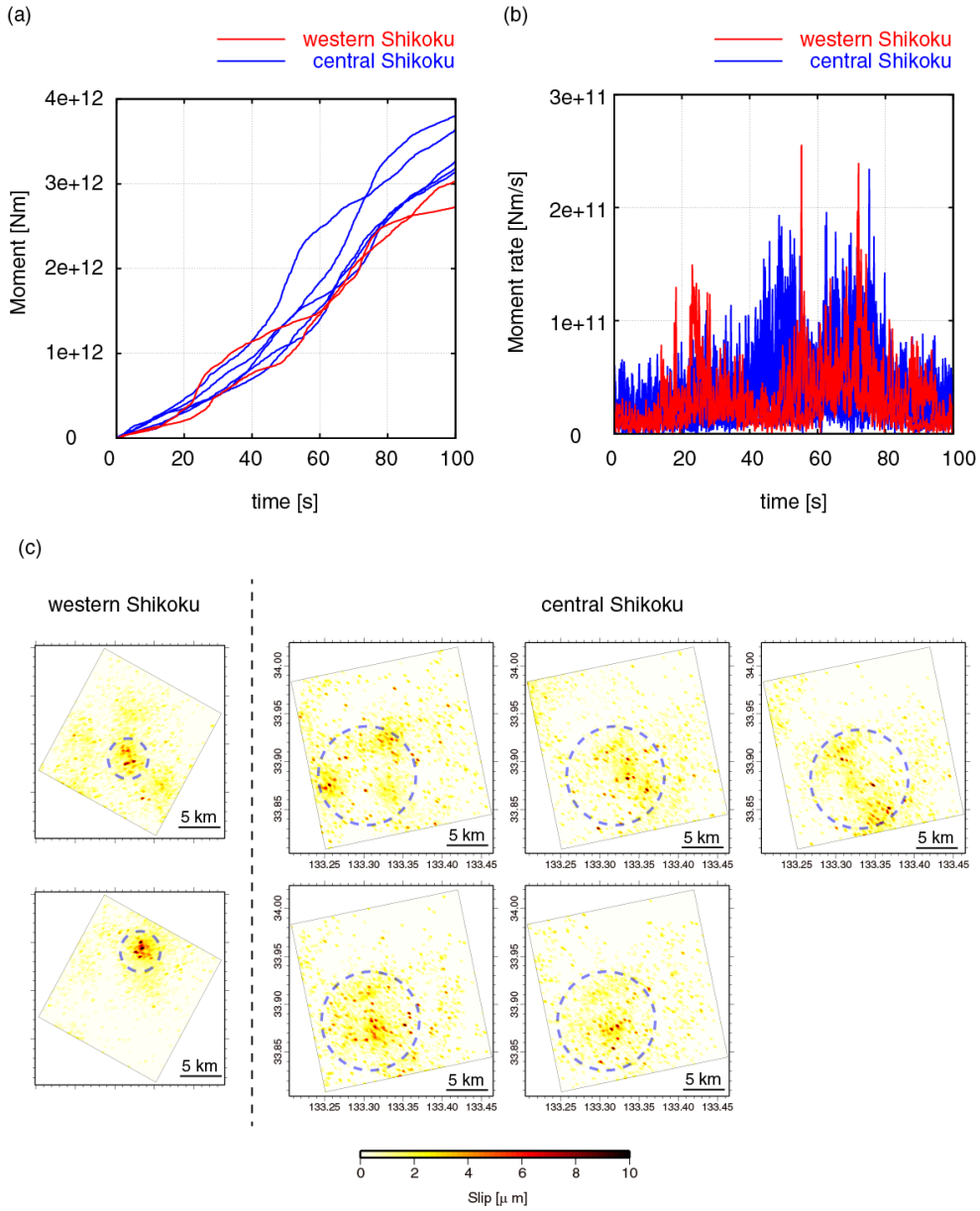

Figure 4.20: Comparison of slip behavior of tremor in the western and central Shikoku. Two tremors 100-200 s and 1100-1200 s from 23:30:00 on 16 March are focused in the western Shikoku and five tremors coincident with VLF0-VLF4 are focused in the central Shikoku. (a) Cumulative moment growth curves and (b) moment rate functions of focused tremors in the western Shikoku (red lines) and in the central Shikoku (blue lines). (c) The slip distributions of tremor in the western Shikoku and central Shikoku. Blue dotted circles indicate approximate source sizes.

Table 4.1: Parameter settings for inversion

	Western Shikoku	Central Shikoku
Fault Length	16 km	20 km
Fault Width	16 km	20 km
Node interval	250 m	250 m
Number of nodes	4,225	6,561
Duration/interval of basis time function	0.3/0.15 s	0.3/0.15 s
σ_x, σ_t	1 km, 100 s	1 km, 100 s
Number of LFEs used for synthetic templates from each node	607	160
Stations	9	6
Time window	1800 s	1800 s
Total number of time windows	576	48

Chapter 5 Conclusion

For detailed investigation of the slip behavior of deep tremor in western Japan, we have developed a new slip inversion method by a combination of precise locations of the plate interface, synthetic template waveforms, and iterative deconvolution method.

The location of the plate interface is obtained by the precise hypocenter distribution of LFEs. We relocate a large number of LFEs beneath the Shikoku region by using the NCC method. Relocated hypocenters of LFEs are more concentrated in depth than in the original catalog and show clear inclinations in every part of the region. We estimate the plate interface based on the distribution of LFEs. The distributions of LFEs are well fitted by a single plane in each subarea.

We introduce the synthetic template waveforms as the representatives of typical constituents of tremor sources on the plate interface by stacking the waveforms of known LFEs. The focal mechanism derived from synthetic template waveforms shows low-angle thrust faults, which supports the idea that LFEs are shear slips on the plate interface. Using synthetic template waveforms, we conduct a matched filter analysis to investigate tremor activities in the western Shikoku region. The synthetic template waveforms works well for detection and the detectability is over 100 times larger than that of the ordinary method adopted by JMA. The recurrence interval of tremor burst episode, 6 months, and the migration behavior of the tremor at the rate of ~20km/h are also consistent with the previous studies.

We finally invert continuous tremor waveforms by iterative deconvolution method with a Bayesian constraint using the synthetic template waveforms as substitutes of Green's functions. We apply the method to one tremor burst episode for 12 days in the western Shikoku and for 1 day in the central Shikoku region which contains the known VLF event. The observed waveforms are well explained by synthetic waveforms. The large seismic moment release in the first three days of tremor burst episode in the western Shikoku indicates the close association between the tremors and coincidental

SSEs. The major slips derived from the tremors occur on some patchy regions with relatively rapid moment releases with durations lower than 100 s. This may reflect the heterogeneities of material properties on the plate interface. The centroids of both tremor and VLF in the central Shikoku are almost identical, which suggests that the tremors are triggered within the source area of VLF. The source size of VLFs in the central Shikoku approximated by slip distribution of tremor, ~5 km in radius, is much larger than the size of patchy slip region of tremors in the western Shikoku. Such difference in source size might possibly control the occurrence of VLFs.

This thesis is the first attempt to investigate a detailed spatio-temporal evolution of deep tremor by slip inversion method. For general discussion in occurrence condition of VLFs and other slow earthquakes, we need more study in the future. Nevertheless, the present study shows the potential for investigating detailed source process of slip associated with slow earthquakes.

References

Akaike, H. (1973), Information theory and an extention of the maximum likelihood principle, *Proceedings of the second International Symposium on Information Theory*, edited by Petrov, B. N. and Caski, F., pp. 267-281, Akadimiai Kiado, Budapest.

Aguiar, A.C, T.I. Melbourne, and C.W. Scrivner (2009), Moment release rate of Cascadia tremor constrained by GPS, *J. Geophys. Res.*,**114**, B00A05, doi:10.1029/2008JB005909.

Akaike, H. (1980), Likelihood and the Bayes procedure, in *Bayesian Statistics*, edited by J. M. Bernardo *et al.*, pp. 143-166, Univ. Press, Valencia, Spain.

Aki, K., and R. Koyanagi (1981), Deep volcanic tremor and magma ascent mechanism under Kilauea, Hawaii, *J. Geophys. Res.*, **86**, 7095-7109, doi:10.1029/ JB086iB08p07095.

Ammon, C. J., G. E. Randall, and G. Zandt (1990), On the nonuniqueness of receiver function inversions, *J. Geophys. Res.*, **95**(B10), 15303-15318, doi:10.1029/JB095iB10p15303.

Ando, R., R. Nakata, and T. Hori (2010), A slip pulse model with fault heterogeneity for low-frequency earthquakes and tremor along plate interfaces, *Geophys. Res. Lett.*, **37**, L10310, doi:10.1029/2010GL043056.

Bartlow, N. M., S. Miyazaki, A. M. Bradley, and P. Segall (2011), Space-time correlation of slip and tremor during the 2009 Cascadia slow slip event, *Geophys. Res. Lett.*, **38**, L18309, doi:10.1029/2011GL048714.

Brown, J.R., G. C. Beroza, and D. R. Shelly (2008), An autocorrelation method to detect low frequency earthquakes within tremor, *Geophys. Res. Lett.*, **35**. L16305, doi:10.1029/2008GL034560.

Brown J. R., G. C. Beroza, S. Ide, K. Ohta, D. R. Shelly, S. Y. Schwartz, W. Rabbel, M. Thorwart, and H. Kao (2009), Deep low-frequency earthquakes in tremor localize to the plate interface in multiple subduction zones, *Geophys. Res. Lett.*, **36**. L19306, doi: 10.1029/2009GL040027.

Douglas, A., J. Beavan, L. Wallace, and J. Townend (2005), Slow slip on the northern Hikurangi subduction interface, New Zealand, *Geophys. Res. Lett.*, **32**, L16305, doi:10.1029/2005GL023607.

Dragert, H., K. Wang and G. Rogers (2004), Geodetic and seismic signatures of episodic tremor and slip in the northern Cascadia subduction zone, *Earth Planet. Space*, **56**, 1143-1150.

Ghosh A., J. E. Vidale, J. R. Sweet, K. C. Creager, A. G. Wech, and H. Houston, Tremor bands sweep Cascadia (2010), *Geophys. Res. Lett.*, **37**. L08301, doi: 10.1029/2009GL042301.

Gibbons S. J. and F. Ringdal (2006), The detection of low magnitude seismic events using array-based waveform correlation, *Geophys. J. Int.*, **165**, 149-166.

Gomberg J, the Cascadia 2007 and Beyond Working Group (2010), Slow-slip phenomena in Cascadia from 2007 and beyond: *a review. Geol. Soc. Am. Bull.,* 122:963-78.

Guilhem A. and R.M. Nadeau (2012), Episodic tremors and deep slow-slip events in Central California, *Earth Planet. Sci. Lett.*, **357** (2012), pp. 1-10, doi: 10.1016/j.epsl.2012.09.028.

Hartzell, S.H. and T.H. Heaton (1983), Inversion of strong ground motion and teleseismic waveform data for the fault rupture history of the 1979 Imperial Valley, California, earthquake, *Bull. Seismol. Soc. Am.*, **73**, 1553-1583.

Hirose, H. and K. Obara (2005), Repeating short- and long-term slow slip events with deep tremor activity around the Bungo channel region, southwest Japan, *Earth Planets Space*, **57**, 961-972.

Houston, H., B. G. Delbridge, A. G. Wech, and K. C. Creager (2011), Rapid tremor reversals in Cascadia generated by a weakened plate interface,*Nat. Geosci.*, **4**, 404-409, doi:10.1038/ngeo1157.

Ide, S., G. C. Beroza, and J. J. McGuire (2005), Imaging Earthquake Source Complexity, *Geophys. Monogr.*, **157**, 117-135.

Ide, S., D. R. Shelly, and G. C. Beroza (2007b), The mechanism of deep low frequency earthquakes: Further evidence that deep non-volcanic tremor is generated by shear slip on the plate interface, *Geophys. Res. Lett.*, **34**, L03308, doi:10.1029/2006GL028890.

Ide, S., G. C. Beroza, D. R. Shelly, and T. Uchide (2007a), A scaling law for slow earthquakes, *Nature*, **447**, 76-79.

Ide S., Imanishi K, Yoshida Y., Beroza G.C., and Shelly D.R. (2008), Bridging the gap between seismically and geodetically detected slow earthquakes, *Geophys. Res. Lett.*, **35**, L10305, doi:10.1029/2008GL034014.

Ide, S. (2010), Striations, duration, migration and tidal response in deep tremor, Nature, **466**, 356-359, doi:10.1038/nature09251.

Idehara, K., Yabe, S., and Ide, S. Regional and global variations in the temporal clustering of tectonic tremor activity, submitted.

Ito, Y., K. Obara, K. Shiomi, S. Sekine, H. Hirose (2007), Slow Earthquakes Coincident with Episodic Tremors and Slow Slip Events, *Science,* **315**, 503-506.

Ito, Y., K. Obara, T. Matsuzawa, and T. Maeda (2009), Very low frequency earthquakes as small asperity on plate boundary in transition zone from locked to aseismic slip, *J. Geophys. Res.*, **114**, B00A13, doi:10.1029/2008JB006036.

Kao, H., and S.-J. Shan (2004), The source-scanning algorithm: Mapping the distribution of seismic sources in time and space, *Geophys. J. Int.*, **157**, doi:10.1111/j.1365-246X.2004.02276.x.

Kao, H., S.-J. Shan, H. Dragert, G. Rogers, J. F. Cassidy, and K. Ramachandran (2005), A wide depth distribution of seismic tremors along the northern Cascadia margin, *Nature*, **436**, 841-844.

Kao, H., P. J. Thompson, G. Rogers, H. Dragert, and G. Spence (2007a), Automatic detection and characterization of seis-mic tremors in northern Cascadia, *Geophys. Res. Lett.*, **34**, L16313, doi:10.1029/2007GL030822.

Kao, H., S.-J. Shan, G. Rogers, and H. Dragert (2007b), Migration characteristics of seismic tremors in the northern Cascadia margin, *Geophys. Res. Lett.*, **34**, L03304, doi:10.1029/2006GL028430.

Katsumata, A., and N. Kamaya (2003), Low-frequency continuous tremor around the Moho discontinuity away from volcanoes in the southwest Japan, *Geophys. Res. Lett.*, **30**, doi:10.1029/2002GL015981.

Kikuchi, M. and H. Kanamori (1982), Inversion of complex body waves, *Bull. Seism. Soc. Am.*, **72**, 491-506.

Kikuchi, M. and H. Kanamori (1986), Inversion of complex body waves--II, *Phys. Earth Planet. Interiors*, **43**, 205-222.

Kikuchi, M. and H. Kanamori (1991), Inversion of complex body waves--III, *Bull. Seism. Soc. Am.*, **81**, 2335-2350.

La Rocca, M., K. C. Creager, D. Galluzzo, S. Malone, J. E. Vidale, J. R.Sweet, and A. G. Wech (2009), Cascadia tremor located near plate interface constrained by S minus P wave times, Science, **323**, 620-623,

doi:10.1126/science.1167112.

Lowry, A. R., K. M. Larson, V. Kostoglodov, and O. Sanchez (2005), The fault slip budget in Guerrero, southern Mexico, *Geophys. J. Int.*, **200**, 1-15.

Maeda, T. and K. Obara (2009), Spatiotemporal distribution of seismic energy radiation from low-frequency tremor in western Shikoku, Japan, *J. Geophys. Res.*, **114**, B00A09, doi: 10.1029/2008JB006043.

McCaffrey, R. (2009), Time-dependent inversion of three-component continuous GPS for steady and transient sources in northern Cascadia, *Geophys. Res. Lett.*, **36**, L07304, doi:10.1029/2008GL036784.

Menke, W. (1989), *Geophysical data analysis: Discrete inverse theory*, Academic Press.

Miyazawa, M. and J. Mori (2006), Evidence suggesting fluid flow beneath Japan due to periodic seismic triggering from the 2004 Sumatra-Andaman earthquake, *Geophys. Res. Lett.*, **33**, doi:10.1029/2005GL025087.

Nakata, R., R. Ando, T. Hori, and S. Ide (2011), Generation mechanism of slow earthquakes: Numerical analysis based on a dynamic model with brittle-ductile mixed fault heterogeneities, *J. Geophys. Res.*, **116**, B08308, doi:10.1029/2010JB008188.

Nakata, R., N. Suda, and H. Tsuruoka, (2008), Non-volcanic tremor resulting from the combined effect of Earth tides and slow slip events, *Nat. Geosci.*, **1**, 676-678, doi:10.1038/ngeo288.

Obara, K. (2002), Nonvolcanic deep tremor associated with subduction in southwest Japan, *Science*, **296**, 1679-1681.

Obara, K. (2010), Phenomenology of deep slow earthquake family in south-west Japan: Spatiotemporal characteristics and segmentation, *J. Geophys. Res.*, **115**, B00A25, doi:10.1029/2008JB006048.

Obara, K., H. Hirose, F. Yamamizu, and K. Kasahara (2004), Episodic slow slip events accompanied by non-volcanic tremors in southwest Japan subductionzone, *Geophys. Res. Lett.*, **31**, doi: 10.1029/2004GL020848.

Obara, K., S. Tanaka, T. Maeda, and T. Matsuzawa (2010), Depth-dependent activity of non-volcanic tremor in southwest Japan, *Geophys. Res. Lett.*, **37**, L13306, doi:10.1029/2010GL043679.

Obara, K. (2011), Characteristics and interactions between non-volcanic tremor and related slow earthquakes in the Nankai subduction zone, southwest Japan, *J. Geodyn.*, **52**, 229-248, doi:10.1016/j.jog.2011.04.002.

Ohta, Y., J. T. Freymueller, S. Hreinsdottir, and H. Suito (2006), A large slow slip event and the depth of the seismogenic zone in the south central Alaska subduction zone, *Earth Planet. Sci. Lett.*, **247**, 108-116, doi:10.1016/j.epsl.2006.05.013.

Ohta, K. and S. Ide (2008), A precise hypocenter determination method using network correlation coefficients and its application to deep low-frequency earthquakes, *Earth Planets Space*, **60**, 877-882.

Ohta, K., and S. Ide (2011), Precise hypocenter distribution of deep low-frequency earthquakes and its relationship to the local geometry of the subducting plate in the Nankai subduction zone, Japan, *J. Geophys. Res.*, **116**, B01308, doi:10.1029/2010JB007857.

Payero, J., V. Kostoglodov, N. Shapiro, T. Mikumo, A. Iglesias, X. Pérez-Campos, and R. Clayton (2008), Nonvolcanic tremor observed in the mexican subduction zone, *Geophys. Res. Lett.*, **35**, L07305, doi:10.1029/2007GL032877.

Peng, Z. and K. Chao (2008), Non-volcanic tremor beneath the Central Range in Taiwan triggered by the 2001 MW7.8 Kunlun earthquake, *Geophys. J. Int.*, **175**, 825-829, doi:10.1111/j.1365-246X.2008.03886.x.

Rogers, G., and H. Dragert (2003), Episodic tremor and slip on the Cascadia subduction zone: the chatter of silent slip, *Science*, **300**, 1942-1943.

Rubinstein, J. L., D. R. Shelly, W. L. Ellsworth (2010), Non-volcanic Tremor: A Window into the Roots of Fault Zones, *New Frontiers in Integrated Solid Earth Sciences*, International Year of Planet, 287-314, doi:10.1007/978-90-481-2737-5_8.

Rubinstein, J. L., J. E. Vidale, J. Gomberg, P. Bodin, K. C. Creager and S. D. Malone (2007), Non-volcanic tremor driven by large transient shear stresses, *Nature*, **448**, doi:10.1038/nature06017, 579-582.

Schwartz, S. Y., and J. M. Rokosky (2007), Slow slip events and seismic tremor at circum-Pacific subduction zones, *Rev. Geophys.*, **45**, RG3004, doi:10.1029/2006RG000208.

Sekine, S., H. Hirose, and K. Obara (2010), Short-term slow slip events correlated with non-volcanic tremor episodes in southwest Japan, *J. Geophys. Res.*, **115**, B00A27, doi:10.1029/2008JB006059.

Shelly, D. R., G. C. Beroza, and S. Ide (2007a), Non-volcanic tremor and low-frequency earthquake swarms, *Nature*, **446**, 305-307.

Shelly, D. R., Beroza, G. C. & Ide, S. (2007b), Complex evolution of transient

slip derived from precise tremor locations in western Shikoku, Japan, *Geochem. Geophys. Geosyst.*, **8**, Q10014, doi:10.1029/2007GC001640.

Shelly, D. R., G. C. Beroza, S. Ide, and S. Nakamula (2006), Low-frequency earthquakes in Shikoku, Japan and their relationship to episodic tremor and slip, *Nature*, **442**, 188-191.

Shiomi, K., M. Matsubara, Y. Ito, and K. Obara (2008), Simple relationship between seismic activity along Philippine Sea slab and geometry of the oceanic Moho beneath southwest Japan, *Geophys. J. Int.*, **173**, 1018-1029, doi:10.1111/j.1365-246X.2008.03786.x.

Suda, N.R., R. Nakata, and T. Kusumi (2009), An automatic monitoring system for nonvolcanic tremors in southwest Japan, *J. Geophys. Res.*, **114**, B00A10, doi:10.1029/2008JB006060.

Takeo, A., Idehara, K., Iritani, R., Tonegawa, T., Nagaoka, Y., Nishida, K., Kawakatsu, H., Tanaka, S., Miyakawa, K., Iidaka, T., Obayashi, M., Tsuruoka, H., Shiomi, K., Obara, K. (2010), Very broadband analysis of a swarm of very low frequency earthquakes and tremors beneath Kii Peninsula, SW Japan, *Geophys. Res. Lett.*, **37**, L06311, doi:10.1029/2010GL042586.

Takeo, M. (1987), An inversion method to analyze the rupture processes of earthquakes using near-field seismograms, *Bull. Seismol. Soc. Am.*, **77**, 490-513.

Ueno, H., S. Hatakeyama, T. Aketagawa, J. Funasaki, and N. Hamada (2002), Improvement of hypocenter determination procedures in the Japan Meteorological Agency, *Quater. J. Seismol.*, **65**, 123–134 (in Japanese with English abstract).

Wech, A.G. and K.C. Creager (2008), Automated detection and location of Cascadia tremor, *Geophys. Res. Lett.*, **35**, L20302, doi:10.1029/2008GL035458.

Wech, A. G., and K. C. Creager (2011), A continuum of stress, strength and slip in the Cascadia subduction zone, *Nat. Geosci.*, **4(9)**, 624-628, doi:10.1038/ngeo1215.

Wech, A. G., K. C. Creager, and T. I. Melbourne (2009), Seismic and geodetic constraints on Cascadia slow slip, *J. Geophys. Res.*, **114**, B10316, doi:10.1029/2008JB006090.

Yabuki, T., and M. Matsu'ura (1992), Geodetic data inversion using a Bayesian information criterion for spatial distribution of fault slip,

Geophys. J. Int., **109**, 363-375.

Zhang, H., and C. H. Thurber (2003), Double-difference tomography: The method and its application to the Hayward fault, California, *Bull. Seismol. Soc. Am.*, **93**, 1875-1889.

Acknowledgments.

I would like to express my deepest appreciation to my adviser Prof. Satoshi Ide for helpful advices and continuous encouragement. I would like to give my thanks to Prof. Kazushige Obara for constructive discussion and helpful suggestions. My defense committee members: Profs. Kazushige Obara, Minoru Takeo, Hitoshi Kawakatsu, Masao Nakatani, and Satoshi Ide kindly reviewed this thesis. Their constructive comments are helpful to improve this thesis. I also thank my Lab. members: Shintaro Tamura, Yoshiharu Kurihara, Naofumi Aso, Shimon Abe, Suguru Yabe, Masamichi Ara, Tomoaki Nishikawa, Drs. Takehito Suzuki and Koki Idehara for their assistances.
I would like to thank Dr. David R. Shelly for providing his result of relocated hypocenter data. I also express my thanks to Dr. Katsuhiko Shiomi for providing the digital data of his previous result. I am grateful to Prof. Gregory C. Beroza for enlightening comments.
A portion of this thesis has been published in *Journal of Geophysical Research* [Ohta and Ide, 2011]. I used the earthquake catalogs by Japan Meteorological Agency. Many figures are created using Generic Mapping Tool (GMT) by P. Wessel and W. H. F. Smith. This work was supported by Grant-in-Aid for Scientific Research, Ministry of Education, Sports, Science and Technology, Japan and JSPS Bilateral Joint Project. This work was also supported by JSPS KAKENHI, Grant-in-Aid for JSPS Fellows, 217481.